Surface stability

and small-scale testing of zirconia

A dissertation submitted in partial fulfillment of the requirements
for the degree of Doctor of Philosophy by

Erik Camposilvan

Department of Materials Science and Metallurgical Engineering
Doctorate program in Materials Science and Engineering
Universitat Politècnica de Catalunya - BarcelonaTech

Supervisor: Prof. Dr. Marc Anglada

UNIVERSITAT POLITÈCNICA DE CATALUNYA
BARCELONATECH
Departament de Ciència dels Materials
i Enginyeria Metal·lúrgica

April 2015

Cover photo: top view of a 3 μm diameter micropillar milled from the polished zirconia surface. A hair from the author is also visualized on the top-left of the image to better appreciate the sample size.

Outline

Tetragonal polycrystalline zirconia stabilized with 3 mol% of yttria (3Y-TZP) is a popular biocompatible ceramic, showing superior mechanical properties among single oxide ceramics. These properties are partly the consequence of phase transformation: thanks to the presence of the stabilizer, zirconia is composed mainly of a tetragonal metastable form, which can transform to the stable monoclinic phase through a martensitic transformation. The transformation, which involves a net volume increase, can be activated either mechanically by the application of high stresses, or chemically by the diffusion of water species, when the material is exposed to humid environment and moderate temperatures. In the first case, the local transformation at the crack tip under tension hinders its propagation, producing a phenomenon known as transformation toughening, which allows the design of "tough" and damage-tolerant ceramics. On the other hand, the spontaneous and progressive surface transformation in presence of humidity represents an aging phenomenon known as low-temperature degradation (LTD), hydrothermal degradation or aging. Although this phenomenon affects a surface layer of only few micrometers, it is accompanied by a substantial impairment of the surface integrity, which represents a serious issue for the use of 3Y-TZP in load-bearing biomedical applications. It was shown in orthopedics that zirconia femoral heads used in hip-joint arthroplasty may be vulnerable to LTD, leading in some cases to premature failures. Likewise, some recent publications devoted to dental zirconia have highlighted that zirconia is susceptible to LTD if exact processing conditions are not followed.

The first subject of this thesis is the study of reliable solutions to avoid hydrothermal degradation of 3Y-TZP. Two novel methods are proposed, which allow a strong enhancement of the aging resistance through limited changes in the standard processing steps for 3Y-TZP, while maintaining its good mechanical properties. These methods are based on co-doping the material from the surface with CeO_2 by two different approaches. One approach includes

infiltration of CeO_2 precursors in the pre-sintered porous material. During thermal decomposition and sintering, CeO_2 is trapped into the pores and diffused into 3Y-TZP, obtaining a functionally-graded material with decreasing CeO_2 content from the surface to the bulk. The co-doping profile has been optimized by studying the pre-sintering, infiltration and sintering parameters in order to avoid a drop in the mechanical properties that is generally found in CeO_2-doped zirconia. The second approach derives from the same idea but is applied to the dense material, where surface roughness has been created for adhesion or osseointegration purposes. After pressure infiltration of CeO_2 precursors into the surface defects and pores created during the roughening process, a few-micrometers thick co-doped layer is obtained with a diffusion treatment. This treatment helps sealing the surface defects and avoids hydrothermal degradation, without affecting the color or the mechanical properties. It is therefore directly applicable in the manufacturing of dental crowns, abutments and dentures.

The second subject of the thesis focuses on small-scale testing of zirconia near-surface regions. The existence of extrinsic size effects on the mechanical properties has been investigated, and the mechanical response of the degraded and non-degraded state has been compared in bending and compression. By testing micropillars and micro-cantilevers milled with focused ion beam (FIB) from the zirconia surface, it has been proved that mechanical properties are significantly different at the small-scale. Higher strength and strain at failure have been recorded with respect to the bulk state, as a result of the absence of processing defects and the occurrence of significant transformation-induced plasticity. No size effect has been found in terms of strength between small-scale samples of different sizes, whereas the "yield" stress for activating phase transformation is smaller for samples in the sub-micrometer range. Hydrothermal degradation produces a microcrack network which strongly impairs the mechanical properties of small-scale samples milled inside the degraded layer. In bending, a different response in terms of strength and stiffness has been measured depending on sample orientation, proving that that the induced damage is anisotropic. The degradation effects on the compressive behavior depend on pillar size, since the discrete contribution of a reduced number of weakened grain boundaries and microcracks yield to significant scatter in the response of sub-micrometric pillars.

Keywords: zirconia; 3Y-TZP; infiltration processing; dental materials; low-temperature degradation; micro-pillar; micro-cantilever; small-scale testing; size effect.

Preface

This dissertation is submitted for the degree of Doctor of Philosophy at the Universitat Politècnica de Catalunya - BarcelonaTech. The research described in this work was carried out by the author during the period from the 1st of September 2010 to the 31st of December 2015 under the supervision of Prof. M. Anglada in the Department of Materials Science and Metallurgical Engineering at the Universitat Politècnica de Catalunya. The work described in this dissertation is original, unless otherwise detailed references are provided.

This thesis is presented as a collection of published articles, which are listed in the next section. Chapter 1 is a review about the state of the art of biomedical grade zirconia and small-scale testing. The aim and scope of the thesis are presented in Chapter 2. The experimental details can be found in each article and supporting information (if present), whereas some additional experimental details about small-scale sample preparation and testing are included in Chapter 3. In Chapter 4, the seven articles included in this thesis are introduced in order of publication date. The full articles appear in the Chapters 5 to 9 and in Annexes A and B. **Article VII** and **Article III** are devoted to the infiltration of CeO_2 precursors in the pre-sintered porous material. The methodology of infiltration has been developed and the processing parameters have been studied and optimized through a multi-scale characterization of the obtained materials in terms of resistance to LTD, microstructure evolution and mechanical properties under various processing conditions. The method of pressure infiltration, designed for fully dense zirconia where surface roughness is needed, is studied in **Article IV** and applied to sandblasted and acid-etched materials. **Article I** is a study of the effect of hydrothermal exposure to standard 3Y-TZP with different grain sizes and Cerium infiltrated 3Y-TZP in terms of indentation crack profiles. This paper details a novel technique for revealing crack profiles, which has been employed in **Article III** to compare the resistance to crack formation in materials doped under different conditions. **Article VI** represents a detailed study of the compressive behavior of zirconia at the small-

scale. Monotonic and cyclic compression tests are performed on micropillars and the behavior is compared with macroscopic samples. Advanced characterization techniques are applied to give an interpretation to the observed plastic effects and size-dependent phenomena. In **Article II**, the in situ micro-cantilever bending technique is applied to 3Y-TZP to measure its flexural response at the small-scale. The mechanical behavior is compared between micro-cantilevers milled from non-aged surfaces and from inside the degraded layer. In the latter, by testing samples with different orientations with respect to the degraded surface, the anisotropy of the damage induced by hydrothermal degradation is assessed. A similar approach is followed in **Article V**, where the micropillar compression technique is applied before and after degradation to study the compressive behavior of aged and non-aged pillars. Moreover, interesting insights on the effect of the damage induced by LTD are observed by testing small-scale samples of different sizes and by performing loading/unloading tests at increasing peak stress.

The main results and conclusions of the research work are reviewed in Chapter 10, together with its scientific impact and possible future implications.

List of publications

This dissertation is based on the articles contained in the following list, in order of publication date. IF = impact factor; Q = quartile.

Article I. Marro, F. G., **Camposilvan, E.** & Anglada, M. *Revealing crack profiles in polycrystalline tetragonal zirconia by ageing.* Journal of the European Ceramic Society **32,** 1541–1549 (2012). doi: 10.1016/j.jeurceramsoc.2012.01.013. IF 2.307, Q1 (2/25) in the cathegory: "Materials science, ceramics".

Article II. **Camposilvan, E.**, Torrents, O. & Anglada, M. *Small-scale mechanical behavior of zirconia.* Acta Materialia **80,** 239–249 (2014). doi: 10.1016/j.actamat.2014.07.053. IF 3.940, Q1 (35/251) in the cathegory "Materials science, multidisciplinary", and Q1 (1/75) in "Metallurgy & metallurgical engineering".

Article III. **Camposilvan, E.**, Garcia Marro, F., Mestra, A. & Anglada, M. *Enhanced reliability of yttria-stabilized zirconia for dental applications.* Acta Biomaterialia **17**, 36-46 (2015). doi: 10.1016/j.actbio.2015.01.023. IF 5.684, Q1 (3/76) in the cathegory: "Engineering, biomedical", and Q1 (3/32) in "Materials science, biomaterials".

Article IV. **Camposilvan, E.**, Flamant, Q. & Anglada, M. *Surface roughened zirconia: Towards Hydrothermal stability.* Journal of the Mechanical Behavior of Biomedical Materials **47**, 95-106 (2015). doi: http://dx.doi.org/10.1016/j.jmbbm.2015.03.017. IF 3.048, Q1 (15/76) in the cathegory: "Engineering, biomedical" and Q2 (10/32) in "Materials science, biomaterials".

Article V. **Camposilvan, E.** & Anglada, M. *Micropillar compression inside zirconia degraded layer.* Journal of the European Ceramic Society (2015). doi:

10.1016/j.jeurceramsoc.2015.04.017. IF 2.307, Q1 (2/25) in the cathegory: "Materials science, ceramics".

Moreover, the following articles are included as annexes for completeness.

Article VI (Annex A). **Camposilvan, E.** & Anglada, M. *Role of size and plasticity in zirconia micropillars compression.* Article submitted to Acta Materialia, under review (2015, submission ref. A-15-657).

Article VII (Annx B). **Camposilvan, E.**, Garcia Marro, F., Mestra, Á. & Anglada, M. *Development of a novel zirconia dental post resistant to hydrothermal degradation*. IOP Conference Series: Materials Science and Engineering 31, (2012). doi:10.1088/1757-899X/31/1/012016

Contents

List of Figures and Tables

Figures

Tables

Glossary of terms

3Y-TZP: TZP stabilized with 3% mol content of Y_2O_3

AFM: Atomic Force Microscopy

AS: As-sintered

ATZ: Alumina-Toughened Zirconia

B3B: Ball-on-three-balls strength test

Ce-TZP: TZP stabilized with CeO_2

CIP: Cold isostatic pressing

CSM: Continuous Stiffness Measurement

EDS: Energy-Dispersive X-ray Spectroscopy

EPMA: Electron Probe Micro Analysis

FGM: Functionally-Graded Material

FIB: Focused Ion Beam

MAJ: Mehl-Avrami-Johnson

MIP: Mercury Intrusion Porosimetry

PSZ: Partially Stabilized Zirconia

SEM: Scanning Electron Microscopy

TBCs: Thermal Barrier Coatings

TEM: Transmission Electron Microscopy

THA: Total Hip Arthroplasty

TZP: Tetragonal Polycrystalline Zirconia

XRD: X-ray diffraction

Y-Ce-TZP: TZP stabilized with Y_2O_3 and CeO_2

ZTA: Zirconia-Toughened Alumina

Chapter 1

Introduction

1.1. Overview: zirconia-based ceramics

Zircon gems were known since ancient times, and zirconia (Zirconium oxide) was used during centuries as a pigment for ceramics, but the material itself could not be processed due to catastrophic phase transformation during cooling of sintered parts. Nevertheless, since about 90 years ago, sane zirconia parts could be obtained at room temperature thanks to the addition of stabilizers starting [1]. The seminal discovery of transformation toughening in 1975 [2], paved the way to their wider use because of their excellent strength, fracture toughness, hardness and chemical stability.

These materials are used in high refractory and thermal shock resistant parts like valves and liners for engines and in foundry, extrusion dyes and thermal barrier coatings (TBCs), wear resistant component like blades, moulds and bearings and as high-temperature ionic conductors, *e.g.* solid electrolytes in fuel cells and in gas sensors [3].

The first paper concerning the use of zirconia to manufacture ball heads for Total Hip Arthroplasty (THA), was introduced by Christel *et al.* in 1988 [4]. In the 90's, biomedical grade 3% molar yttria-tetragonal polycrystalline zirconia (3Y-TZP) became an alternative to alumina as structural bioinert ceramic in orthopedics because it has substantially higher fracture toughness and strength. In fact, 3Y-TZP exhibits some of the best mechanical properties among single-phase oxide ceramics: flexural strength above 1000 MPa, fracture toughness around 5 MPa·√m and hardness above 12 GPa. The use of 3Y-TZP in orthopedics paved the way to new implant designs that were not possible with alumina, which is more

brittle. Examples of medical applications are smaller 3Y-TZP femoral heads, 3Y-TZP knees and more recently a large range of dental devices (crowns, bridges, abutments and dental implants), where the translucency and easy color modification for matching teeth shade offered by TZP is of great interest [3], [5].

Fracture toughness in 3Y-TZP is related to the transformation toughening mechanism, that is, the local tetragonal to monoclinic (*t–m*) martensitic phase transformation activated by stress and accompanied by a volume increase that occurs in front of the crack tip. Since the surrounding elastic material does not transform, this induces a net compressive residual stress which develops on the crack flanks and hinder crack growth [2].

In spite of these excellent properties, 3Y-TZP has a strong drawback: poor resistance to hydrothermal degradation also referred to as *Low Temperature Degradation* or *aging* (LTD) [6]. This phenomenon consists in the spontaneous and progressive *t–m* phase transformation which happens at the surface when exposed to humid environment and moderate temperature.

The kinetics of *LTD* depends on the alloying element, its concentration and other microstructural parameters, but in general this process affects only near-surface regions [7], with the transformed surface layer growing progressively in the depth direction [8]. The phase transformation is accompanied by the formation of microcracks and surface roughening, which reduce the hardness [9] and induce grain pull-out [3]. Although the kinetics of transformation is maximal at temperatures around 250ºC, there is now evidence that LTD is also possible at lower temperatures, even at human body temperature. This was considered as a minor issue by femoral heads manufacturers until an unusual high rate of failures for some batches of 3Y-TZP femoral heads was reported in 2001 during a short period of time [10]. During the posterior investigation, it was clearly established that these failures had their origin in a change in the processing steps of the balls that decreased their resistance to LTD.

These failures had a strong negative impact on the implementation of zirconia in hip arthroplasty. Additionally, there are now many reports on explanted femoral heads which show that even in prosthesis processed under normal conditions, *t–m* transformation occurs and the surface is degraded in contact with human body fluids. As a consequence, 3Y-TZP is currently not anymore used in the manufacturing of femoral heads prosthesis in Europe and United States [11] and new nanocomposites, mainly based on the alumina-zirconia system, have been developed instead.

Nevertheless, monolithic zirconia femoral heads are still being manufactured in some countries (*e.g. in Japan*) [12] and there is major interest in applying zirconia in different other biomedical applications, especially in orthopedics and for dental restorations and implants since new shaping techniques have been recently developed [13]. A considerable effort is directed nowadays to the improvement of zirconia surface long-term reliability, which is still a matter of concern in all these applications.

1.2. Introduction to tetragonal zirconia

Zirconia is a Zirconium oxide (ZrO_2). It was first identified in 1789 by the German chemist Martin Heinrich Klaproth as the dioxide of Zirconium, a metal whose name comes from the Arabic *Zargon*, which means *golden in color*. The words *zar* (gold) and *gun* (color) were actually Persian in origin [3].

The crystallographic structure of zirconia exhibits three allotropes: monoclinic phase from room temperature up to 1170 ºC, tetragonal phase from 1170 ºC up to 2370 ºC and cubic phase for temperatures above 2370 ºC. The tetragonal-monoclinic (*t–m)* phase transformation is martensitic and is accompanied by a volume expansion of approximately 4 % (see Appendix 1 for further details on the *t-m* transformation). This phase transformation is reversible and, in pure zirconia, it occurs on cooling at approx. 950 ºC. The expansion creates large internal stresses, which compromise the integrity of the material and induce generalized cracking.

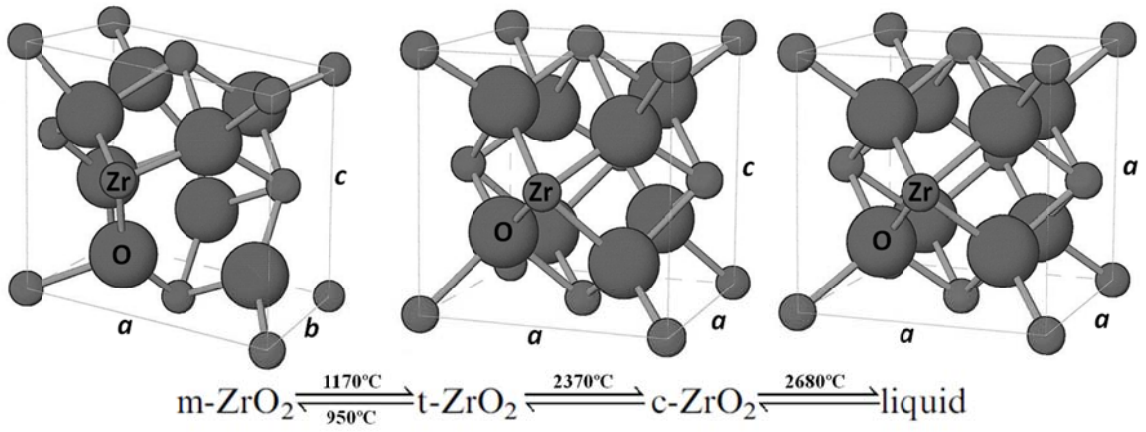

Figure 1.1. Allotropic structures of pure zirconia and transformation temperatures. From left to the right: monoclinic ($P2_1/c$), tetragonal ($P4_2/nmc$), and cubic ($Fm\text{-}3m$) structures.

In order to maintain the integrity of sintered zirconia, the tetragonal or cubic phases can be fully or partially stabilized at room temperature by alloying zirconia with another

oxide. The most widely used stabilizers are Calcium oxide (CaO), Magnesium oxide (MgO), Yttrium oxide (Y_2O_3) and Cerium oxide (CeO_2). Figure 1.2 shows the phase diagram for the binary system ZrO_2-Y_2O_3.

According to the final microstructure achieved, zirconia ceramics can be conveniently classified into three major types [7]:

- *Fully stabilized zirconia* (FSZ): the crystallographic phase is mostly cubic. These ceramics are frequently used in oxygen sensors and fuel cell electrolytes.

- *Partially stabilized zirconia* (PSZ): consists of nano-sized tetragonal precipitates in a cubic matrix. Such ceramics are generally obtained with the addition of CaO or MgO.

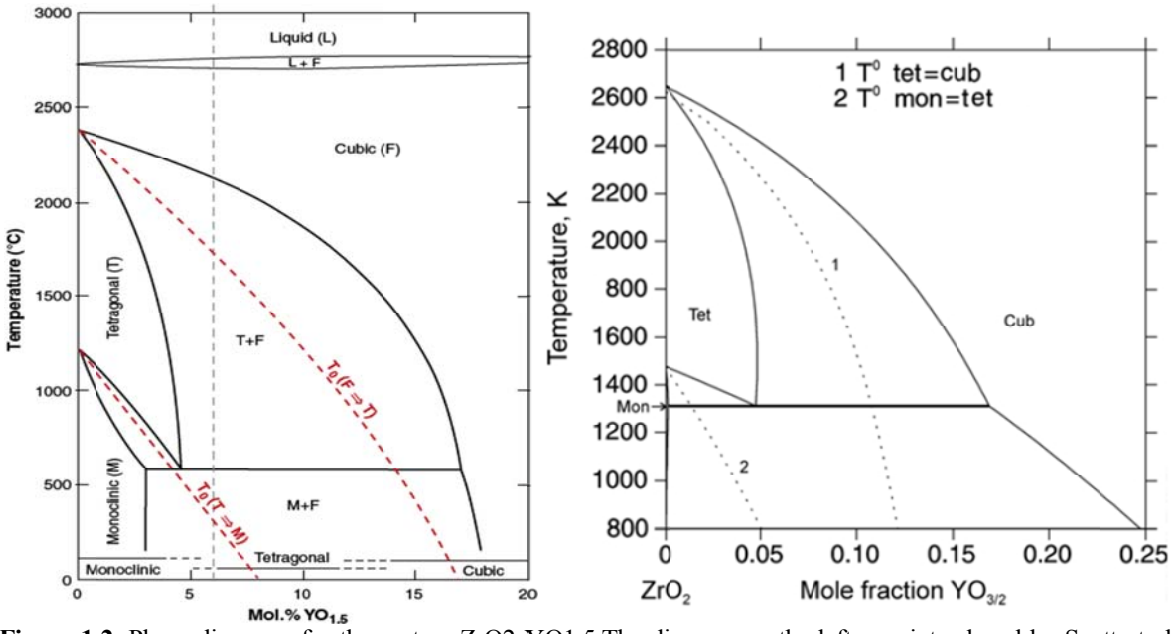

Figure 1.2. Phase diagrams for the system ZrO2-YO1.5.The diagram on the left was introduced by Scott et al [14], where the metastable phases retained at room temperature are indicated with horizontal lines at the bottom of the picture. The red dashed lines indicate the T_0 temperatures, which separate the non-equilibrium transition regions between the monoclinic (M) and tetragonal (T) phases and between tetragonal and cubic phases (F = fluorite), while the vertical dashed line represent the composition for 3Y-TZP. The updated diagram on the right was calculated by Fabrichnaya et al [15].

- *Tetragonal Zirconia Polycrystals* (TZP): With alloy stabilization, the tetragonal phase can be retained in a metastable state down to room temperature even though the equilibrium phase is monoclinic. This type of ceramic exhibits exceptional fracture toughness when transformation to the monoclinic phase is locally triggered by the high tensile stresses in front of a crack tip during its propagation.

From now on in this manuscript, only TZP materials will be of interest. The Y_2O_3 content has a strong influence on the tetragonal phase stability and therefore on fracture toughness of Y-TZP ceramics. As shown in Figure 1.7, the fracture toughness of tetragonal Y-TZP, which can reach values as high as 5-6 MPa·√m, decreases with increasing Y_2O_3 content. Nevertheless, the fracture toughness of the cubic and monoclinic phases is as low as about 2 MPa·√m. However, high toughness does not mean necessarily high strength. It has been shown that by the destabilization of the tetragonal phase, the strength of TZP can be increased, but there is limit over which the fracture toughness starts to drop. This marks the transition from the strength controlled by the flaw size to transformation-limited strength. Hannink *et al.* [16] proposed that, for materials with KIc less than approx. 8 MPa√m the strength is limited by flaw size, whereas, above this value, it is limited by stress-activated phase transformation, which occurs at a stress lower than the fracture stress. This behavior is also evidenced in the Figure 1.3, where the strength-toughness relation for various zirconia ceramics is showed. In any case, when the stabilizer content is optimized for transformation toughening, LTD resistance is also affected, as it will be discussed in section 1.6.

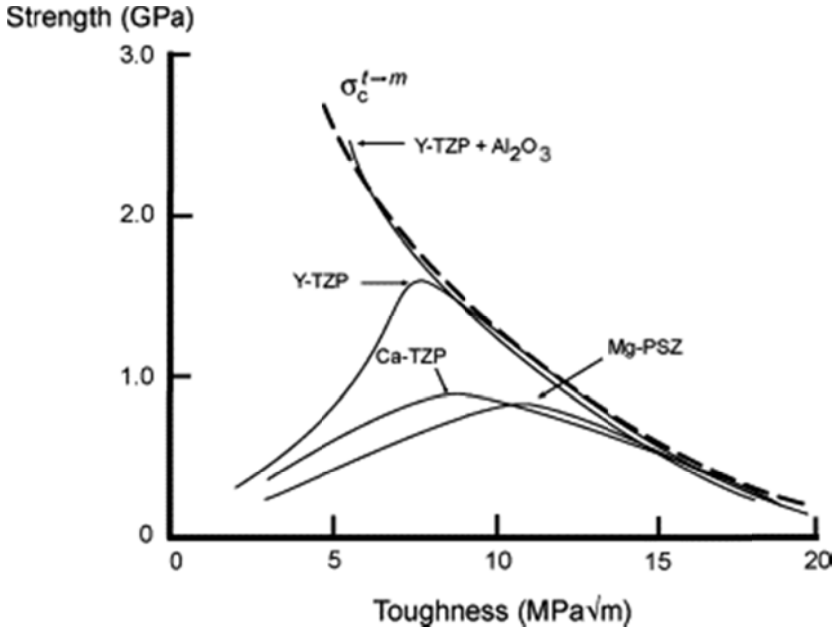

Figure 1.3. Strength-toughness relation for some PZT and TZP ceramics. Adapted from ref. [17].

1.3. The t–m transformation

The *t–m* phase transformation in zirconia is martensitic. This means that is athermal, diffusionless and involves the simultaneous, cooperative movement of atoms over distances less than an atomic diameter. Therefore, it produces a macroscopic change of shape of transformed regions [18].

To explain the behavior of zirconia ceramics, it is essential to understand the role of the stabilizers. For doing so, it is necessary to know the thermodynamics of the *t–m* phase transformation. Considering the simple ideal case of a spherical tetragonal particle in a matrix, the change of total free energy (ΔG_{t-m}) due to its transformation is given by:

$$\Delta G_{t-m} = \Delta G_C + \Delta U_{SE} + \Delta U_S \tag{1.1}$$

where ΔG_c (< 0 when $T < M_s$) is the chemical free energy change (dependent on temperature and composition), ΔU_{SE} (> 0) is the strain energy change associated with the transformed particles (dependent on the surrounding matrix and its stiffness, the size and shape of the particle, and the presence of stresses), and ΔU_S (> 0) is the change in energy associated with the surface of the particle (creation of new interfaces and micro-cracking). Through a decrease in $|\Delta G_c|$ and an increase in ΔU_{SE}, the addition of alloying oxides such as Y_2O_3 in Y-TZP decreases the driving force of the *t–m* transformation and hence its temperature, with the result of the metastable phase diagram of Figure 1.2, allowing the retention of metastable tetragonal particles at room temperature. At the same time, a stiffer matrix can stabilize the tetragonal phase reducing ΔU_{SE}. Moreover, the driving force for the transformation is not the same for the bulk and the surface of the material, because both ΔU_S and ΔU_{SE} are different, especially when it is considered the possibility of accommodating the volume change with a surface uplift [7].

Some authors [19], [20] have argued that stabilization of the tetragonal phase at room temperature is a direct consequence of the presence of oxygen vacancies introduced by the aliovalent alloying elements rather than by the aliovalent dopant itself. It has been shown computationally that the tetragonal phase can be produced with lower energy than the monoclinic phase by introducing oxygen vacancies and without any aliovalent ions into the unit cell [21]. Then, all the phase diagrams for different stabilizers would roughly collapse onto one when plotted as a function of concentration of oxygen vacancies, so it can be understood how the concentration of oxygen vacancies is a crucial factor. However, this is not the complete explanation of the behavior of TZP ceramics as shown by Li *et al.* [20], [22], [23], who studied the effect of the various aliovalent dopants and determined the local atomic structures. The key concept in zirconia stabilization is that Oxygen atoms tend to be overcrowded around the small Zr atom, reducing the stability of the structure with the 8-fold coordination. By relieving the overcrowding with aliovalent doping and vacancy generation,

the tetragonal and cubic structures are stabilized. With trivalent dopants, the cations adopt the zirconia structure and oxygen vacancies are generated for charge compensation:

$$Y_2O_3(ZrO_2) \rightarrow 2Y'_{Zr} + 3O_O^x + V_O^{\bullet\bullet} \quad (1.2)$$

It was concluded that the vacancies are associated with the Zr cations in the case of oversized trivalent dopants (Y^{3+}, Gd^{3+}), and with two dopant cations sharing one vacancy in the case of undersized dopants (Fe^{3+}, Ga^{3+}). While in both cases, Oxygen overcrowding is partially relieved, oversized dopants are more efficient due to the position of the vacancy (near Zr) and the additional dilatation of the cation network.

With tetravalent dopants like Ce^{4+} and Ge^{4+} forming solid solutions, two sets of tetrahedra form with Zr. Ce forms a random substitution with a decrease in tetragonality[1], where the CeO_8 polyhedra is bigger than for pure ZrO_2 but smaller than in pure CeO_2. Therefore, Ce dilates the lattice because of his oversized dimension, decreasing oxygen overcrowding and so improving tetragonal stability. The behavior of Ge is the opposite since it forms an ordered substitution and increases the tetragonality. The stabilization of tetragonal phase has been associated in the latter case to the cation ordering and the full development of bifurcated tetrahedral bondings in the layer-like structure [22].

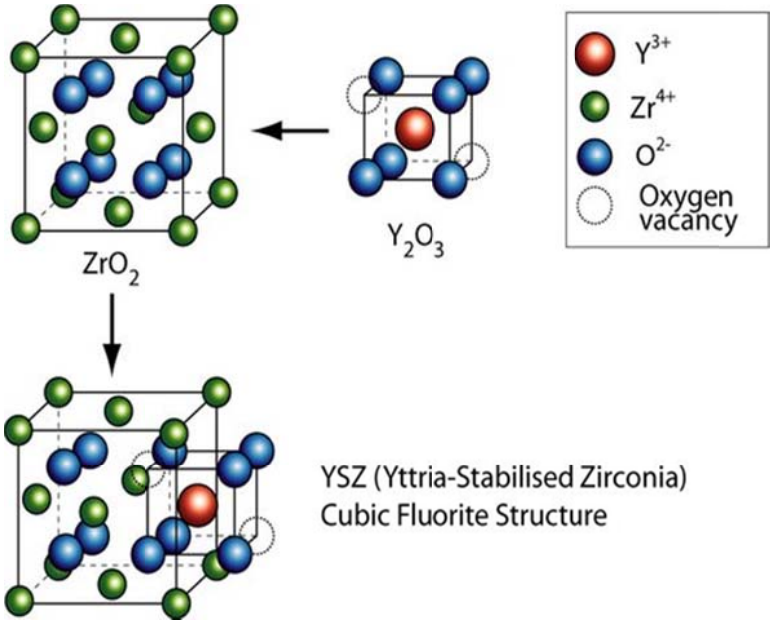

Figure 1.4. Formation of oxygen vacancies into the ZrO2 lattice when its doped with Y2O3 [24].

[1] Tetragonality: feature of tetragonal Zirconia that consists of a different strength and length of Zr-O_1 and Zr-O_2 bonds, where O_1 and O_2 are Oxygens of different layers in the lattice. It corresponds so with the anisotropy of the tetragonal layer structure and is an indicator of the instability of the tetragonal phase.

1.4. Processing of zirconia-based ceramics

Diverse techniques can be employed to process dense zirconia based ceramics with the desired shape, integrity and dimensional tolerances. These techniques can be summarized in two main categories: wet and dry processing.

1.4.1. Slip casting

Among wet processing techniques, slip casting is the one traditionally used for the fabrication of pottery, which need the preparation of an adequate suspension (slip) of the powder. This can be formed by particles of different constituents or already pre-alloyed. The suspension is poured into a mould with the desired shape, in which the liquid is partially absorbed giving some mechanical strength to the "green" piece, which is then allowed to dry. After drying, the piece can be fired and, depending on the firing technique and temperature, the desired density can be achieved. Despite of the versatility of this process and the reduced waste of material, up to now it is only occasionally employed in the manufacturing of biomedical implants, even though the interest toward slip casting has been recently rising due to the possibility to create engineered surfaces for bone adhesion and regeneration.

1.4.2. Dry processing

The dry processing route involves the employment of powders with tailored characteristics of particle size, composition, flowability and strength after pressing. Even though there is not only one way to process powders and current research is addressed to evaluate possible modifications and improvements to the method, the following describes a general route followed by most of the companies. Powders are constituted of spray-dried spherical agglomerates, generally around 60 μm in size, of smaller particles usually of some tens of nanometers, with crystallites of 20-30 nm (see Figure 1.5). These agglomerates, containing also a binder designed for giving the green strength, are usually pressed isostatically in a deformable mould to obtain the green piece, which can be manipulated. The green piece is then pre-sintered in air, obtaining a porous machinable preform with a reasonable mechanical strength.

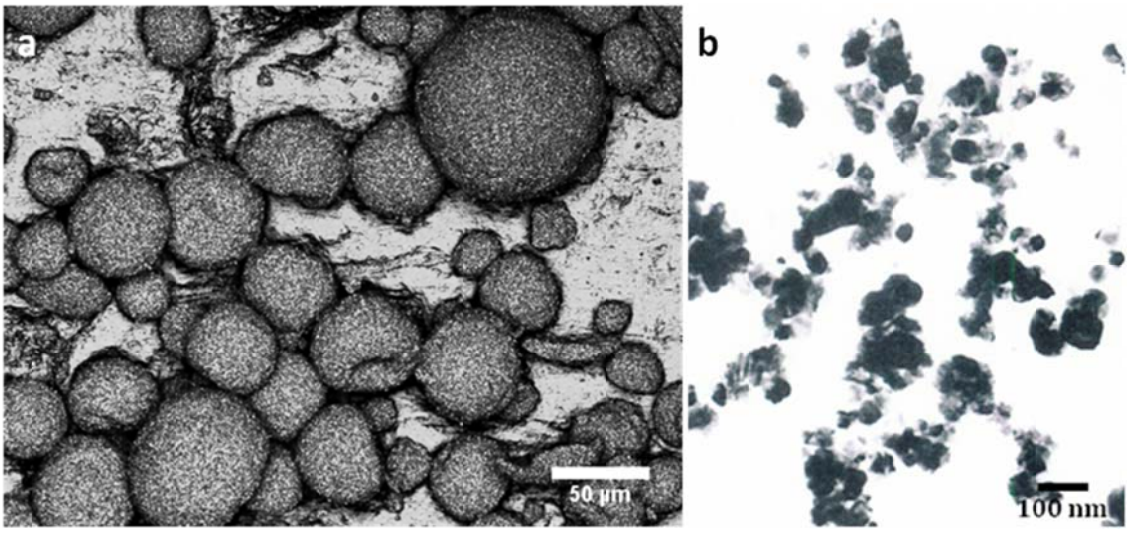

Figure 1.5. In picture *a* (Laser Scanning Confocal Microscopy) the spray-dried granules are showed, in picture *b* the particles forming the granules are visualized with TEM.

During pre-sintering, which is commonly performed around 1100 ºC, the binder is eliminated and burn out products must be allowed to escape by choosing a correct heating rate and dwell time [5]. The pre-sintered blank can be soft machined via Computer Aided Design/Computer Aided Manufacturing (CAD/CAM), taking into account the shrinkage of the piece during full sintering, to the desired shape. In the CAD/CAM system, which is typically applied to total joint arthroplasty prosthesis, dental posts and abutments, *i.e.* when the shape is standard, the part is designed with a computer. On the other hand, for the production of dental crown and bridges a replica of the part is scanned, either with contact or non-contact methods, and the CAM centre machines the shrinkage-compensated part into the blank [25]. After soft machining the parts are sintered at temperatures that can range between 1300 ºC and 1550 ºC depending on the time and atmosphere used. Some manufacturers perform the sintering in two or more steps, including a Hot Isostatic Pressing (HIP) treatment at the end in order to minimize the residual porosity. Once fired, the piece in only seldom used as it is; often strict tolerances are expressed and hard machining and polishing has to be performed. When the piece is designed for joint replacement, careful polishing is performed to obtain very smooth surfaces and reduce the presence of residual stresses. After cleaning, sterilization and packaging the part is ready for being implanted.

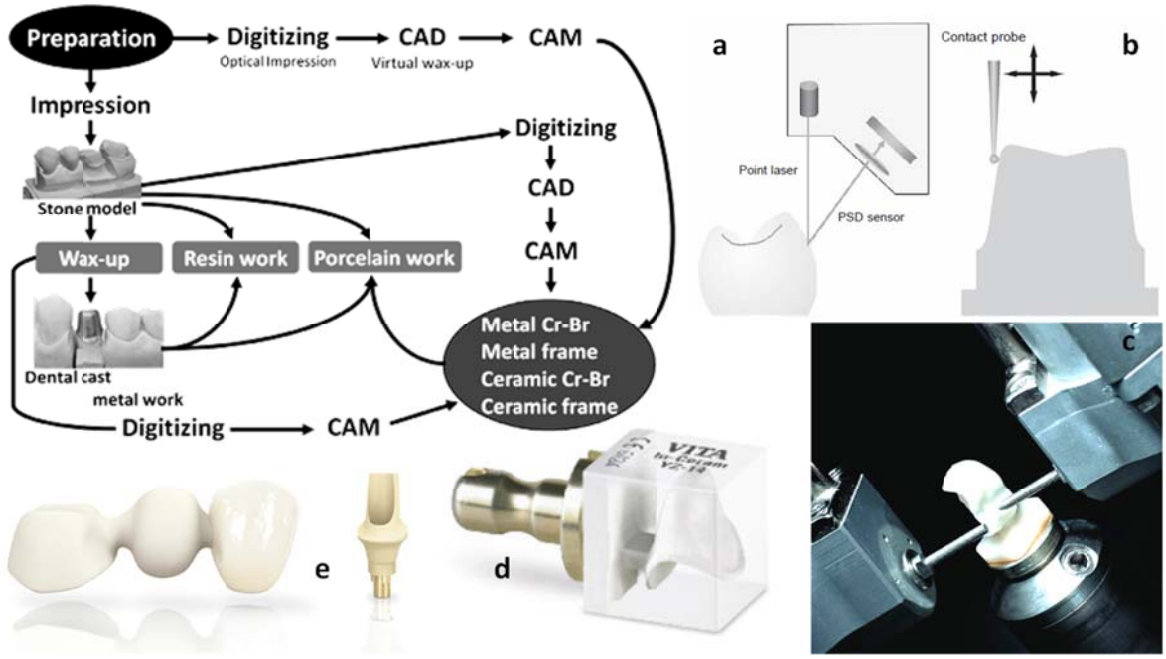

Figure 1.6. Top-left: scheme representing current dental CAD/CAM systems for Crown and bridge restorations. *a* and *b*: laser and contact scanning, respectively, of the replica tooth. *c*: soft machining (CAM) of the pre-sintered blank. *d*: pre-sintered blank (VITA corp.) showing the shape of a milled crown. *e*: final shape of a sintered abutment (right) and bridge with partial veneering (left). Reproduced from Miyazaki *et al.*[25].

1.5. A material of choice for biomedical implants

Why to use zirconia in biomedical implants? It was already stated that mechanical properties are very good among ceramics, both in terms of strength and wear resistance. A rapid look at Table 1.1 can give an idea of the main mechanical properties for various ceramics used as biomaterials. Besides, being an oxide ceramic, its chemical state is very stable if compared with metals, where ion release due to corrosion is becoming more and more matter of concern.

Table 1.1. Mechanical properties of different ceramics for biomedical applications. From ref. [26]

Material	Toughness (K_{IC}, MPa $m^{1/2}$)	Threshold (K_{I0}, MPa $m^{1/2}$)	Strength (MPa)	Vickers hardness
Alumina	4.2	2.4	400–600	1800–2000
Zirconia	5.4	3.5	1000	1200–1300
A10Z0Y	5.8	4	700–900	1800
Hydroxyapatite	0.9	0.6	50–60	500
Tricalcium phosphate	1.3	0.8	50–60	900
Mg-PSZ	8	6	600	1000
12Ce-TZP	7.8	5.1	700	1000–1100
Micro-nano-alumina–zirconia	6	5	600	1800
Nano-nano-Ce-TZP–alumina	8.4	4.6	900	1300
Silicon nitride	10*	?	1000*	2500

Zirconia has been proved to be biocompatible in vitro and in vivo and it is osseoconductive. The interaction with soft tissues (mainly fibroblastic) can be modified with physical and chemical treatments. Some studies have shown that zirconia and its derivatives (ZrN) are able to reduce plaque on implant and surrounding tissues, indicating that they

should have an important role in soft tissue healing and implant success at bone level. Resorption of peri-implant bone is probably avoided as well. Finally, the capacity of zirconia to be colored to match natural teeth tint represents a beneficial property compared to titanium in aesthetical applications [27].

1.6. Low-temperature degradation (LTD)

Low temperature degradation (LTD) is the phenomenon by which the tetragonal phase is converted into monoclinic by the diffusion of water-derived species (see Appendix 2 for details on LTD mechanism and kinetics). This degradation is a complex process that involves various steps and leads to surface roughening, micro and macro-cracking, grain pull-out and may also induce loss of strength after very long exposure times or altered microstructures. Unfortunately, the Y-TZP compositions that show the best performances for the fracture toughness are at the same time those that are the most susceptible to LTD [7] (see Figure 1.7). This happens because the transformability of the tetragonal phase, which promotes transformation toughening, is in general also responsible for the driving force for LTD.

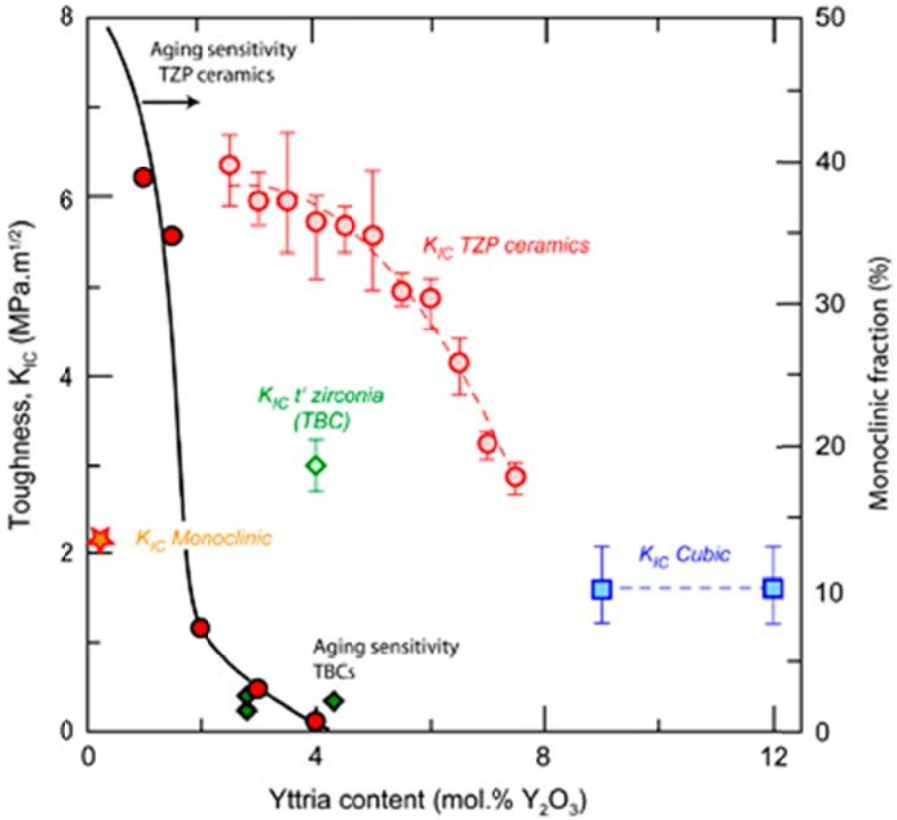

Figure 1.7. Fracture toughness and aging sensitivity of Y-TZP as a function of yttria content. Toughness data for cubic and monoclinic zirconia is shown together with the toughness of a zirconia thermal barrier coating (TBC). Aging sensitivity (solid line) is indicated by the monoclinic fraction after 3 hours at 134ºC in water vapor [7].

A complete and accurate description of the phenomenon of LTD is still missing, however many reports have qualitatively argued on possible explanations. The most accepted one is that transformation is likely to be due to the increase of internal stresses and reduction of vacancies associated with the penetration of water species, which have been often recognized as hydroxyl ions [28] or water molecules [29]. More recently, a variation of this mechanism has been proposed, where Oxygen ion migrates filling a vacancy site and Hydrogen ion is located in an adjacent interstitial site [30]. Finally, after secondary ion mass spectroscopy studies of samples exposed to isotopically enriched water, it was found that moisture diffusion into zirconia occurs by parallel but independent diffusion of H and O ions, while the transport of either water molecules or hydroxyl ions was excluded [31].

It has been shown that the strong variability of zirconia sensitivity to *in vivo* degradation is a consequence of the strong influence of microstructure and processing conditions on LTD [32]. Many variables play a role in LTD and can modify the resistance of the material to this phenomenon. The most important are:

- Density and porosity distribution: the presence of interconnected porosity around the original granules may allow percolative transport of the external moisture inside the body and accelerate LTD [7]. Moreover, the presence of regions with non uniform density may lead to stress concentration, damage and slow crack propagation [33].

- Phase separation: the presence of the cubic phase is likely to allow the formation of locally Yttrium depleted tetragonal (t) grains close to the cubic ones; these t grains are less stable and act as nucleation sites for the t–m transformation [34].

- Residual stresses: the local stress state seems to play a dominant factor governing grain stability, so everything that leads to a state of tensile stress into the material, both at the micro- and macroscopic level, may affect negatively LTD. Stresses can be induced, for example, after heavy machining or careless polishing [35], while grain coarsening and thermal anisotropy contribute in generating thermal stresses [36].

- Grain size: there seems to be a critical value of tetragonal grain size D_c below which the water-enhanced transformation does not occur, and it becomes more active with increasing grain size [36] (see Figure 1.8). However, this grain size is strongly related to composition and therefore is different for each zirconia ceramic [37].

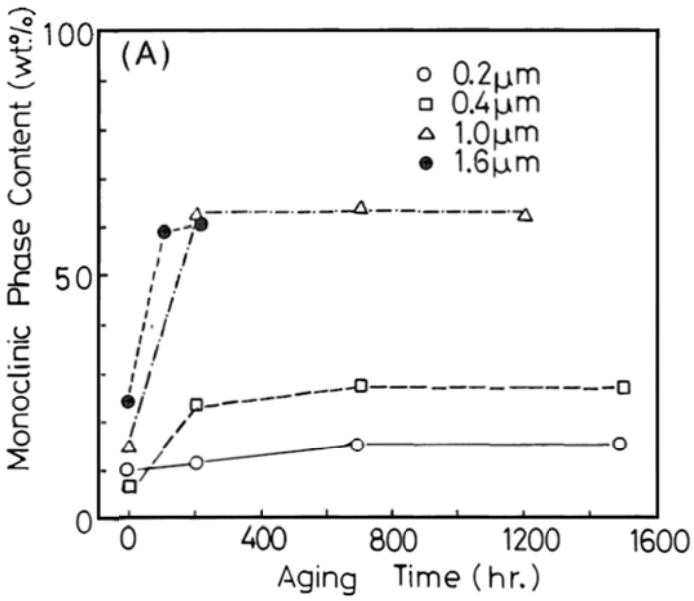

Figure 1.8. Surface phase transformation of 3Y-TZP zirconia aged at 230ºC in air [38], as observed for different grain sizes.

- Stabilizer type and content: with increasing yttria content, the critical grain size increases [37], although the toughening mechanism is strongly inhibited. Zirconia with other stabilizers, like ceria, is less susceptible to LTD despite of the increased grain size typical of Ce-TZP ceramics (see section 1.8.1).

- Composition and homogeneity: a powder with more inhomogeneous yttria distribution is more easily transformable than one with constant composition. Moreover, the presence of an intergranular glassy phase can increase the aging resistance [6]. Also, the presence of small quantities of alumina (typically between 0,25 and 0,5 mol%) has been proved to increase considerably the LTD resistance [39].

- Aging temperature and environment: aging occurs between room temperature and T_0, with the maximum rate at 250ºC for 3Y-TZP; the transformation rate increases with increasing vapor pressure, but the saturation level remains constant [37]. Moreover, when the transformation has been initiated by water vapor, autocatalytic propagation occurs. No transformation is detected in vacuum [40].

1.7. Mechanism and kinetics of LTD

As said before in section 1.6, transformation during LTD is likely to be due to the increase of internal stresses associated with the penetration of water radicals, where oxygen is located on the vacancy site, and hydrogen on an adjacent interstitial site.

These radicals produce a lattice contraction that results in the formation of tensile stresses in the surface grains and modify the oxygen configuration around Zr, increasing oxygen overcrowding; both effects destabilize the *t* phase by reducing ΔU_{SE} and ΔG_c in eq. 1.1 [30]. The diffusion of water radicals is easily permitted in Y-TZP, more than in other ceramics, by the strong presence of oxygen vacancies due to the trivalent character of Yttrium. The transformation also requires a cooperative interaction between many Zr ions; this may be a critical event for the nucleation of the monoclinic phase [32].

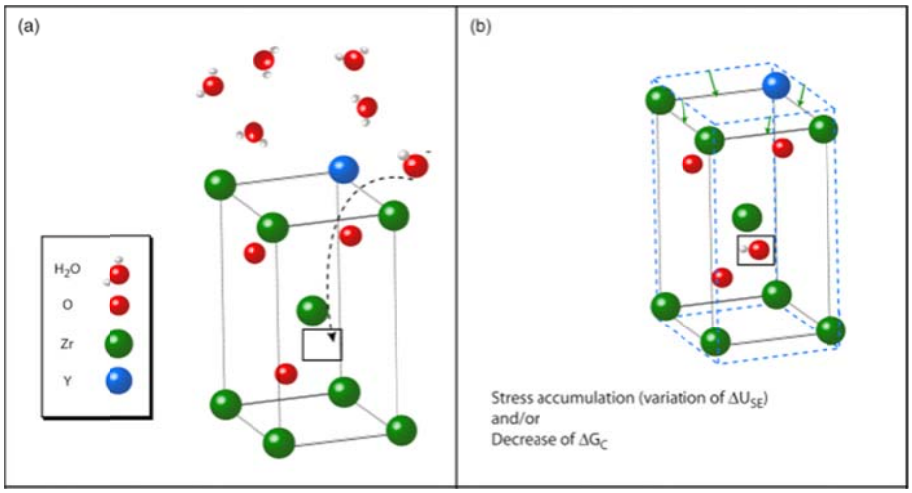

Figure 1.9. First steps of LTD by Chevalier *et al.* [7]. The figure shows the diffusion of water species (a) and the consequent variation of lattice parameters (b).

At the beginning of degradation, the transformation starts at the surface, mostly at grain corners where the internal stresses are bigger, and the volume change is relaxed at the free surface with the production of uplifts. This change is accompanied by displacements and shear stresses that can generate micro-cracking along the grain boundaries. The transformation follows a nucleation-and-growth mechanism, first from grain boundaries and triple points to the rest of the grain and then to adjacent grains. This mechanism was confirmed by optical interferometry [41] and by atomic force microscopy (AFM) [42]. The kinetics of surface degradation as measured by XRD is well described by the sigmoidal law of Mehl-Avrami-Johnson (MAJ) [43], where the grade of nucleation is constant and the diameter of the transformed centers are constantly increasing [41]:

$$\alpha = 1 - \exp(-(bt)^n) \tag{1.3}$$

where α is the fraction of tetragonal that has transformed to monoclinic phase, *t* is the time of exposure to moisture and the value of the constant, *b*, and the exponent, *n*, depend on temperature. Figure 1.10-a reports an example of application of the MAJ law.

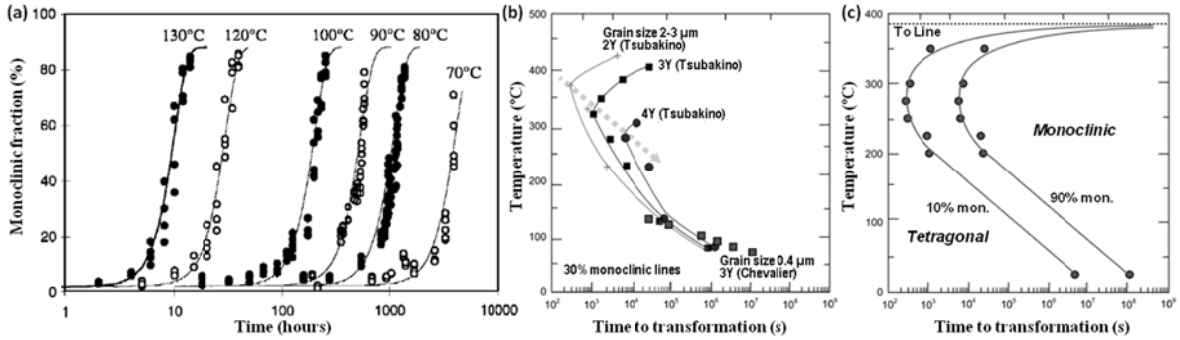

Figure 1.10. (a) Degradation kinetics in terms of monoclinic content vs. time measured on 3Y-TZP by XRD for different degradation temperatures. Curves have been fitted with the MAJ law and n=36. Adapted from ref. [41]. (b) TTT curves at 30% monoclinic content for TZP with 3 different yttria contents (ref. [44]) and for 3Y-TZP with smaller grain size measured by XRD. Adapted from ref. [7]. (c) TTT curves for 2,8 mol% Y-TZP thermal barrier coating at the beginning and end of transformation measured by Raman spectroscopy. Adapted from ref. [45].

The transformation kinetics forms C-shaped curves in a time-transformation-temperature (TTT) plot that can be interpreted in terms of competition between nucleation and grow rates (see Figure 1.10-b and -c) [44]. Well below the "nose" of such curves, the kinetics follows an Arrhenius law:

$$b = b_0 \exp(-\frac{Q}{RT}) \tag{1.4}$$

where b_0 is a constant, R the gas constant, T the absolute temperature and Q the activation energy, which is estimated to be close to 100 KJ/mol, a value similar to the activation energy for oxygen vacancy diffusion.

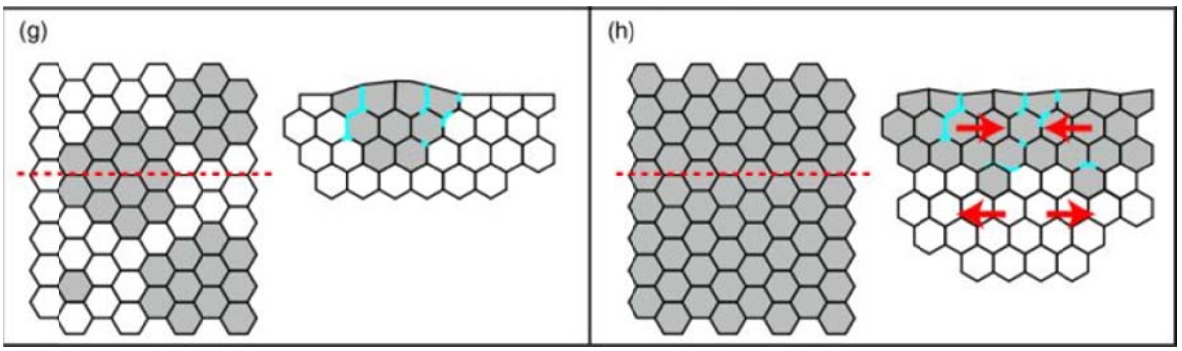

Figure 1.11. Growing of the transformed layer and extension of the degradation to the underlying layer due to water penetration and consequent rising of tensile stresses. Reproduced from ref. [7].

Once the surface grains are entirely transformed the process can progress because the water can penetrate through micro-cracks destabilizing the underneath grains. Moreover, the expansion of transformed grains generates a compressive state in the surface monoclinic layer and, as a consequence, tensile stresses in the underlying layer of tetragonal grains (see Figure

1.11). It is an autocatalytic reaction that leads to the acceleration of the transformation and thus to the second phase of the sigmoidal kinetic relationship [6].

1.8. Increasing LTD resistance. New zirconia-based materials

Many methods have been proposed to reduce or avoid LTD in TZP zirconia [6], [19], [37], [46]–[48]. The first and most important recipe is a better control of the process in terms of residual stresses, grain size, density and pore distribution. It is widely recognized that, even if the ISO standards are followed for implant production [49], the result in terms of LTD in actual parts is sometimes erratic, so better standards are required in order to achieve an improved aging resistance [35]. Doping Y-TZP with other oxides, such as magnesia or ceria is also a promising way to avoid LTD degradation.

It has been shown, for example, that Mg-PSZ is less susceptible to LTD [50] , but the strength of this material is significantly lower [17]. The case of ceria-stabilized zirconia deserves special attention in the context of this thesis.

1.8.1. Ceria-stabilized zirconia

Figure 1.12 shows the (*t–m*) transformation kinetics of zirconia stabilized by 10 mol% CeO_2 (10Ce-TZP) aged at 134ºC, 2 bars. This composition, which is fully tetragonal at the sintering temperature, is far more resistant to LTD than the corresponding YSZ compositions. In the case of ceria as a stabilizer, due to the tetravalent character of Ce^{4+} ion that forms solid solution with zirconia (see Figure 1.13), the vacancy mechanism is not operative, and therefore the stabilization of the tetragonal phase given by Ce^{4+} is imputable to its oversized dimension with respect to Zr^{4+}. According to Lin *et al.*, in this case the dilation and the 8-fold Oxygen coordination promoted by the dopant decreases Oxygen overcrowding around Zirconium ions and stabilize the tetragonal phase [22].

However, both 10 Ce-TZP and 3Y-TZP have almost the same *t–m* transformation temperature (T_0 in Figure 1.2 and Figure 1.13), implying that the driving force for the *t–m* transformation is approximately similar. Therefore, materials with the same driving force for LTD (that can be estimated in terms of T_0) can exhibit very different LTD kinetics [7], [46].

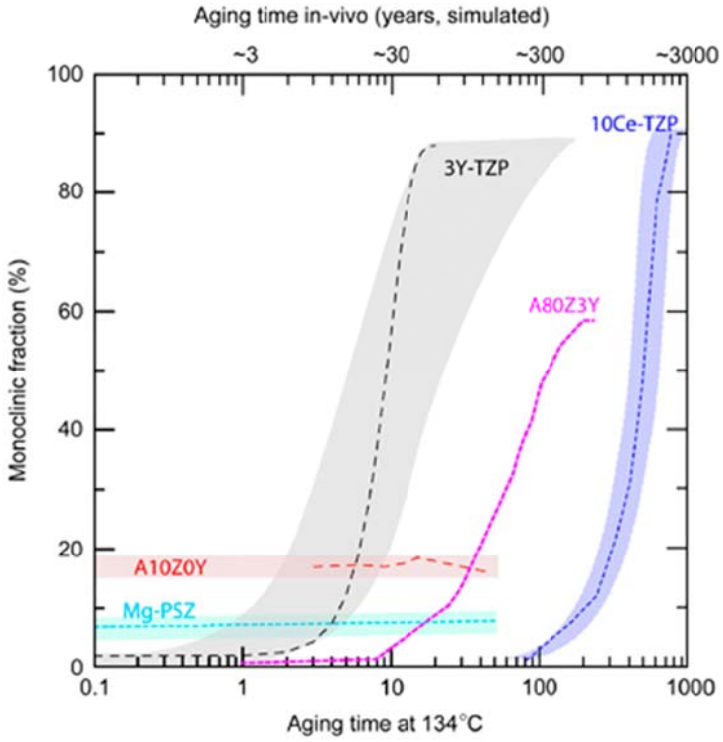

Figure 1.12. LTD kinetics of 10Ce-TZP, 3Y-TZP, Mg-PSZ, alumina-toughened zirconia (A80Z3Y), and zirconia-toughened alumina (A10Z0Y) measured at 134 ºC and expected at 37 ºC (from Chevalier *et al.* [7]).

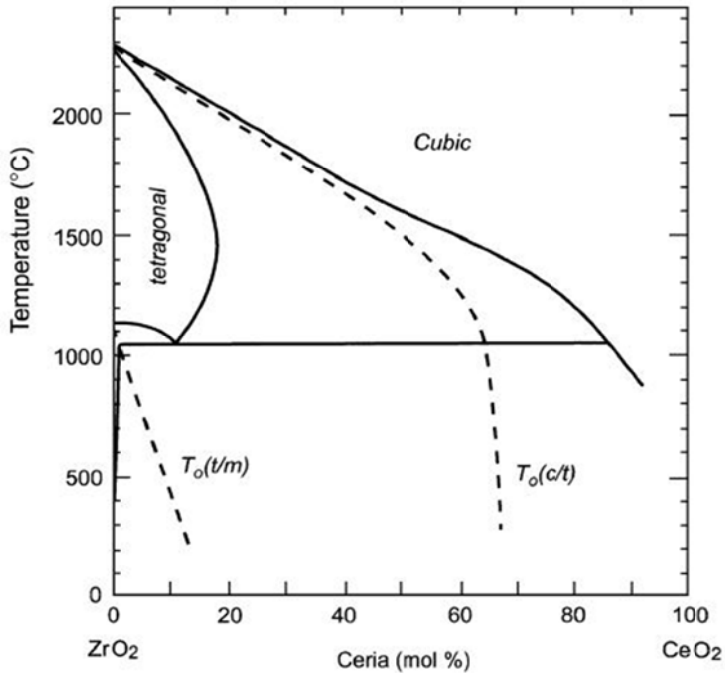

Figure 1.13. Zirconia–ceria phase diagram, from Yashima *et al.* [51]. Dashed lines represent the temperatures for non-equilibrium transformation

The main difference of ceria-stabilized zirconia (Ce-TZP) from YSZ is that, for the Ce^{4+} oxidation state, vacancies are not required for electrical charge compensation. The first steps of degradation, which require diffusion of water species, may thus be blocked and this could explain why aging is strongly retarded. Nevertheless, LTD is still happening in Ce-TZP,

with a very sluggish kinetics, so the explanation offered is not sufficient. Probably, in this case the vacancies naturally present in zirconia lattice at room temperature or retained after sintering are responsible for inducing the degradation. The presence of a limited amount of Ce^{3+} ions is also not to be excluded [52]. Other authors state that ceria apparently segregates into grain boundary or produces a thin film of CeO_2 on the surface of the sample, preserving Y-TZP "active points" that would be responsible for initiating LTD [48]. Even though the segregating behavior of Ce in a thin (2-4 nm) superficial layer at high temperatures has been observed elsewhere [53], it was also reported that the segregating ion was mainly at the trivalent state and that Y is the main segregant. Hence, the ceria "coating" explanation lacks of consistency and the vacancies mechanism seems more reasonable.

A further advantage is that with appropriate processing, the fracture toughness of the 10 and 12Ce-TZP materials is comparable with or greater than that of 3Y-TZP [7]. Adding Ce to Y-TZP increases the grain size and somehow reduces the sintering capabilities of the material leaving some residual porosity, but the aging resistance is significantly improved [54]. Mechanical properties are more influenced by the grain size and residual defects than by the amount of Ce itself. Because Ce-TZP is biocompatible (it is already used for dental restorations), Ce-Y-TZP could represent an attractive biomedical grade of zirconia. Following the results of Tsukuma and Shimada [55], the fracture strength of Ce-TZP reaches its maximum with a content of 10-12 mol% CeO_2, reaching 800 MPa. On the other hand, the maximum reported strength for Ce-TZP is usually lower and this behavior is valid only for pure Ce-TZP, while the presence of others stabilizers, for instance yttria, strongly affects the optimum Ce concentration for higher strength, as shown in Figure 1.14. [46], [47].

The optimum ceria content for resistance depends strongly on the yttria content. According to ref. [46], an optimum composition region exists in the range of 6,5 – 7 mol% CeO_2 and 2,25 – 3 mol% $YO_{1,5}$, exhibiting high strength of 750 – 900 MPa, high toughness of 10 – 17 MPa·√m, and moderate resistance to LTD. Unfortunately in these conditions the strength is still lower than that of 3Y-TZP if processing is not changed. The map shown in Figure 1.15 summarizes the behavior in terms of strength and fracture toughness as a function of yttria and ceria contents. By looking in the same plot, it appears that the high toughness (and transformability) generally means low resistance to LTD, *i.e.*, the two behaviors are roughly opposite, while this is not true in terms of strength vs. LTD resistance. Therefore, any choice of a new alloy will be confronted to a challenge: decreasing LTD sensitivity without decreasing too much the transformability, *i.e.* the T_0 (*t/m*) line [7].

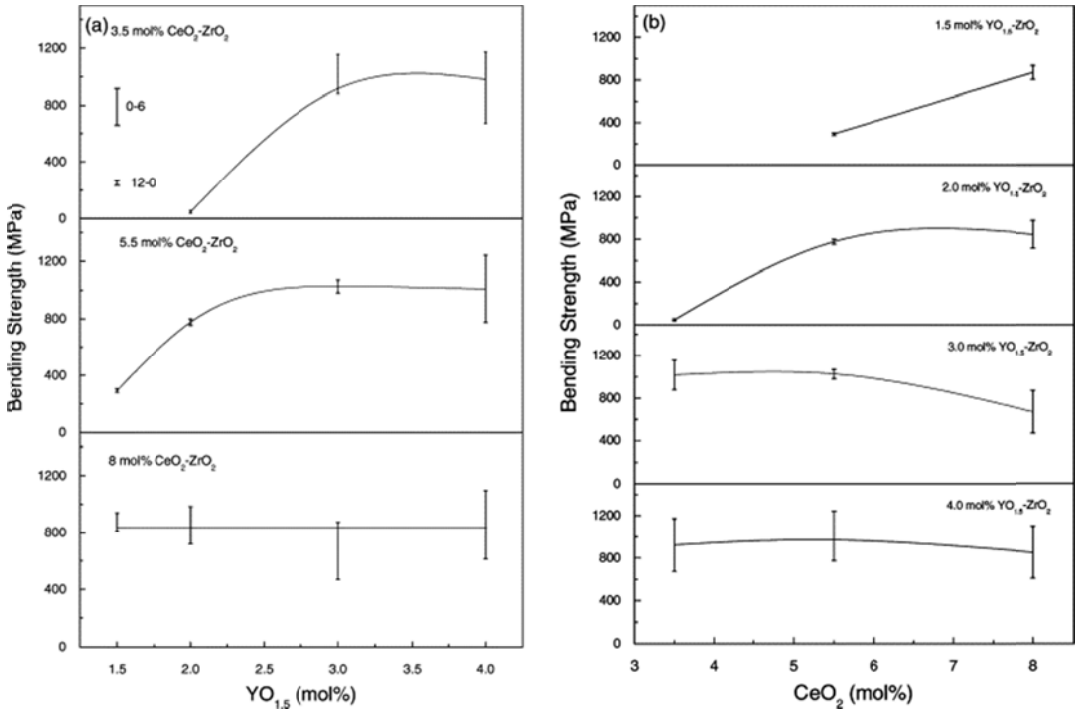

Figure 1.14. Correlation of three points bend strength and CeO_2 contents in terms of $YO_{1,5}$ content, from Lin *et al.* [47].

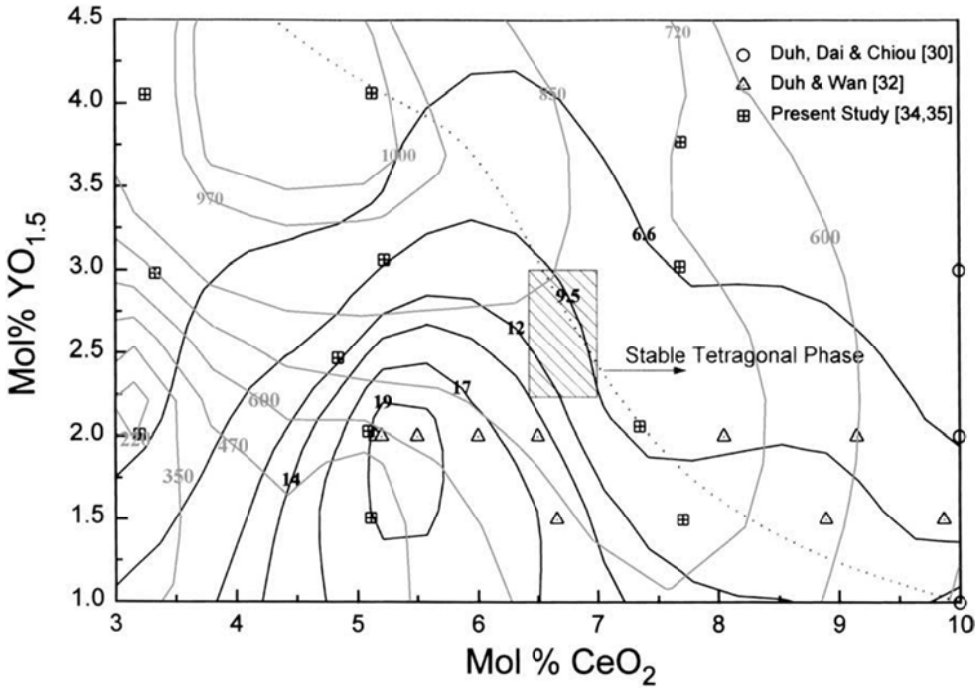

Figure 1.15. Map of flexural strength (grey lines, MPa), fracture toughness (black lines, MPa·√m) and composition of various Y-Ce-TZP samples. The dotted line indicates the composition boundary between stable and unstable t phase after 1000 h hydrothermal aging at 200ºC, while the dashed square indicates the optimum composition region according to Lin *et al.* [46].

Zhao *et al.* studied the possibility to create a Functionally Graded Material (FGM) in which the composition varies from totally Ce-TZP and totally Y-TZP together with aging resistance and mechanical properties. In this way, a higher Ce content in the surface can avoid

LTD, while the bulk resistance can be saved. They employed the electrophoretic deposition technique with good results [56], while Marro *et al*. [57] have followed the same approach by pressing a layer of CeO_2 powder on the surface of the dense 3Y-TZP followed by annealing. In both cases, LTD was prevented on the Cerium-rich face, where surface mechanical properties were strongly enhanced after artificial degradation with respect to the Y-TZP material.

1.8.2. Zirconia/alumina composites

Since 3Y-TZP femoral heads were retrieved from the market, manufacturers have tried different way to produce new reliable ceramic implants. Nowadays, the most successful zirconia based materials capable of overcoming the LTD problem are represented by zirconia/alumina nanocomposites, which are being distributed by various companies. These composites are divided in two main categories: materials where the main phase is alumina (zirconia-toughened alumina) and materials where the main phase is zirconia (alumina toughened zirconia).

1.8.2.1. Zirconia-toughened alumina

In these materials, tetragonal zirconia stabilization is achieved thanks to the high stiffness of the alumina matrix. Even though zirconia grains in ZTA are likely to be in net tensile stress after processing as a result of thermal expansion mismatch, the stiffer alumina matrix increase the ΔU_{SE} value in eq. A.1, decreasing the free energy for phase transformation. Therefore, little or no presence of stabilizer is necessary and the amount of vacancies in zirconia is strongly reduced, with the result that the diffusion of water radicals is retarded and aging is strongly delayed or totally avoided. If percolation threshold (approx. 16%) is not surpassed, the transformation cannot take place, limiting the phenomenon to the superficial layer [26]. When the percolation threshold is exceeded, aging has been observed [58]. The function of zirconia dispersed transformable grains is to increase fracture toughness, since the transformation toughening mechanism in presence of cracks is still active. In this way, the incidence of fracture of these materials with respect to the sole alumina is reduced [59]. Another function is to limit the grain growth of alumina, increasing its strength.

Nowadays, all the major companies that produce all-ceramic systems for arthroplasty have developed ZTA materials with approx. 15-20% of tetragonal zirconia, since this is the more reliable material for such delicate applications and the failure rate is very low.

Nevertheless, the production of such high strength composites involve at least one sintering in air and one HIP treatment to avoid the presence of defects

1.8.2.2. Alumina-toughened zirconia

It was reported, already in 1993, that the addition of small quantities of alumina to zirconia have the effect of retarding hydrothermal degradation [44]. According to Sato *et al.* [60], alumina grains play a major role in resisting the volume expansion of zirconia grains during transformation. At the same time, alumina was found to be beneficial for strength enhancement of Y-TZP [61]. On the other hand, other authors claim that the presence of alumina create internal stresses which are detrimental for aging resistance [36]. After these controversial results, in more recent works it was confirmed that both grain size and silica content at grain boundaries are affected by the addition of alumina. Typically, the addition of certain volume fractions of alumina reduces the grain size of zirconia [7] and reduces the saturation value of monoclinic content and increase the bending strength [62]. Nevertheless, it seems that hot isostatic pressing is necessary for obtaining well sintered parts. Currently, ATZ is produced by few companies (Mathys Orthopadie, Germany, among others) and also employed in THA.

1.9. Small-scale testing

Up to few years ago, only few approaches were suitable for determine mechanical properties of surface regions or reduced volumes. The most popular of these is represented by nanoindentation.

1.9.1. Nanoindentation

This practice performs an indentation while registering load and displacement, obtaining a curve similar to the one shown in Figure 1.16, which can be modeled with several methods after knowing the indenter geometry and some material properties. In this sense, the most used method is the one introduced by Oliver and Pharr in 1992, which permits the extraction of the sample hardness and elastic modulus after measuring the unloading stiffness [63]. The contact depth h_c is estimated from the load-displacement data and, taking into account the area function of the indenter, $A=f(h_c)$, the projected contact area can be calculated and hardness measured:

$$H = \frac{P_{max}}{A} \tag{1.5}$$

The contact stiffness $S = dP/dh$ is defined as the slope of the upper portion of the unloading curve during the initial stages of unloading. At the same time, elastic modulus can be calculated from contact stiffness value, knowing the Poisson's ratio of the material and elastic properties of indenter tip:

$$S = \beta \frac{2}{\pi} E_{eff} \sqrt{A} \tag{1.6}$$

$$\frac{1}{E_{eff}} = \frac{1-\nu^2}{E} + \frac{1-\nu_i^2}{E_i} \tag{1.7}$$

where β depends on the indenter tip geometry and is equal to 1.034 for a Berkovich tip and E_{eff} is the effective elastic modulus, which takes into account the fact that elastic displacements occur in both the specimen, with Young's modulus E and Poisson's ratio ν, and the indenter, with elastic constants E_i and ν_i. A well known example of nanoindentation system is presented in Figure 1.16, together with a simplified diagram showing the main components.

Moreover, in modern nanoindenters the stiffness can be measured continuously as a function of penetration depth by simultaneously superimposing an oscillating force with amplitude generally several orders of magnitude smaller than the nominal load and analyzing the response of the system by means of a frequency specific amplifier. This system is called Continuous Stiffness Measurement (CSM), which allows measuring the progressive variation in superficial mechanical properties when the substrate the surface is in a different state with respect to [64].

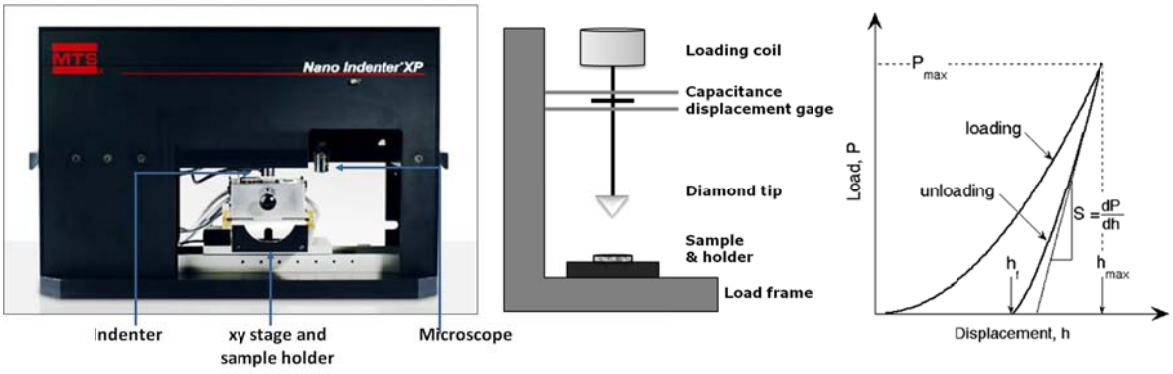

Figure 1.16. From left to right: MTS Nanoindenter XP with the main parts indicated, nanoindenter simplified scheme and typical load-displacement curve obtained with nanoindentation.

Nanoindentation can be also used to estimate several other properties like fracture toughness, viscoelastic parameters or yield stress. This technique determines properties with a sub-nanometer resolution, and it is specially suited for assessing thin surface layers and different microstructural phases. However, nanoindentation measurements are done under contact loading, which implies a non-homogeneous complex triaxial stress state, with an important hydrostatic stress component, which may not be representative of the in-service conditions.

1.9.2. Novel small-scale techniques

Since the introduction of devices capable for machining, handling and testing samples with dimensions in the range of micro- and nano-meters, new techniques have been developed in order to assess materials properties at these scales and understand better their behavior. These techniques as often referred to as "small-scale testing". Small-scale testing has lately become an important tool for understanding deformation, strengthening and failure mechanisms at small scales.

The intrinsic or "intensive" properties of materials, *i.e.* not size dependent, which are normally measured through standardized testing, start to exhibit an extrinsic behavior if the volume of material tested is reduced down to the level of the micro- or nano-scale. This is true at least for metallic monocrystals, where diverse experimental approaches have shown that the ultimate strength strongly increases when the volume of material is in the micro-nano range.

During late 80's, it was shown that the strength of thin films is inversely proportional to film thickness. Nevertheless, this phenomenon is related to the constraining effect of surrounding layers and not only related to the size [65].

The size effect was first observed by Fleck *et al.* [66] in copper wires, as showed in Figure 1.17. The authors explained the observed behavior in terms of the strain gradient theory, which states that stress is both function of strain and strain gradient.

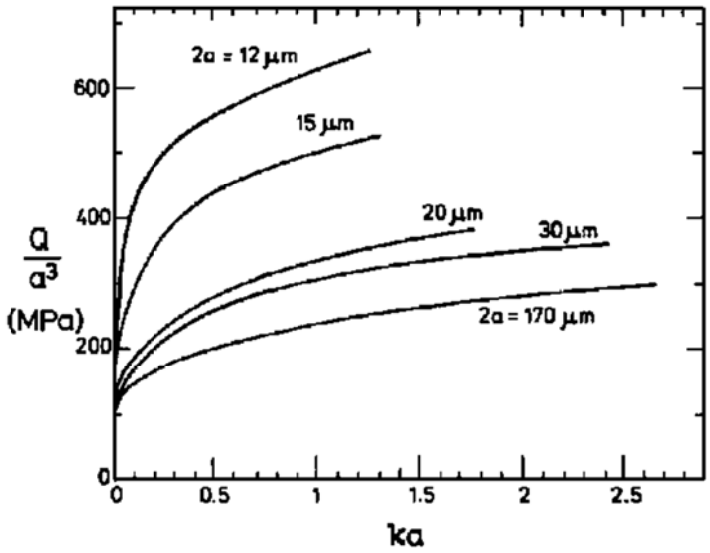

Figure 1.17. Torsional response of copper wires of diameter 2*a* in the range 12-170 μm. *Q* is the torque, *a* the wire radius and *k* the twist per unit length. If the constitutive law were independent of strain gradients, the plots of normalized torque Q/a^3 vs. ka would all lie on the same curve. Reprinted from ref. [66].

The main idea of this theory is, keeping it simple, that the higher strain gradient for smaller sizes imposes the generation of many geometrically necessary dislocations, which are responsible for the increase in yield stress. Some years later, a similar behavior was found in bending thin foils [67].

After these findings, several authors started to study the effect of the "small scale" to material properties. During the 90's, numerous nanoindentation experiments showed the existence of an inverse relation between hardness and indentation depth, leading to the strain gradient plasticity law developed by Nix and Gao [68].

According to the authors, the reciprocal of indentation depth and the square of the hardness are linearly related. In all these results, increase in flow stress was related to the strain gradient, meanwhile Horstemeyer *et al.* [69] showed by molecular dynamics simulations that also with no presence of strain gradient a power law scaling effect for fcc metals was possible, suggesting that dislocation nucleation could be considered as an explanation for plasticity size effects.

The research addressed at investigating size effects turned towards testing of materials in absence of strain gradient, starting a series of studies involving micro-pillars compression. Nevertheless, other small scale testing techniques have been employed during recent years, which are not only designed for investigating size effects but rather in order to assess the mechanical response of small volumes, thin films, individual microstructural constituents of hybrid materials and microcomposites. Among these techniques, the ones that concern us for

the characterization of TZP materials surface are micro-cantilever testing and determination of micro-fracture toughness.

In the following sections, a summary of the findings related to small-scale testing in the last decades will be presented.

1.9.3. Micro-pillar compression and size effects

The first size-effect in micro-pillar compression was experimentally detected by Uchic *et al.* [70] [71]. They milled micrometric pillars of different sizes with the aid of Focused Ion Beam (FIB) and tested them in compression ex-situ (outside the FIB chamber) by using nanoindentation technology (an MTS Nanoindenter XP) and a homemade flat-punch diamond tip. As a result, they observed a dramatic size effect on strength for a Ni_3Al-1% Ta alloy deforming under nominally single-slip conditions, as shown in Figure 1.18.

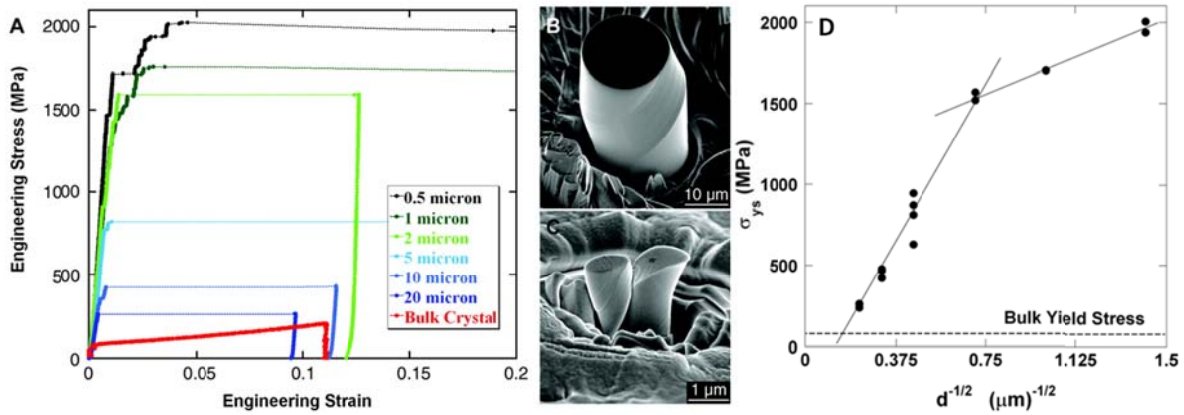

Figure 1.18. Compression behavior at room temperature for pure Ni microsamples having a ⟨134⟩ orientation. A: stress-strain curves for pillars of different sizes and for bulk material. B, C: SEM images of 20 µm and 1 µm diameter pillars, respectively, after testing. D: dependence of the yield strength (σ_{ys}) on the inverse of the square root of the sample diameter for Ni_3Al-Ta. The transition from bulk to size-limited behaviour is predicted by the linear fitting at approx. 42 µm. From Uchic *et al.* [71]

The flow stress increased from 250 MPa for a 20-µm-diameter sample to 2 GPa for a 0.5-µm-diameter sample, following the general law:

$$\sigma = \alpha d^n \tag{1.8}$$

Where α is a constant and n is the power-law exponent, which was found to be dependent on the absolute magnitude of the stress [72].

These flow stresses were much higher than those found for bulk crystals, which themselves exhibit a flow stress of only 81 MPa. The size effect was associated to dislocation truncation and annihilation at the surface, especially for screw-type dislocations. This

correspond to the nucleation starvation model, where any sources and dislocations existing within a small sample are exhausted at low strains, allowing the stress to rise until surface nucleation is possible.

The first authors describing micro-pillar compression procedure in detail were again Uchic *et al.*, showing how the technique is appropriate for investigating size effects and activate single slip systems in monocrystals [73]. A variety of metals and intermetallics alloys such as Ni, nanocrystalline Ni, Ni-base superalloys, Ni3Al alloys, Zr-based metallic glasses, and TiAl were tested, with samples with size ranging from 0.5 to 43 μm in diameter. The same authors developed a procedure for reducing the taper effect associated to FIB milling in pillars from 2 to 20 μm in diameter: after placing a circular fiducial mark on the top pillar surface, a program automatically collect an image of the surface and then mill the pillar by "lathe milling" patterns with a fixed distance from the fiducial mark. For bigger diameters other techniques were suggested, like micro-electro-discharge-machining and laser ablation, while for smaller diameters they used only the annular milling pattern already available on the FIB dual station control program.

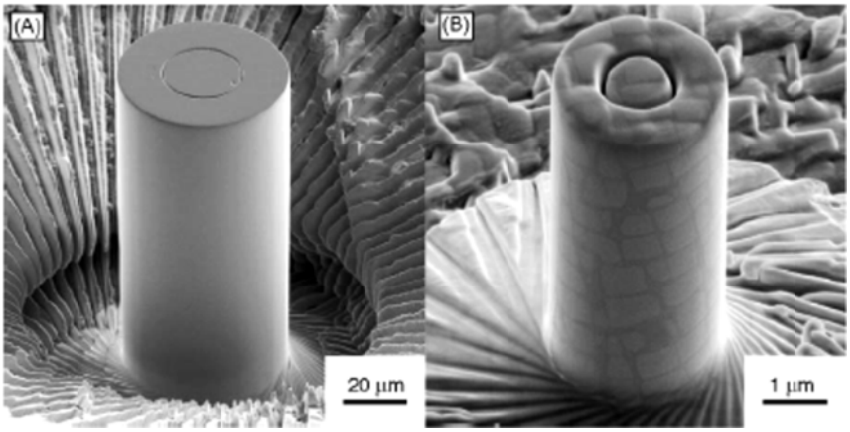

Figure 1.19. A: micro-pillar of 43 μm diameter milled by the lathe automated milling procedure into the surface of a $Ni_3(Al,Hf)$ single crystal. On the top of the pillar the fiducial mark can be appreciated. B: micro-pillar of 2.3 μm diameter milled into Ni superalloy (UM-F19) single crystal.

Other metallic systems, thin films and porous materials have been studied by means of micro-pillar compression. For comprehensive reviews of the results, the reader is referred to recent works by Kraft *et al.* [74] and Greer *et al.* [75]. As a general result, it was found that all the yield stress vs. pillar diameter curves would collapse on a linear relationship by plotting a normalized resolved shear effective stress instead of the simple yield stress, and that the exponent of equation 1.9 is approx. 0.6 for soft fcc metals [72]. The recent work of Korte *et*

al. shows that a reasonable equation normalized by the shear modulus of the material could be:

$$\frac{\tau-\tau_0}{G} = \beta d^x \tag{1.9}$$

Where d is the pillar diameter, τ the critical resolved shear stress along the slip plane, τ_0 the bulk shear yield stresses, G the shear modulus, and β and x the fitting variables. This analysis gives values of x that are dependent on the type of material investigated, as shown in the following picture.

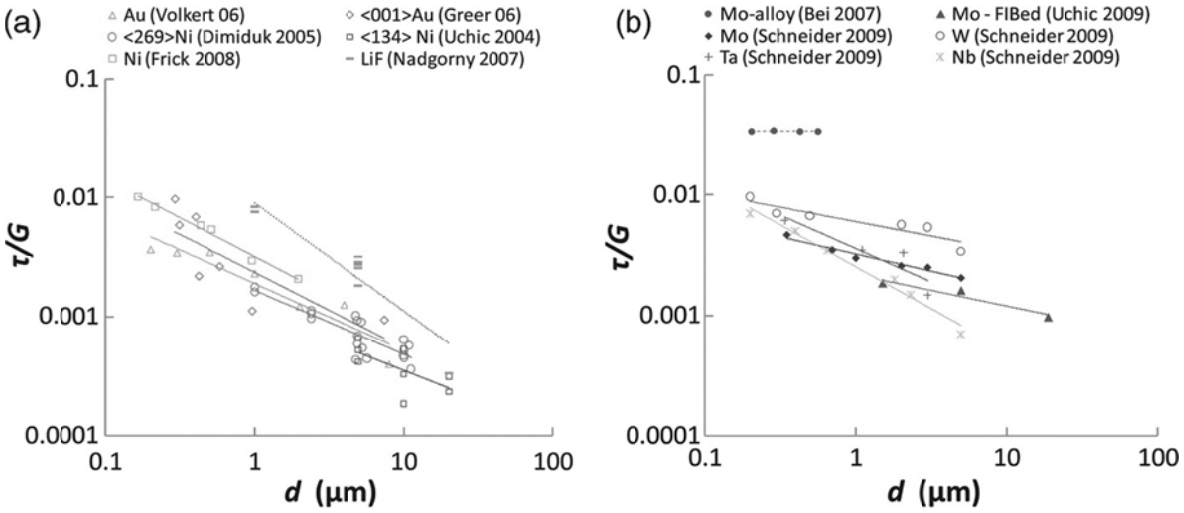

Figure 1.20. (a) Low lattice resistance (fcc metals and LiF) and (b) Intermediate lattice resistance (bcc metals) normalized shear yield stress vs. pillar diameter and power-law fit. Reproduced from ref. [76].

1.9.4. Small-scale testing of polycrystals

The situation is more complicated for polycrystalline small-scale samples. At these scales, both extrinsic and intrinsic contributions play simultaneously a role in the mechanical behavior, resulting in contrasting results observed by different authors. For example, it was shown that the "smaller being stronger" trend can be inverted in polycrystals depending on the ratio thickness/grain size, as explained in the case of nanocrystalline Nickel by Greer and De Hosson [75]. Leung and Ngan [77] concluded, after performing dislocation dynamics simulations, that sample size, grain size and dislocation density control the behavior, which can be classified in two types. The first is dominated by strain-hardening, according to the well known Hall-Petch law. In the second, plasticity is source-limited and the "smaller being stronger" behavior is expected. Figure 1.21(a) summarizes these concepts, showing the combined effects of sample size and grain size. In the intermediate region, opposite behaviors are found, as outlined in the chart in (b).

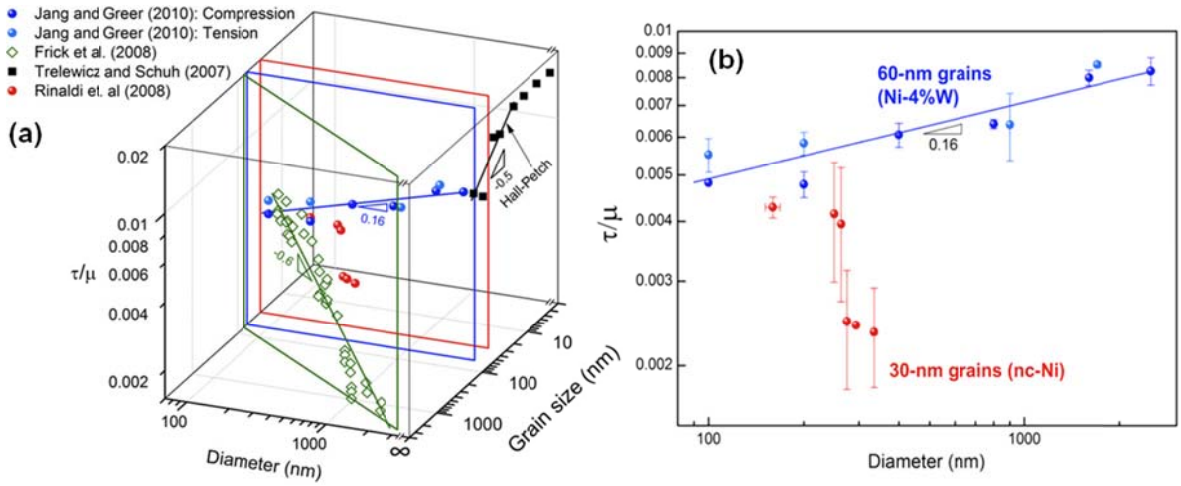

Figure 1.21. a) Extrinsic and intrinsic size effects for Ni and Ni-4%W, reproduced from Ref. [75]. b) opposite behavior of nanocrystalline Ni after Rinaldi *et al.* [78] and Jang and Greer [79].

1.9.5. Micro-pillar compression: results in ceramics

Micro-pillar compression in ceramics started after results in metals were well established, probably because of lack of dislocation mobility at room temperature, which is generally accepted for almost all ceramic systems in the bulk state. Nevertheless, it has been shown recently that micropillars of materials normally considered as brittle can be deformed plastically at room temperature.

Michler *et al.* studied the compression of GaAs at room temperature [80] and the brittle-ductile transition for the same material [81]. It was observed that under compression slip occurs, causing slip band intersections to form. In GaAs micropillars with diameter greater than approximately 1 μm, cracks nucleate at room temperature at these intersections and then grow axially in the sample. Below this size, axial splitting cannot occur at the yield stress, so that splitting is not observed (**¡Error! No se encuentra el origen de la referencia.**).

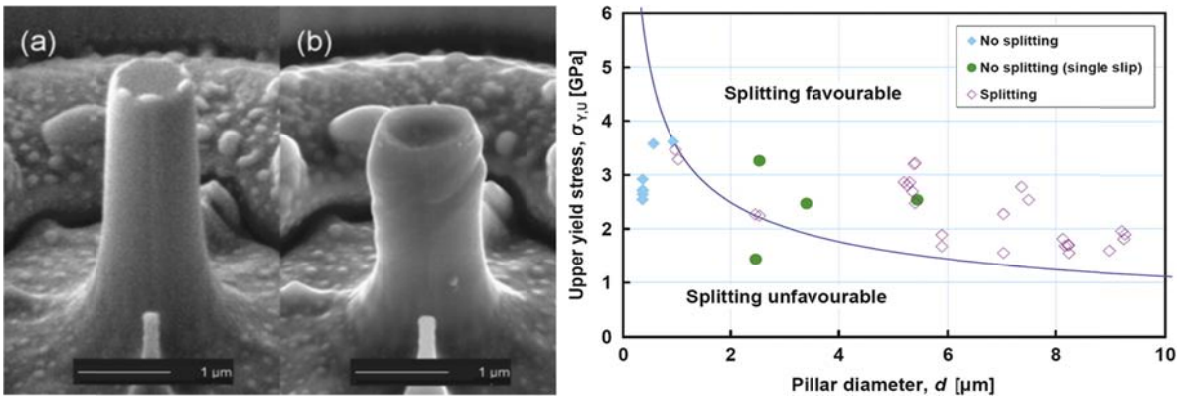

Figure 1.22. a) and b): GaAs micropillar before and after compression, showing the presence of slip bands. Reproduced from [80]. Right: yield stress vs. pillar diameter for GaAs, with the failure mode indicated. From ref. [81].

Ostlund and Korte studied the brittle-to-ductile transition of Si micropillars at room temperature [82], observing that the transition temperature, which for bulk silicon is around 550 ºC, drops to room temperature for samples with diameter between 310 and 400 nm (see Figure 1.23). At the same time, the fracture toughness is strongly enhanced for diameters below the critical value.

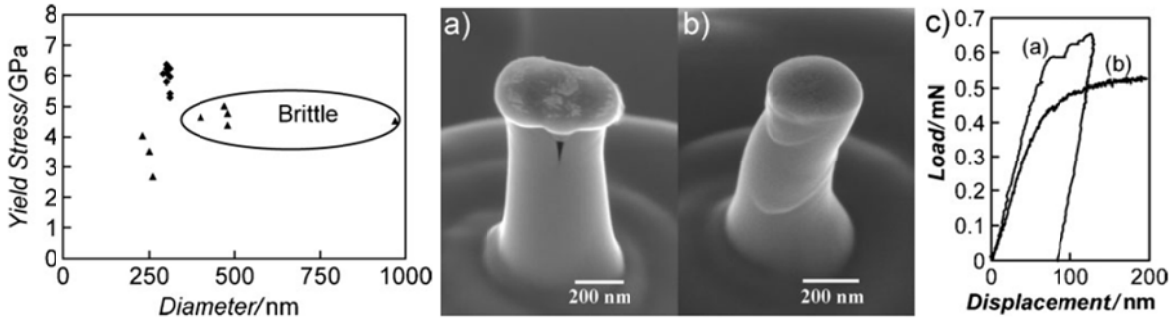

Figure 1.23. Left: yield stress vs. pillar diameter for Si micro-pillars of different sizes, tested *ex-situ* (triangles) and *in-situ* (diamonds). The circled pillars showed cracking, which is reflected in (a) picture and curve, meanwhile smaller pillars showed plastic deformation, reflected in (b) picture and curve. (a) and (b) pillars are 400 and 310 nm, respectively. Reprinted from [82].

Korte and Clegg first tested ceramic micropillars ($MgAl_2O_4$ spinel single crystal) at moderate-elevate temperatures, from 25 to 400 ºC [83], in order to facilitate plasticity. At room temperature they obtained brittle fracture but from above 200 ºC the deformation was clearly plastic and the pillars could be unloaded, showing slip traces. Yield stress decreased with increasing temperature but was higher than yield stress for macroscopic monocrystals under hydrostatic pressure, as shown in Figure 1.24.

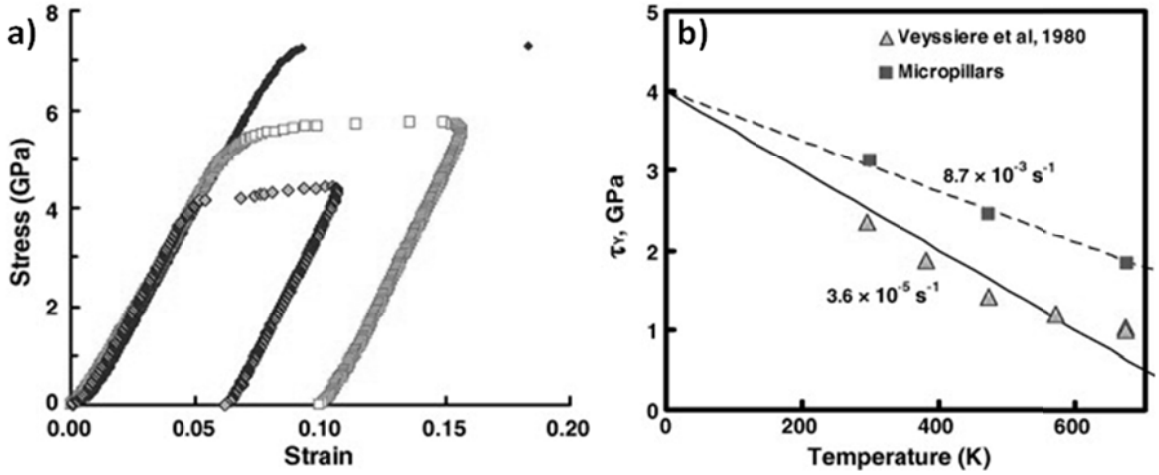

Figure 1.24. a) Stress-strain curves for spinel micropillars deformed at 25 ºC (filled diamonds), 200 ºC (open squares) and 400 ºC (open diamonds). b) Shear yield stress τy vs. temperature for <001> oriented bulk crystals (triangles, from ref. [84]) and micropillars (squares) at the shear strain indicated. τy changes with temperature at -5 x 106 PaK-1 (ref. [84]) and -3.17 x 106 PaK-1 (micro-pillars)

They stated that a value for the activation volume can be estimated that is consistent with that expected for thermally activated glide and that the values obtained from the bulk and the micro-pillar compression are consistent with one another; the differences being due to the differences in strain rate. This suggests that, in contrast to metals, the increase in flow stress observed in ceramics is negligible, presumably because the lattice resistance is much greater than in metals. Nevertheless, decreasing the sample size reduces the temperature at which plasticity is observed.

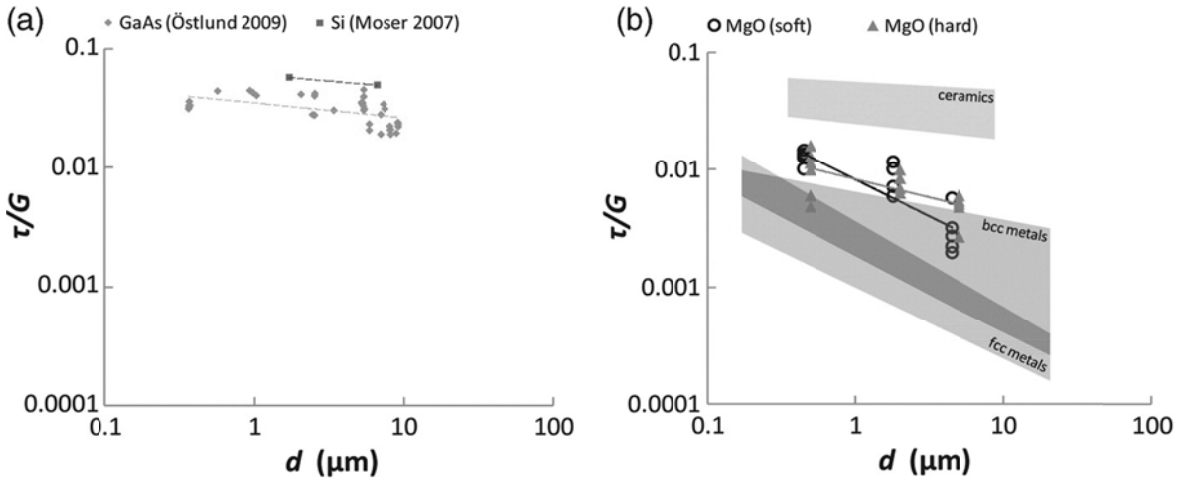

Figure 1.25. Normalized shear yield stresses and power-law fits for several ceramic systems. In (a) the results of refs. [82], [85] are showed, while in (b) a summary of metal and ceramic systems is represented, together with the results of Korte and Clegg [76], from which the charts are reproduced.

The same authors [76] showed later that micro-pillars obtained from ceramic monocrystals (MgO) tested both on soft and hard slip planes can be plasticized at room temperature, observing also an increase in flow stress with size reduction. This happens because cracking is a size-dependent phenomena which can be suppressed completely if the sample is small enough, as it was suggested by Kendall and Karihaloo [86], [87]. The results are summarized in Figure 1.25.

Stauffer [88] studied the nanoindentation and nano-compression behavior of Silicon monocrystalline nano-pillars and nano-spheres by in-situ TEM imaging. He observed that the deformation is the result of dislocation nucleation and long-range movement at high velocities at room temperature, because of the high stresses applied in the nano-pillars. Strain-hardening was observed, although this is normally not found when deforming nano-pillars due to dislocations exhaustion mechanisms at the surface. The strain-hardening exponent increased with repeated runs on Si nano-pillars and also with approximately the square-root of the sample diameter. This was explained in terms of the lower amount of nucleation sites at the

free surfaces as size decreases. Similarly, a decreased size could limit the mean free path of dislocation motion if all, or most of, the dislocations remain in the volume.

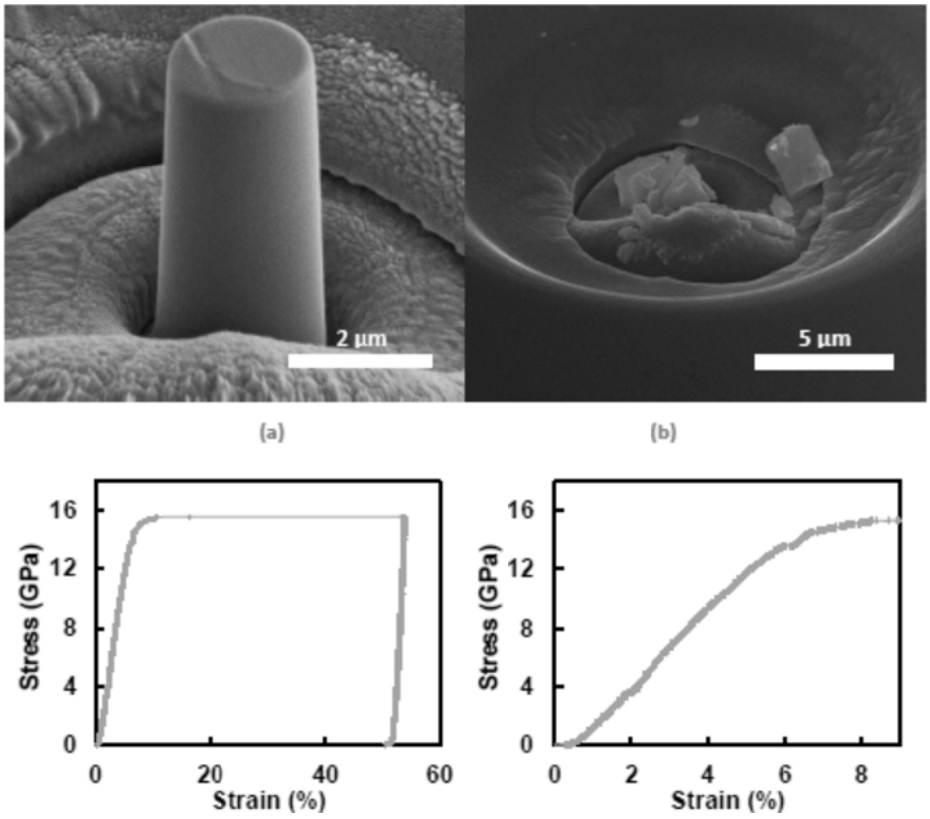

Figure 1.26. 2 µm TiC micro-pillar before and after testing, with the correspondent stress-strain curve, which is magnified in the last picture. From [89].

Howie [89] studied plasticity in TiC and LaB_6 monocrystals. In TiC compression along the 〈100〉 direction, the deviation from linearity was found at approx. 3.5 GPa. For bigger pillars (2 µm) the formation of slip traces could be observed occasionally, with failure occurring in brittle mode (Figure 1.26). Smaller TiC pillars (0.8 µm) showed clearly slip traces that correspond to displacements at constant load in the stress-strain curve (Figure 1.27). Moreover, the same soft slip system was activated in different tests. Greater scatter in strength was observed for smaller pillars, which was associated to variations in surface structure that may affect dislocation activation. By TEM observation of 0.8 µm pillars after testing, {110} slip planes could be observed. The soft slip system in TiC could be detected as {110}<1-10>, with CRSS of 4 GPa. A similar trend was observed for LaB_6 pillars, with the softest {111}<1-10> slip system activated at CRSS of 3.8 GPa. For both materials, size-dependent fracture behavior was clearly evident, with larger pillars fracturing more often and more completely than smaller ones.

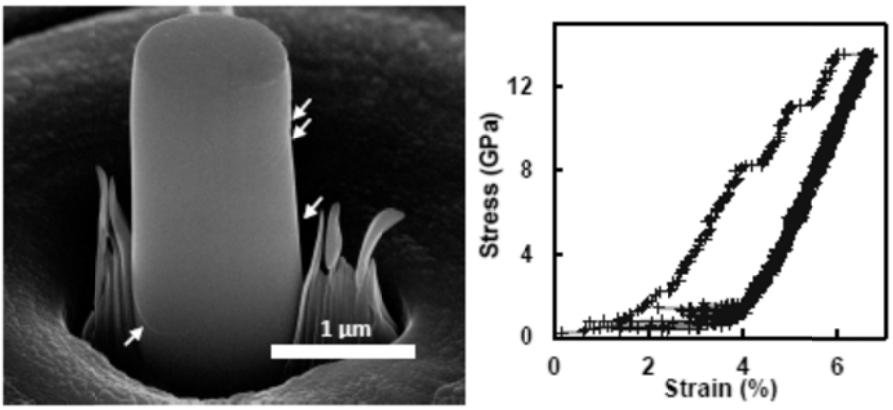

Figure 1.27. 0.8 µm TiC micro-pillar compressed around 6,6% strain, with the correspondent stress/strain curve. Slip bands are clearly visible. From [89].

The failure mechanism of TiC and LaB_6 micropillars were discussed in Ref. [90], observing three different failure modes, which result from dislocations interaction. Axial splitting nucleated at intersecting slip bands (which can be observed in Figure 1.23-a) was recognized as the most important mode for the brittle-ductile transition. A model of axial splitting was proposed, which explains the transition with the size dependence of the equations governing fracture (valid only if intersecting bands are forming). No size effect in the material properties is needed for this model, since it implies a reduction of the stress intensity factor with decreasing pillar size. The critical stress for axial splitting was defined as:

$$\sigma_S = \frac{K_{Ic}}{k_s \beta \sqrt{d}} \tag{1.10}$$

This implies a clear dependence on the pillar diameter *d*. Regarding the taper effect, Howie used the interpretation of Kendall [91] to show that the taper gives a contribution in deviating cracks, since ligaments tend to buckle. The driving force for this process is between 6% and 22% of the driving force for axial splitting with taper angles between 2º and 4º, respectively.

Gerberich [92] reviewed the scale effects observed on traditionally brittle materials. Size effects could be observed in terms of ultimate strength, fracture toughness, ductile-brittle transition and also cycles to failure in cyclic loading for materials such as Silicon and SiC. The underlying mechanism suggested is dislocation plasticity.

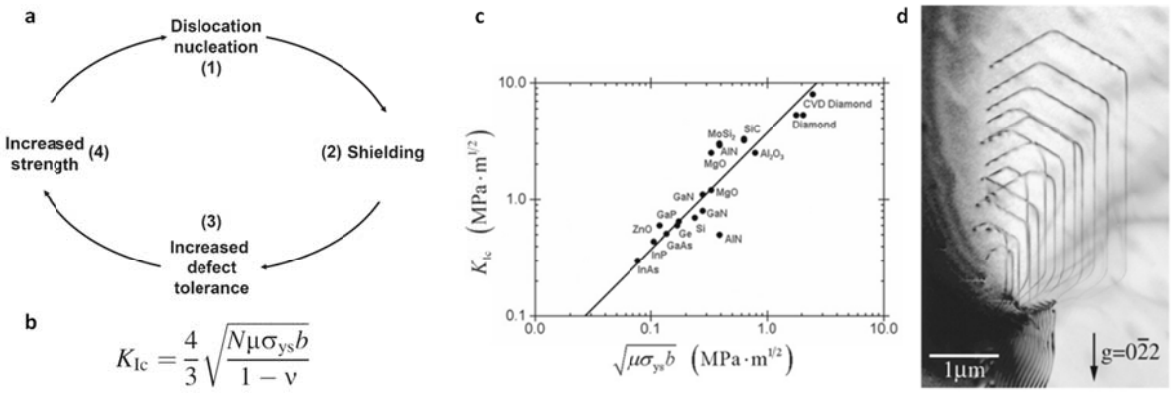

Figure 1.28. The dislocation shielding concept is outlined in (a), while (b) is the formula which relates K_{Ic} with the number of shielding dislocations N, the shear modulus μ, yield strength σ_{ys}, the Burger's vector b and the Poisson's ratio ν, from [93]. (c) Fit of 22 ceramic materials according to the model proposed. (d) Arrested crack in silicon single crystal with $N = 14$ shielding dislocations [94]. Pictures reproduced from Gerberich *et al.* [92].

Three factors apparently come into play allowing enhanced plasticity at small scale. First, small volumes, particularly single crystals, are relatively free of stress risers allowing high stresses prior to crack propagation. Second, very high stresses can nucleate dislocations at free surfaces in ceramics at low temperature. Third, the activation energy for nucleating a dislocation is much smaller at high stresses allowing both nucleation and propagation of dislocations to produce plasticity when normalized by structure size. Furthermore, they proposed the dislocation shielding concept to be responsible for increasing strength and fracture toughness at the small scales. Briefly, in small volumes of brittle materials the nucleation of dislocations at the surface with high stresses happens well below the stress that is necessary for small but sparse inherent defects to nucleate fracture. An equation for K_{Ic} was proposed and it was showed that the model holds valid for a series of materials.

Other examples of micropillar compression of high-strength ceramic monocrystals showing room temperature plasticity have recently been reported in sapphire [95], silicon carbide [96] and silicon nitride [97].

1.9.6. Phase-transforming materials at the small scale

Ueland *et al.* [98] described the effect of sample reduction on some Cu-based shape-memory phase-transforming alloys, which exhibit shape-memory effects when tested as monocrystals, but usually undergo brittle failure in the polycrystalline state. It was shown that the increase of the surface area with respect to the grain boundary area, when testing microwires of small diameter, leads to enhanced ability to transform without failure. This is

the result of a reduction in transformation strain incompatibilities at grain boundaries and triple junctions. These materials were named "oligocrystalline shape-memory alloys".

Single-crystals or oligocrystalline micropillars of zirconia highly doped with Ce and Y have been tested by Lai *et al.* [99], reporting shape memory and pseudoelastic effects. With the introduction of high quantities of dopants, the *m-t* reversion temperature was lowered below room temperature or few hundreds of degrees above it. In the first case, pseudoelasticity was observed, while the shape memory effect was found in the second case. These evidences are the results of stress-induced phase transformation, which produces a considerable strain (up to 8%) under loading, which is totally recovered during unloading of the pillar. In this case, the small-scale structure allows suppressing brittle failure by reducing the internal mismatch occurring during martensitic transformation. These pillars were able tu sustain loading cycles, showing a progressive thinning of the loading-unloading loop (referred to as "training" of the superelastic material), as shown in Figure 1.29.

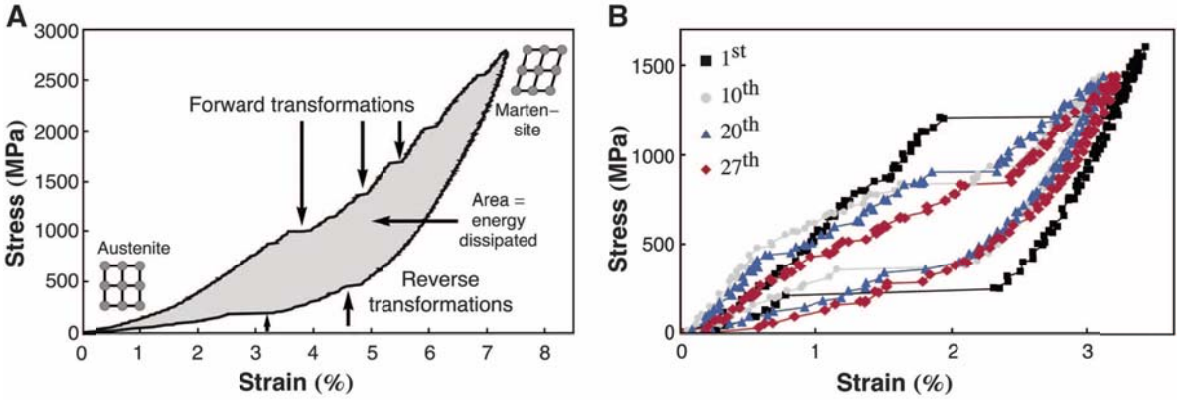

Figure 1.29. A) Pseudoelastic effect in tetragonal zirconia. B) Thinning of the loading-unloading cycles ("training"). Reproduced from Lai *et al.* [99].

1.9.7. Micro-cantilevers bending

The main limitation of micro-pillar compression technique is due to the stress state, which can only be compressive. A suitable method to create tensile states on small samples is represented by micro-cantilever testing. This technique involves the machining of small cantilevers samples and testing them in flexure.

In 1998, *in-situ* flexure testing of silicon cantilevers produced by etching processes (diffused pattern technique and anisotropic etching technique) was performed using a stylus with conical tip. No strain was measured, only the force on the stylus was recorded with a strain gauge directly on the lever supporting the stylus. In this way, failure stress could be obtained and flaw size was calculated from fracture stress [100].

McCarthy *et al.* produced for the first time FIB machined submicron-cantilevers for assessing thin films properties by measuring the cantilever deflection after milling. This time cantilevers were not tested but only the spontaneous deflection was measured and related to residual stresses [101].

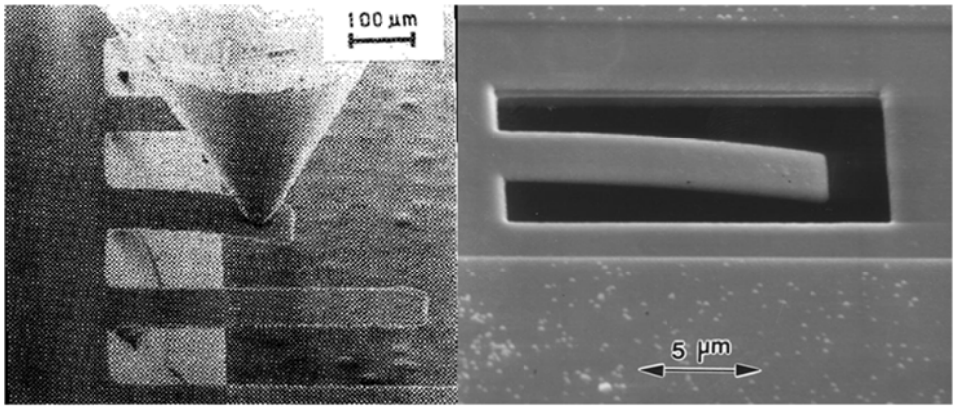

Figure 1.30. Left: *in-situ* fracture testing of silicon cantilevers by Johansson *et al.* [100]. Right: FIB machined micro-cantilevers by McCarthy *et al*. [101].

The specimen size-effect was evaluated for the first time with the micro-cantilever bending technique for polysilicon in 2001. Cantilevers were produced by etching and loaded *ex-situ* with a nanoindenter. The indentation effect and the deflection across the cantilever width were taken into account in order to calculate Young modulus. Fracture strength was discussed in terms of effective volume and surface-to-volume ratios between cantilevers with different sizes. No plasticity was observed [102].

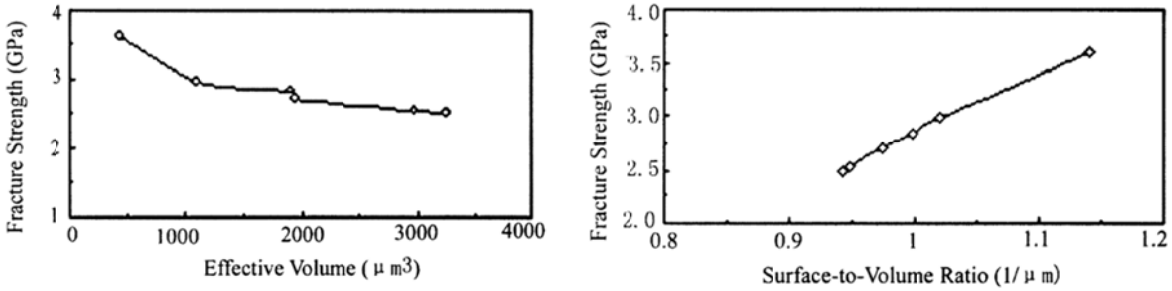

Figure 1.31. Left: fracture strength and effective volume of polysilicon cantilevers. Right: Fracture strength vs. surface-to-volume ratio of the polysilicon cantilevers. Reproduced from ref. [102].

Motz *et al.* [103] explored the mechanical properties of micro-sized copper beams milled by FIB, observing a strong size effects. To explain it, both the strain gradient plasticity and the limitation in available dislocation sources were invoked.

Micro-cantilever testing was employed in 2009 to measure the anisotropy in Young's modulus for copper single crystals [104]. Micro-cantilevers with different orientations in the plane were obtained by FIB milling and tested in flexure, recording load and displacement. In

the analysis, the extra deflection at the fixed end due to the not-fully-constrained condition was taken into account, stating that it should be considered for aspect ratios lower than 6. The elastic modulus was calculated both with single point and multiple point (loading/unloading at different distances from the fixed end for the same cantilever) tests.

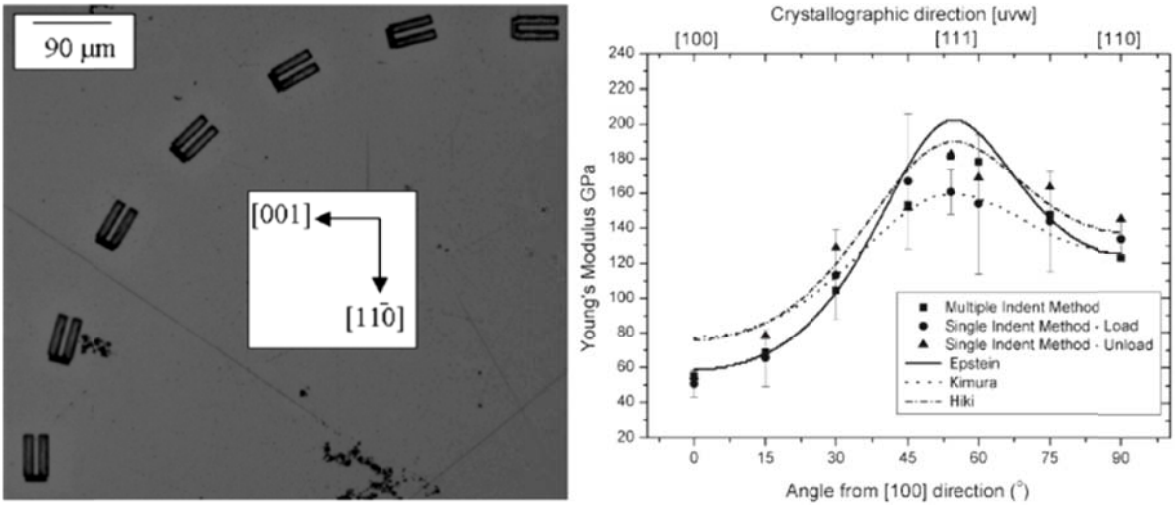

Figure 1.32. Left: micro-cantilevers at 15º intervals in (110) single crystal copper face, optical micrograph. Experimental (points) and literature data (lines) about Young's modulus of copper single crystal, with both techniques proposed in ref. [104].

Wurster *et al.* [105] detailed how the ion slicing technique can be used to prepare different types of micro-sized specimens for bending, compression and tensile tests. In the same work, preliminary fracture toughness experiments were conducted after cutting notches with FIB, showing the potential of this shaping technique.

Chapter 2

Aim and scope of the work

As it has been shown in the introduction, one of the weak points of 3Y-TZP is its poor resistance to LTD which can affect the long-term reliability of biomedical implants. Terefore, one first target of the thesis is to increase the resistance of the material to LTD with no losses in terms of mechanical properties. This should be achieved through the development of simple procedures to be implemented without altering significantly the standard manufacturing process through CAD/CAM technology.

The second main objective of the thesis is to assess near-surface mechanical properties of TZP by employing small-scale testing, evaluating in this way directly the effect of LTD and studying the role of size on mechanical properties. The results should be able to give insights on the surface reliability of the material and to select useful design parameters for the development of novel -and more durable- biomedical implants.

2.1. Methods for improving the surface long-term stability

Ce is a suitable dopant for increasing the long-term stability of 3Y-TZP, due to its compatibility with ZrO_2 structure and better aging behavior. On the other hand, the literature shows that 12Ce-TZP has lower hardness and strength than 3Y-TZP. Therefore, the idea here is to alloy Ce in 3Y-TZP surface regions, without affecting the bulk of the material.

The idea of alloying Ce into Y-TZP surface region is not new, since diverse methods following this principle have already been proposed [56], [57], [106]. In a recent publication, Marro *et al.* [57] describe a method for increasing resistance to LTD based on the diffusion of a pressed cerium oxide layer from surface at high temperature after final sintering. The

method proposed in the present work is also based on the introduction of Cerium oxide in 3Y-TZP, but the procedure is different, based on the infiltration of a Cerium liquid precursor into surface pores or defects. Cerium III Nitrate Hexahydrate, $Ce(NO_3)\cdot 6H_2O$, has been chosen as a precursor of CeO_2, since it is easy to manipulate and dissolves in water or ethanol up to high concentration. After thermal treatment, the salt decomposes into CeO_2, which is partly deposited, so Ce can diffuse into the material from the pores/defects connected to the surface.

Infiltration is a simple technique which can be applied to the processing of zirconia. Once the infiltrating solution has been optimized, it can easily penetrate the material and the residues of the salts can be evacuated during the final sintering, without generating significant wastes. It has been shown in the past that infiltration processing of ceramics can lead to a variation in microstructure and compositions. It is a valid technique for finely dispersed doping, obtaining microscopically homogeneous materials that can be also macroscopically homogeneous or present a gradient in composition [107], [108]. The employment of nitrate salts was previously proposed as a way to introduce Cerium [109] or alumina [110] and obtain the oxide in a simple way during pyrolysis. Also, the idea of performing cyclic infiltration to obtain different composites with higher concentration of the infiltrated phase was suggested for the zirconia/mullite system [111].

Cerium co-doping by infiltration processing is studied in this thesis with two different approaches, which are detailed in the next sections.

2.1.1. Infiltration of Ce in pre-sintered blanks

The first approach involves the infiltration of Cerium Nitrate solutions in pre-sintered porous blanks after soft machining (see section 1.4.2 for details on dry processing). This method applies directly to CAD/CAM processing of TZP pieces. During previous studies, it was already confirmed that dense materials can be obtained after infiltration without the presence of significant defects and that Ce alloying is effective in preventing LTD. Matter of study is how the Ce doping modifies the mechanical properties and if there is an optimum concentration for minimizing these variations still avoiding LTD. In this view, it is necessary to evaluate the role of various parameters in the process: pre-sintering temperature and porosity, salt concentration, infiltration time and temperature, drying conditions and final sintering temperature.

2.1.2. Infiltration of Ce in superficially etched/sandblasted samples

The second proposed approach is to apply infiltration of Cerium precursors in the surface of the fully dense material, once superficial treatments aimed at generating roughness have been performed. The creation of carefully engineered surface roughness on the surface of the implant is mandatory when the implant is designed either for bone adhesion and regeneration (this is the case of dental posts or may be the case of artrhoplastic parts in contact with the bone for all-ceramic systems) or for veneering/bonding with another material (this is the case of veneering of dental crowns and crown/abutment union). Although roughness generation on zirconia surface is not a well established and unified process, the main techniques that are being studied are acid etching and sandblasting. In sandblasting roughness is created mechanically by spraying hard particles on the surface, which erode the material by producing chipping of particles and leaving many microcracks beneath the surface. Annealing is usually performed after sandblasting for stress relieving. In acid etching, individual grains are corroded by the aggressive solution and a certain amount of porosity is created beneath the surface due to preferential etching. In both techniques, the cavities produced by microcracking and porosity can be exploited for infiltration with the precursor followed by annealing, in order to produce a enriched Ce layer which could protect the surface from degradation. The method will be validated by studying the effect of salt concentration and annealing temperature on the degradation resistance and surface integrity. This time, the effect of pressure will also be studied since pressure may be necessary to introduce the dopant in the superficial defects. If successful results will be obtained, this technique could be easily applicable since it does not require severe complications in the manufacturing process.

2.2. Small-scale testing of zirconia surface

Small-scale testing is employed in this thesis with the objective of assessing the near-surface mechanical properties of TZP when the material is modified, degraded or damaged and to evaluate size-dependent phenomena. Therefore, samples smaller than the thickness of the affected surface are machined with the aid of Focused Ion Beam and tested using nanoindentation, which is the appropriate technique for achieving adequate load and displacement resolution.

The small-scale tests are performed before and after degradation. Since the degraded layer is usually few micrometers thick, this is also the size of samples that need to be milled.

During preliminary studies, different specimen geometries were obtained with the use of FIB and the available milling control program. Following these results, the tests which are proposed for investigating the small scale response of the surface are: micropillar compression and micro-cantilever bending.

2.2.1. Micro-pillar compression

Micro-pillars of different sizes are milled with FIB on the zirconia surface, using the annular milling method included in the software of the SEM-FIB dual beam station.

Different specimen sizes are chosen according to the depth of the layer of material of interest. Ex-situ compression experiments are performed with a MTS XP Nanoindenter equipped with a flat-punch tip or a CSM Ultra Nano Hardness Tester - UNHT (CSM Instruments, Peseux, Switzerland). The compression behavior of as-sintered and degraded materials is compared and the change in compressive response associated to degradation was investigated. Moreover, the existence of size effects was studied by comparing the response of zirconia pillars of different sizes. Pillars diameters varied between the smallest that can be milled providing an acceptable shape (few hundreds of nanometers) and the biggest that can be tested in the nanoindentation system (one to few micrometers, depending on the system).

2.2.2. Micro-cantilever bending

Micro-cantilevers are produced in order to assess the flexural response at the small scale. The final shape is obtained by sequential milling of trenches on the edge region of a polished sample. Details about the milling procedure are provided in Chapter 6 (supporting information) and in the Chapter 3.

In this case, a sharp tip is needed so that the contact occurs at one point at the free end of the cantilever. In bending, half of the sample is subjected to a compressive state, while the "outer" region is in tension, where failure is expected. After optimizing the milling operations in terms of currents and dimensions, micro-cantilevers are milled with different orientations with respect to the surface, both in the as-sintered and the artificially degraded samples. In this way, the anisotropy of mechanical properties and damage due to LTD is assessed and the strength of the degraded layer is measured. At the same time, the effect of transformation on stress-strain curves is analyzed. Testing is carried out in-situ inside a scanning electron microscope during a stay in an external research center.

Chapter 3

Experimental details

The experimental details of each part of this thesis are presented in the respective articles. Nonetheless, some additional details are provided in this chapter about sample preparation and testing at the small scale.

3.1. Specimens preparation

In order to evaluate the method proposed here, 3Y-TZP powder is used (Tosoh Corp.) as base material to produce the pre-sintered blanks (specimens). This powder, which is named 3YSB-E, has a measured particle average size of 0.6 μm as measured by liquid phase photosedimentation, due to particle agglomeration. The actual particle size observed in TEM is approx. 40 nm and the crystallite size of 36 nm (calculated from X-ray spectra), while the spray-dried granule average size is 60 μm. Two types of specimens are investigated: macroscopic (disc shape) and microscopic (micro-pillars and micro-cantilevers), where the latter are machined from the surface of the discs with the aid of FIB milling.

3.1.1. Discs preparation

The powder is compacted using cold isostatic pressing method (CIP) at 200 MPa with a dwell time of 10 minutes. The rod compacted bodies are then pre-sintered in air during one hour in a tubular furnace, adopting the selected pre-sintering temperatures, which range from 1100 ºC and 1300ºC. The heating and cooling rate is 3ºC /min. The pre-sintered rods are cut into 2 mm thickness in automatic cutter (Struers Accutom-50) using water as lubricant, obtaining the disc shape. This is what is called “pre-sintered blanks”. Blanks are ground to

obtain flat and parallel surfaces and cleaned several times in distilled water to eliminate powder residues. If infiltration is carried out, the blanks are submerged in a solution of the desired salt (Ce III Nitrate Hexahydrate (REacton, 99,5% (REO) provided by Alfa Aesar), with concentrations ranging from 50 wt% to saturation according to the treatment, in distilled water or ethanol (C_2H_5OH) for the time necessary to infiltrate partially or totally the open porosity, according to the specified procedure. Infiltration may be carried out either at ambient temperature or at boiling temperature. In the latter case, a heater/condenser apparatus based on Soxhlet design is used to maintain the concentration of the solution during infiltration.

During the final conventional sintering process, the water evaporates, the salt decomposes into the oxide after the liberation of crystallization water and N_xO_y species in gaseous form [112] and the diffusion of CeO_2 into 3Y-TZP matrix takes place. The standard treatment is carried at 1450 ºC with a dwell time of two hours and a heating/cooling rate of 3 ºC /min, but other treatments at higher temperature/during longer dwell times are employed. After sintering, discs are grinded and polished using a conventional ceramic method to obtain mirror-like surfaces. Final disc specimens have a diameter of approx. 9 mm. For control samples, normally identified as "as-sintered" (AS), infiltration does not take place.

In the case of Infiltration of Ce in superficially etched/sandblasted samples, discs already treated superficially are submerged in a saturated solution of Ce precursor both at ambient pressure and at high pressure. The high pressure is provided by the CIP machine, after introducing the infiltrating solution and the sample in a deformable bag which is sealed and placed inside the pressure chamber. After infiltration, the surface is wiped with laboratory drying paper and samples are annealed for obtaining Ce diffusion. Annealing conditions are matter of study.

Before sintering, a separate drying process may be necessary with the purpose of avoiding nonuniformities in salt distribution. Temperatures and times are optimized according to the infiltration method.

3.1.2. Small-scale samples preparation

Inside the dual-beam microscope, the configuration used for machining micro-pillars is usually the one described in Figure 3.1, where SEM and FIB columns are placed at 54º with respect to each other. The initial disc-shaped samples are cut along the diameter and the cross-section is ground and polished using a tripod fixture (Struers A/S) to obtain a sharp cross-

sectional edge polished on both sides. Polished samples are mounted on inclinable electron microscopy supports and coated with a very thin (approx. 10 nm) carbon layer to make them conductive. In this work, milling is done inside a Zeiss Neon 40 station equipped with a Gemini SEM column and a FIB column and a GIS (Gas Injection System) from Orsay Physics. Small-scale samples are milled on the top surface of the disc, near the polished cross-section, to allow easy visualization and manipulation during and after testing. Before milling, the region of interest is placed in the coincidence point between the beams, so that the features milled with FIB can be visualized right after with SEM. The disc surface is first imaged with the ion beam to find the tangent angle and set the reference for the following operations.

For micro-pillars, milling is performed in at least two steps and the milling procedure has to be optimized according to the desired size of the pillar. In order to allow after-test visualization and easy location during testing, in the first step a large (30 µm diameter) vessel is milled using the annular milling feature of the Zeiss SmartSEM software. The dwell time, and so the milling depth, is increased progressively during the process, leaving a cylinder of intact material in the center (see Figure 3.1). In the second step, lower and more focused FIB currents are employed in order to achieve a specific milling depth, reducing as much as possible the taper angle and maintaining sharp edges at the top of the pillar. In the case of sub-micrometric pillars, a final cut of the top pillar surface is performed to eliminate the edge blunting.

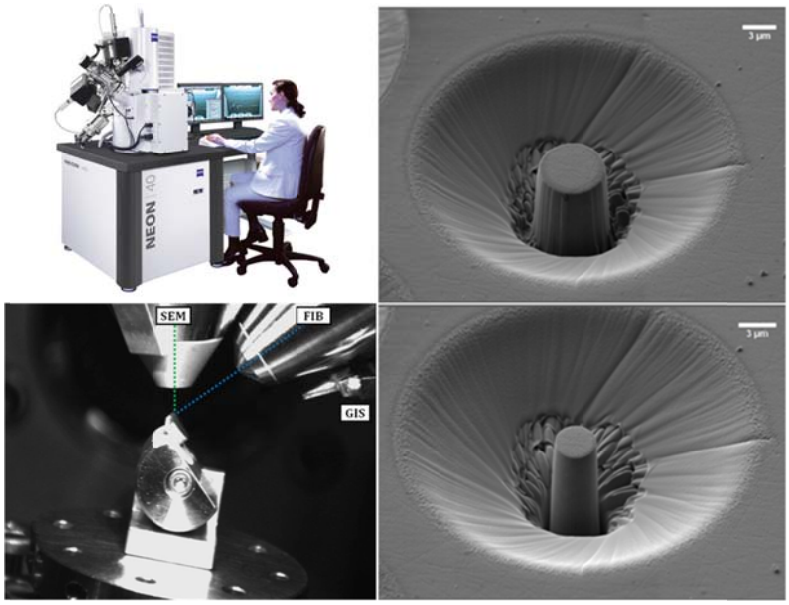

Figure 3.1. Left: dual beam Zeiss Neon 40 (top) and image of the chamber, where SEM and FIB columns are visible. The specimen (half of a disc, polished both on top and cross-section) is mounted on a special holder and tilted 54º. Right: two-steps milling of a pillar (scale bar = 3 µm).

In the case of micro-cantilevers, the final shape is obtained by sequential milling of trenches on the edge region of the disc sample. Pt deposition is performed at the beginning of the procedure to avoid FIB damage of the surface of the cantilevers which is exposed to tension. Similarly to the previous case, high currents are used in the first steps of the procedure and low focused currents are used at the end. Milling needs to be performed from both the top and the cross-sectional surfaces in order to shape the four sides of the cantilevers. Pt layer is removed at the end with low FIB currents. Two examples of cantilevers with different configurations are shown in the figure below. A detailed description of the milling procedure with diagrams is shown in section 6.1.

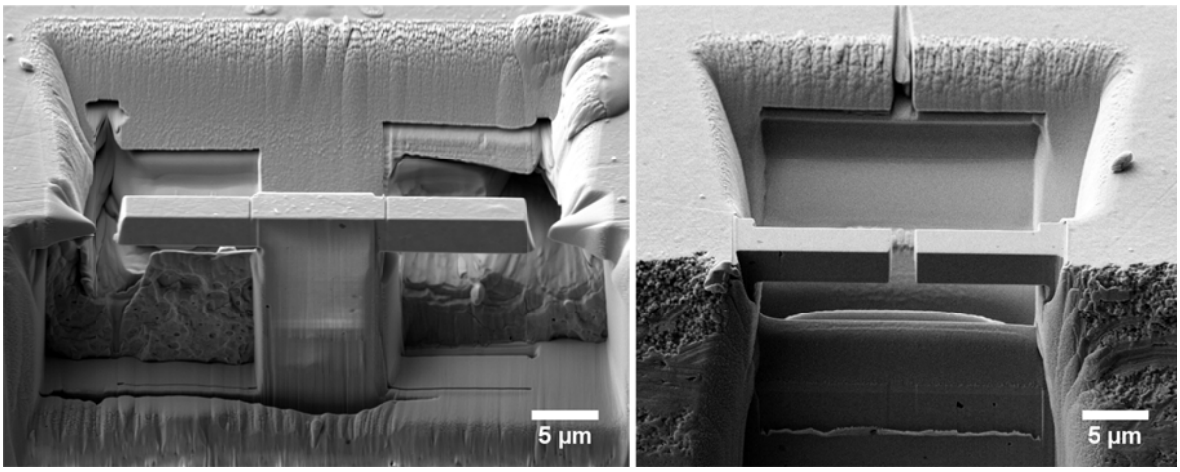

Figure 3.2. Final shape of cantilevers milled from the zirconia surface region with two different procedures.

3.2. Micro-compression tests

Micro-compression tests are performed according to the scheme of Figure 3.3-a for an ex-situ nanoindenter. When it comes to compression testing, some concerns can arise regarding different aspects of testing configuration, procedure and data interpretation. First of all, there is an important difference with standard compression tests, where both sides of the sample are free to slide against compression plates. Here, the base of the pillars is rigidly constrained, resulting in a triaxial stress state in this region. Another important aspect is represented by the possibility of either reciprocal sliding or conjoined lateral movement of the indenter flat surface and the pillar top face, being the second option the most likely to occur [72].

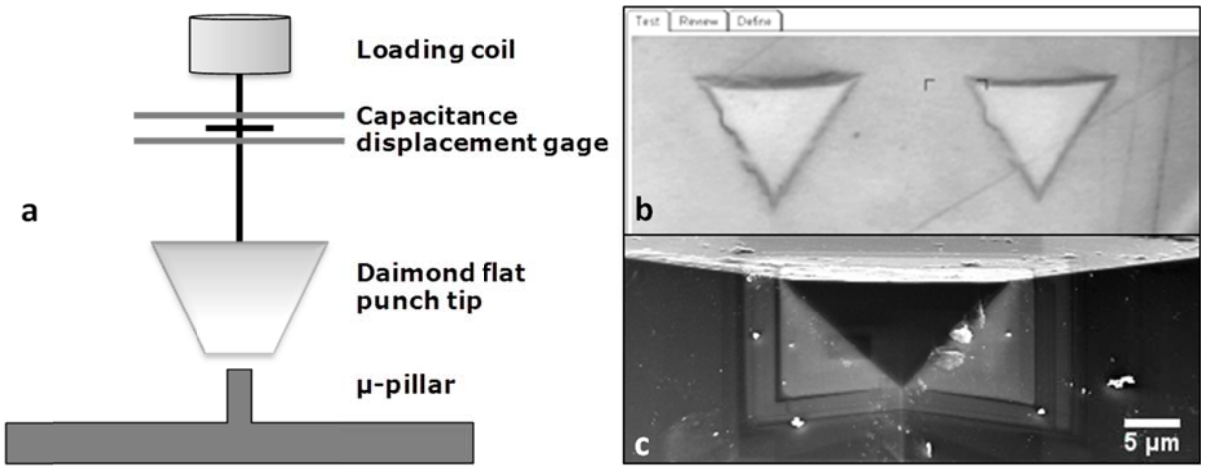

Figure 3.3. a) Micro-compression scheme for a MTS Nanointenter XP. b) Flat-punch marks during microscope-to-indenter calibration on aluminum single crystal. c) SEM image of the home made flat punch tip obtained by FIB assisted cutting of a Berkovich diamond tip.

Displacement has to be transmitted to the sample in a very accurate and rigid way, especially when testing is addressed to very small geometries and to dislocation movement detection [113]. Handling of the samples must be also very accurate during the transfer from the dual-beam station to the nanoindenter, so that the sample is not contaminated and the orientation of the pillar is maintained. For this purpose, a nanoindenter holder suited for electron microscopy stubs was machined, so that the same support used during FIB milling could be placed directly inside the nanoindenter chamber, with no need for touching or ungluing the sample.

A nanoindenter MTS XP equipped with a CSM module is employed in most of the tests, with a homemade flat-punch diamond tip machined via FIB from a Berkovich indenter (see Figure 3.3-b). The side of the equilateral triangle constituting the flat surface is of 18 µm, as can be seen in Figure 3.3-b and –c. When testing with the Ultra Nano Hardness Tester, a flat-punch tip with hexagonal shape is employed.

Fine microscope-to-indenter calibrations are necessary when using the optical microscope coupled with the nanoindenter. To perform this operation, a surface that is susceptible of easy plastic deformation is necessary, because the print has to be easily recognizable with the microscope. Due to the fact that hard ceramics do not show any residual mark after flat-punch indentation at small loads, an aluminum substrate, placed apart from the zirconia specimen, is used to perform a first calibration. A second calibration can be done on a thin layer of cyanoacrylate deposited close to the micro-pillars, on the same zirconia substrate. Since there is always certain grade of mechanical shift between the microscope and the indenter tip, which is around 1-2 µm (this value depends on the system and its state),

several calibrations have to be performed during the experiments. The residual marks are also useful to clean the tip from debris of previous tests and to check, and eventually correct, the alignment between the flat indenter tip and the sample surface, since significant misalignments result in non symmetric residual marks.

The force and displacement resolutions provided by a common nanoindenter are well suited for micro compression testing, having enough sensitivity in order to obtain detailed load-displacement curves in the small range studied [72]. Moreover, a nanoindenter is also capable of data correction for thermal drift, which can be important at these scales.

Once calibration has been performed, the compression test can be run, generally by giving a prescribed loading or displacement rate. In nanoindenters using loading coils, which are inherently load-controlled [81], [114], the fixed loading rate has been found more reliable to obtain reproducible tests. This value should be calculated according to pillar size if the behavior of different sizes is to be compared, since similar strain rates have to be provided during testing.

3.3. Micro-cantilever bending

When ex-situ testing is performed, micro-cantilever bending tests use the same equipment as for the micro-compression tests (Nanoindenter XP), but a sharp tip is now mounted. With a sharp tip, the Nanovision module available in the nanoindenter can be used for scanning the surface beside the cantilever, in contact mode with a load of few μN, to obtain a topographic image of the region. With this mode, the position of the tip is controlled by piezoelectric actuators and the precision is much higher, allowing performing the test in the exact point of choice. In this case, the effect of tip penetration into the material, which can be important for very soft or high strength materials, may be subtracted from the displacement in load-displacement curves. In the case in-situ bending tests, a Hysytron PI 80 Picoindenter is employed, which is mounted horizontally inside the SEM chamber, i.e. with the loading axis perpendicular to the electron beam. Surface scanning prior to testing is not necessary in this case since the contact takes place under SEM imaging. A tilt of 1º – 3º is needed for visualizing part of the edge of the samples and correctly positioning the indenter tip at the test location.

Chapter 4

Articles presentation

Article I. Revealing crack profiles in polycrystalline tetragonal zirconia by ageing

Manuscript published; *Journal of the European Ceramic Society* **32,** 1541–1549 (2012). doi: 10.1016/j.jeurceramsoc.2012.01.013

Author's contribution: finding of the aging effect on indentation crack profiles, production, testing and analysis of Cerium co-doped samples.

In this paper, the effect of water vapor exposure is shown to be useful for revealing indentation crack profiles in doped zirconia polycrystals. In fine-grained ceramics development, the fracture toughness and resistance to crack growth are key parameters. To measure fracture toughness, one of the approaches includes the generation of a crack by a sharp indentation, followed by testing in flexure and measurement of the initial crack. Another method is based on the simple surface measurement of the cracks developed after a Vickers indentation, which is limited by the fact that the real shape of the cracks is generally unknown. The models usually applied for the residual stress intensity factor very often do not provide the actual fracture toughness of the material, only comparative trends. Even after breaking the sample, the crack profile is in many cases difficult to recognize.

The materials studied in the article are 3Y-TZP with two different grain sizes, and 3Y-TZP with 2.5 wt.% Cerium oxide added by infiltration of pre-sintered porous performs. They are Vickers indented and artificially aged under sterilization conditions. These materials are selected because both the shape of the indentation cracks and the degradation resistance is different in each material because of different transformability associated to grain size and to presence of additional stabilizer. The crack profile is clearly revealed on the fracture surface after biaxial flexural testing in all the specimens exposed to artificial degradation. Since 3Y-TZP suffers from aging, the contrast is created in these materials by t–m transformation, which induces an intergranular microcracked zone in front of the crack tip. The biaxial strength and apparent fracture toughness of 3Y-TZP increase substantially with aging time at a rate that depends on the grain size. Instead, Ce-doped 3Y-TZP is not affected by aging exposure and the flexure biaxial strength remains practically constant, but an intergranular fracture zone associated to environmental crack growth develops in front of the initial crack tip.

Article II. Small-scale mechanical behavior of zirconia

Manuscript published; *Acta Materialia* **80,** 239–249 (2014). doi: 10.1016/j.actamat.2014.07.053

Author's contribution: design and development of the idea, realization of a protocol for milling the desired micro-cantilever samples, set up of the collaboration with INM-Saarbrücken for the in situ testing, realization of the testing experiments together with the second author, analysis of the results and article writing.

This work is the first in literature applying novel small-scale testing techniques to 3Y-TZP. The present results offer for the first time a direct measurement of the flexural response of the surface degraded layer by employing the *in situ* micro-cantilever bending technique. Micro-cantilevers are milled inside the zirconia degraded layer by using focused ion beam and tested inside a SEM microscope. Load-displacement data are converted into stress-strain curves, obtaining quantitative results. Moreover, by testing samples orientated in different directions with respect to the degraded surface, it is proved that the damage induced is strongly anisotropic. Interesting insights on the non-degraded zirconia mechanical response at the small scale are presented: significant quasi-plastic behavior due to phase transformation and yield-limited bending strength, which reaches values above 4500 MPa. These properties are surprising for polycrystalline zirconia ceramics that are traditionally "brittle" in the bulk state and where bending strength is normally about 1000 MPa.

Article III. Enhanced reliability of yttria-stabilized zirconia for dental applications

Manuscript published: *Acta Biomaterialia* **17**, 36–46 (2015). doi:10.1016/j.actbio.2015.01.023

Author's contribution: design, planning, implementation and realization of all the experiments, some of which together with co-authors. Analysis of the results and article writing.

This work represents a clear advance in processing of biomedical grade zirconia, which is one of the most important biomaterials used in the dental field. The method which has been proposed and optimized is capable for improving substantially the zirconia surface stability against low-temperature degradation, with minimal modifications in the processing steps of CAD/CAM dentistry. This result is achieved through the infiltration of solutions containing Cerium salts in zirconia machined pre-sintered parts. The paper offers a complete characterization and optimization work, where several parameters are studied to control the surface CeO_2 content and its gradient through the bulk. Moreover, the effect of changing the sintering temperature is investigated with the objective of modifying the *t-m* transformability of the obtained materials. Finally, a material with a good combination of high resistance to environmental aging and similar mechanical properties to the reference yttria-stabilized zirconia is obtained, allowing the design of more reliable dental parts. Since the number of applications in the dental field employing this material is increasing more and more in the last years and thanks to the completeness of the study and ease of implementation of the proposed method, the obtained results are of high scientific and technological impact.

Article IV. Surface roughened zirconia: towards hydrothermal stability

Manuscript published: *Journal of the Mechanical Behavior of Biomedical Materials* **47**, 95-106 (2015). doi: http://dx.doi.org/10.1016/j.jmbbm.2015.03.017

Author's contribution: planning and design of the study, sample preparation, realization of most of the tests and characterizations. Analysis of results and article writing. Acid etched samples have been prepared together with one co-author, similarly to the realization of the roughness measurements and some of the FIB characterizations.

This work is thought for zirconia dental restorations parts where surface roughness is needed for adhesion or osseointegration purposes, which can be in contact with body fluids and therefore are susceptible to hydrothermal degradation. The latter may impair the long-term surface stability, which can lead to adhesion issues and the release of particles into the body. The simple method that is proposed is capable of improving substantially the zirconia surface stability with minimal modifications in the microstructure. This is achieved through pressure infiltration of sintered zirconia surfaces, which have either been sandblasted or acid-etched for creating surface roughness, with solutions containing Cerium salts. The infiltration is followed by a diffusion treatment, which creates a thin co-doped protective layer that does not alter the color of the material. The paper offers an advanced characterization work, showing clearly the benefits of the proposed treatment against hydrothermal aging and analyzing the induced surface modifications.

Article V: Micropillar compression inside zirconia degraded layer

Article accepted and published online: *Journal of the European Ceramic Society* (2015). doi 10.1016/j.jeurceramsoc.2015.04.017.

Author's contribution: design of the experiments, sample preparation, adaptation of nanoindentation instruments for testing, set up of a collaboration for using the high-resolution nanoindenter, testing, characterization, analysis of results, article writing.

The surface stability of this material is critical due to the so-called hydrothermal degradation, which produces a thin degraded layer in contact with body fluids. The present results offer for the first time a direct measurement of the strength of the surface degraded layer by employing the micropillar compression technique, showing that the compressive strength and strain are strongly affected by the aging process. Moreover, the variation of the response with micropillar size is studied and cyclic loading/unloading tests at increasing peak loads are performed, showing interesting insights on the mechanical response at the small scale in relation to the presence and distribution of degradation-induced microcracks. Their effect on the micromechanics of zirconia is shown to be crucial in terms of strength, stiffness and deformation behavior.

Article VI (Annex A). Role of size and plasticity in zirconia micropillars compression

Article submitted to *Acta Materialia*, under review (2015, submission ref. A-15-657).

Author's contribution: work planning, design of the experiments, sample preparation, adaptation of nanoindentation instruments for testing, set up of a collaboration for using high-resolution and in-situ equipment, testing, FIB and TEM characterizations, analysis of results, article writing.

This paper represents a kick-off work about micropillar compression and size effects in polycrystalline zirconia, providing novel insights on the unique behavior of this material under very high applied stresses at the small scale. The absence of natural defects in micropillars obtained by Focused Ion Beam allows reaching compressive stresses up to 9 GPa, compared to ~4 GPa of macroscopic samples. Significant plasticity is observed at these stresses, associated mostly with phase transformation, so that this ceramic material shows ductile character at the small scale with failure strains of 5% – 8%. Different pillar sizes are tested to investigate size-dependent phenomena. The "yield stress" is lower for sub-micrometric pillars with diameter similar to the grain size, where the deformation proceeds through strain bursts, representing an evident size effect. The paper offers an advanced characterization work by means of monotonic and cyclic tests, together with STEM, TEM and FIB observations, giving a complete survey on the mechanical properties and failure mechanisms at the small scale. Moreover, time-dependent and hysteresis phenomena are observed, opening the path to future research.

Article VII (Annex B). Development of a novel zirconia dental post resistant to hydrothermal degradation

Article published: *IOP Conference Series: Materials Science and Engineering* 31, (2012). doi:10.1088/1757-899X/31/1/012016

Author's contribution: planning of the study and experiments together with co-authors, sample preparation, realization of the tests and analysis of results with co-authors, article writing.

This work explores the addition of ceria from the surface of 3Y-TZP as a way to improve the aging behavior of dental posts. This was achieved through the infiltration of the pre-sintered porous samples with a solution containing Cerium salts, followed by sintering. After sintering, Cerium co-doping is obtained with a gradient from the surface to the bulk. Dental post prototypes are obtained in a rod shape and the modifications introduced with the treatment are studied in terms of microstructure, flexural strength in the as-sintered state and aging resistance. The novel zirconia dental posts prototypes developed in this work are much more resistant to LTD as compared to the base material with no loss in flexural strength, showing promising results for the future optimization of the infiltration technique.

Chapter 5

Article I: Revealing crack profiles in polycrystalline tetragonal zirconia by ageing

The article is available for download at the following web address:

http://dx.doi.org/10.1016/j.jeurceramsoc.2012.01.013

Chapter 6

Article II: Small-scale mechanical behavior of zirconia

The article is available for download at the following web address:

http://dx.doi.org/10.1016/j.actamat.2014.07.053

6.1. Supporting information for "Small-scale mechanical behavior of zirconia"

6.1.1. Details of milling procedure for oriented cantilevers

Before starting fabrication, a platinum layer (approximately 100 nm thick) was deposited on the target milling region to protect the final surface from FIB damage. Then, a first trench (T1) of relatively big size was milled on the top side to obtain a 90° edge between the top side and the cross-section, see Figure 6.1. This was done with relatively high gallium ion beam current and step size (thickness of every milling step).

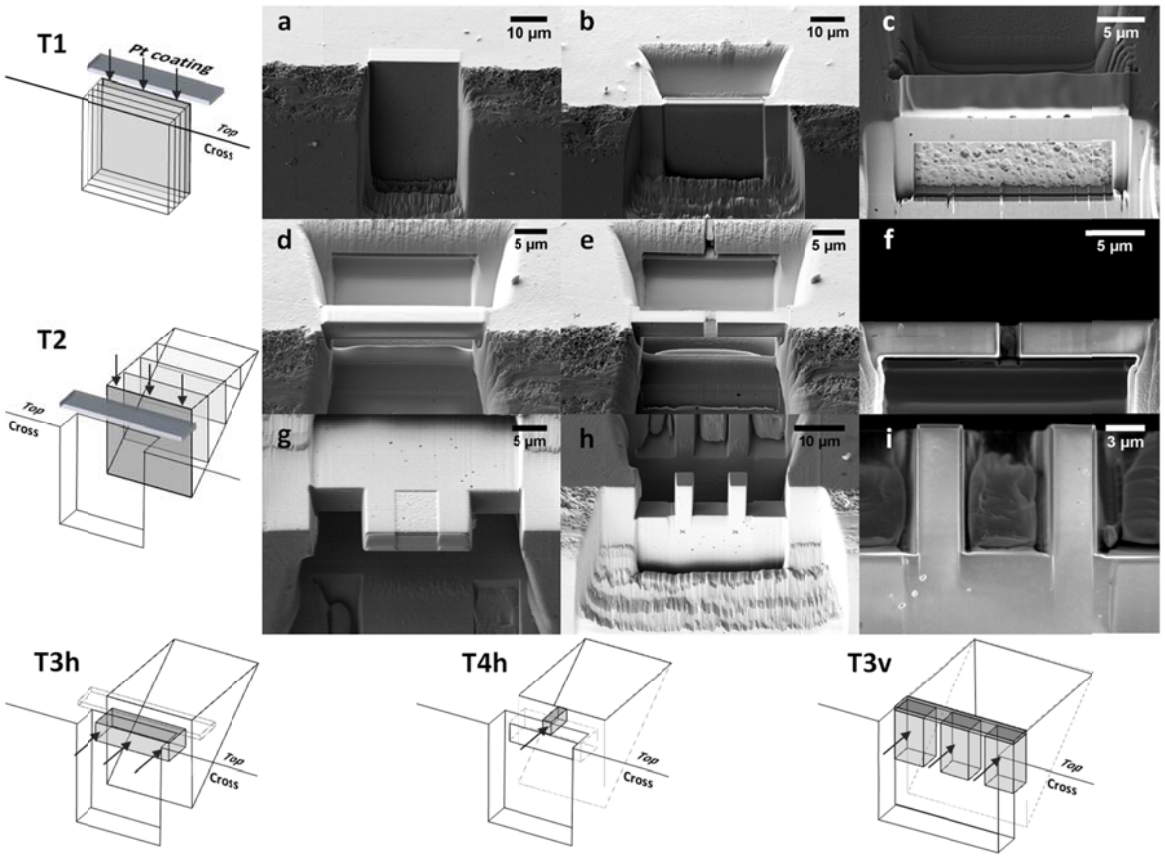

Figure 6.1. Detailed milling procedure for horizontal and vertical cantilevers. The different trenches and cuts are shown. (a): T1; (b): T2; (c) and (d): T3h; (e) and (f): T4h (final shape for horizontal cantilevers); (g), (h) and (i):, T3v (final shape for vertical cantilevers).

The top surface was chosen as reference for adjusting the orientation during the different milling operations. A region slightly bigger than the final cantilevers was then polished on this surface using lower gallium ion beam current and step size. Secondly, a trench with similar depth (T2) was milled symmetrically with respect to T1, where the plane of symmetry was represented by the wall of material which was left untouched. This trench

was polished with lower intensity currents on the side close to the final cantilevers in a similar fashion as T1. The sample was then turned in order to visualize T2, which was formerly hidden to the SEM beam. After this first steps, the procedure was different for milling horizontal and vertical cantilevers. For the first, a rectangular trench was milled and then polished (T3h), this time on the cross-section, in order to hollow out the material under the cantilevers. The superficial Pt layer was then polished away with very low currents and the two symmetric beams were separated with a final cut of approximately 2 μm (T4h). For the second, an "M" shape (T3v) was milled at once around the two cantilevers, removing at the same time the Pt layer, and the sides were finally polished.

6.1.2. In-situ bending test movie

A short movie was recorded inside the SEM-FIB VERSA 3D dual beam station and it is available at the address "http://dx.doi.org/10.1016/j.actamat.2014.07.053". The movie, which was accelerated 8 times with respect to actual testing speed, shows how the bending test is performed on a non-degraded 3Y-TZP cantilever. The cantilever is loaded from the bottom of the image by the cube-corner tip. Specimen is tilted approx. 3 deg in order to visualize the contact point, so the top surface is partially visible. Cantilever deflection at failure is surprisingly high for a "brittle" ceramic.

Chapter 7

Article III: Enhanced reliability of yttria-stabilized zirconia for dental applications

The article is available for download at the following web address:

http://dx.doi.org/10.1016/j.actbio.2015.01.023

7.1. Supporting information for "Enhanced reliability of yttria-stabilized zirconia for dental applications"

The properties of all the samples sintered at 1450 ºC are summarized in Table 7.1.

Table 7.1. Summary of properties of all materials sintered at 1450 ºC: biaxial strength, CeO_2 content near the surface, IF toughness in the surface region, grain size and monoclinic content after 30 h of artificial aging (mean values ± SD). Letters indicate the statistically significant differences.

Condition	σ^*_{B3B} (MPa)	CeO_2 (%)	K_{IC} (MPa√m)	Grain Size (μm)	V_m (%)
AS	1650 ± 111 a	-	4,9 ± 0,1 a	0,31 ± 0,04 a	52 ± 16
1100L	1517 ± 233 a, b	4,6 ± 0,4	4,3 ± 0,1 b	0,40 ± 0,04 b, c	3 ± 2
1100H	1244 ± 242 b	7,8 ± 0,3	3,7 ± 0,1 c	0,46 ± 0,04 c	1 ± 2
1150L	1508 ± 170 a, b	3,0 ± 0,1	4,3 ± 0,1 b, d	0,39 ± 0,05 b, c, d	2 ± 2
1150H	1325 ± 153 a, b	5,9 ± 0,2	4,1 ± 0,1 e	0,37 ± 0,04 a, c, d	1 ± 1
1200L	1557 ± 174 a, b	1,9 ± 0,4	4,5 ± 0,1 d	0,32 ± 0,04 a	16 ± 6
1200H	1643 ± 275 a	3,8 ± 0,5	4,5 ± 0,1 d	0,37 ± 0,07 a, c, d	4 ± 2
1300L	1581 ± 141 a	0,0 ± 0,0	4,8 ± 0,1 a	0,33 ± 0,04 a, d	47 ± 13
1300H	1630 ± 180 a	0,1 ± 0,0	4,9 ± 0,1 a	0,32 ± 0,04 a	49 ± 10

The microstructure observed for the different pre-sintering conditions is presented in Figure 7.1.

Examples of XRD patterns obtained from all the samples infiltrated with 50 wt.% solutions after exposure to artificial degradation are presented in Figure 7.2. For comparison, the XRD pattern of the control material (AS) is shown in the same figure before and after aging. The AS non-aged sample has the same pattern as the 1150*L* and 1100*L* ones, meanwhile the aged AS sample shows a very similar pattern as the aged 1300*L* one. XRD patterns of the materials at the pre-sintered state look identical to the AS non-aged one and are not reported.

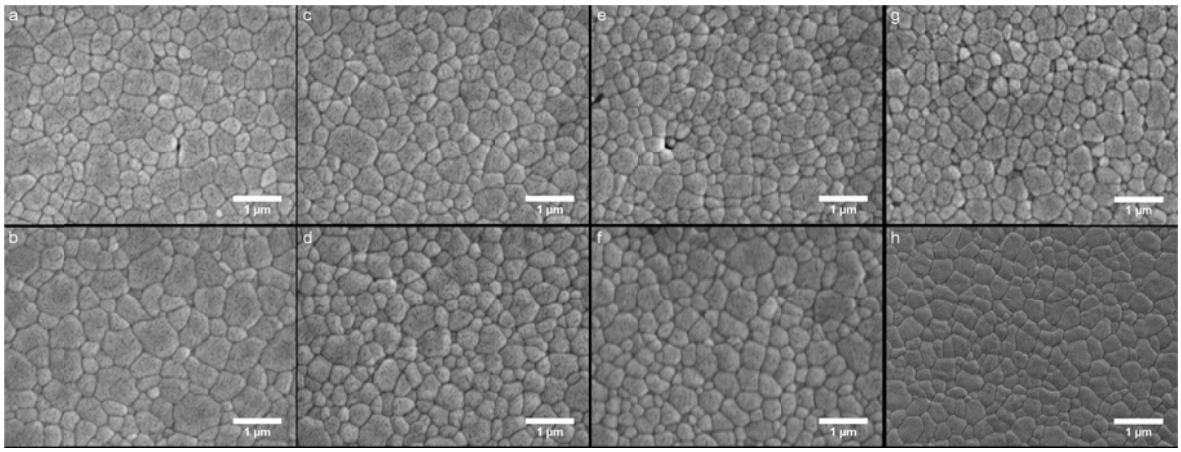

Figure 7.1. Microstructure of materials with different pre-sintering conditions. a: 1100*L*, b: 1100*H*, c: 1150*L*, d: 1150*H*, e: 1200*L* f: 1200*H*, g: 1300*H*, h: AS. Scale bar = 1 µm.

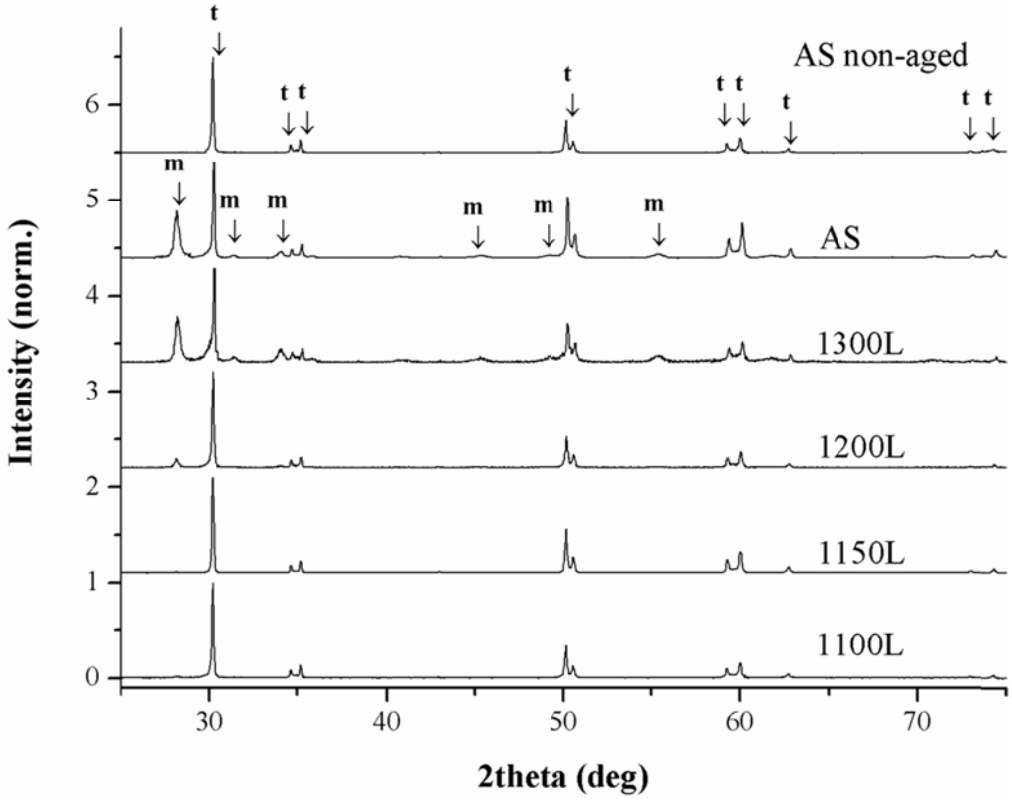

Figure 7.2 (Figure S2 in the article). XRD normalized spectra after artificial aging, in the region 25-75 deg., for selected conditions: AS, 1300L, 1200L, 1150L, 1100L. Additionally, one extra spectra is included for the AS non-aged material (i.e. the base material).

The microstructure of S1450, S1550 and S1600 samples is presented in Figure S3 and compared with the reference AS condition.

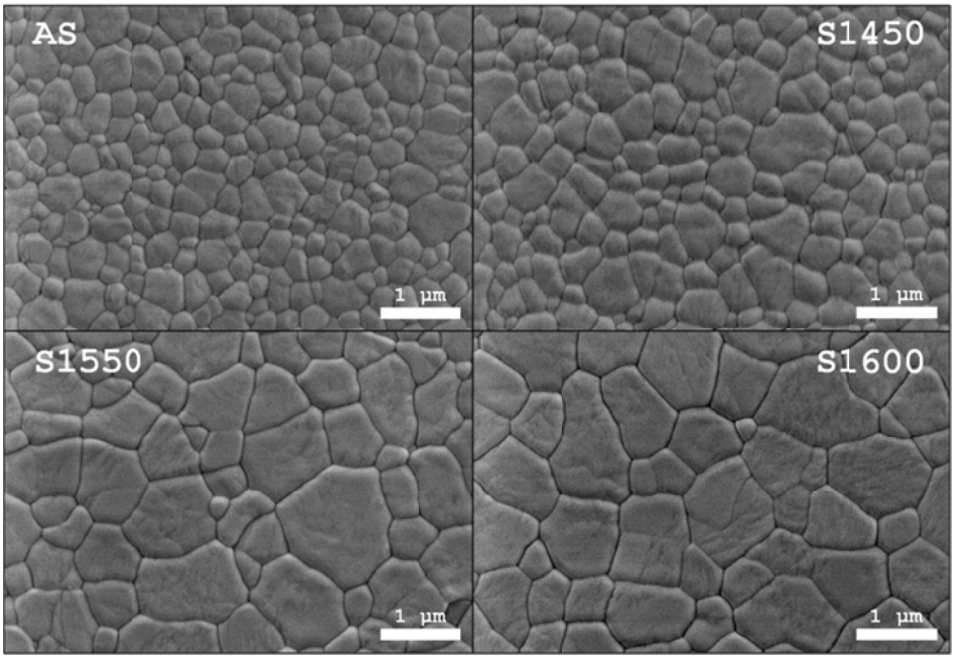

Figure 7.3. SEM micrographs of the AS (a), S1450 (b), S1550 (c) and, S1600 (d) microstructures. Scale bar = 1 µm. Samples have been infiltrated at pre-sintered condition 1150º.

XRD spectra obtained after artificial aging from the samples sintered ad different temperatures are shown in Figure S3, where the presence of the (-1 1 1) and (1 1 1) monoclinic peaks gives a clear indication of the progress of the aging process.

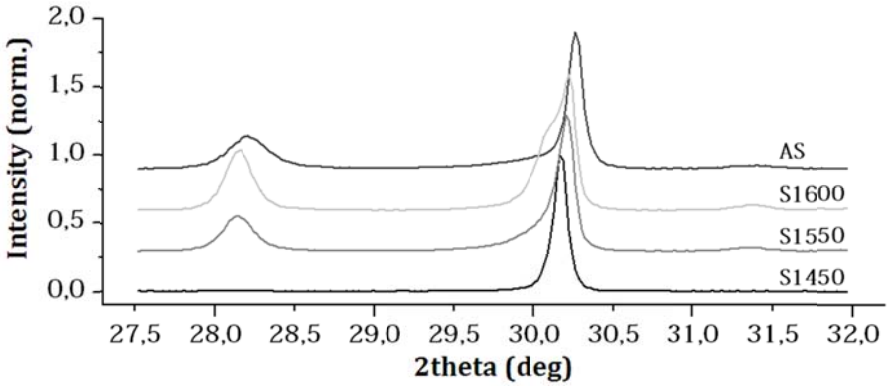

Figure 7.4. XRD normalized spectra after artificial aging, in the region 27.5-32 deg.

Chapter 8

Article IV: Surface roughened zirconia: towards hydrothermal stability

The article is available for download at the following web address:

http://dx.doi.org/10.1016/j.jmbbm.2015.03.017

8.1. Supporting Information for "Surface roughened zirconia: towards hydrothermal stability"

The FIB trench of Figure 8.1. shows the profile and sub-surface appearance of an etched material where the infiltration had been performed at ambient pressure, followed by diffusion treatment. The specimen had been exposed to artificial aging in a similar fashion as for the other samples. In this case, few isolated spots showing evidence of hydrothermal aging were detected, as the one highlighted on the picture.

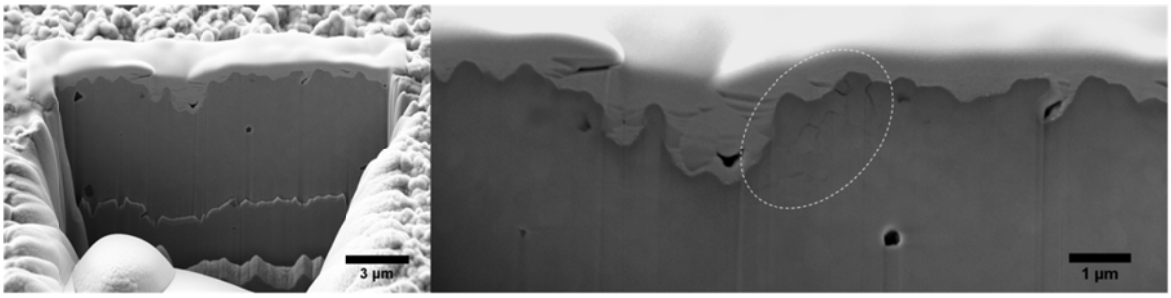

Figure 8.1. FIB trench on EIT material infiltrated at ambient pressure. To the right, a degraded spot is highlighted.

Chapter 9

Article V: Micropillar compression inside zirconia degraded layer

The article is available for download at the following web address:

http://dx.doi.org/10.1016/j.jeurceramsoc.2015.04.017

Chapter 10

Results and conclusions

10.1. Summary of the results and discussion

This thesis has been developed around two main topics: infiltration processing of 3Y-TZP for improving the long-term surface stability in human body environment and small-scale testing of zirconia. In this chapter, the main findings of the research work are outlined.

10.1.1. Infiltration of Cerium nitrate solutions in pre-sintered zirconia: preliminary studies

Infiltration processing has been confirmed as a suitable method for creating functionally-graded Cerium co-doping in yttria-stabilized zirconia. In the explorative work of **Article VII**, it was showed that a pre-sintering condition of 1100 ºC corresponds to open porosity values of ~47 %. By infiltrating with a solution containing Ce nitrate Hexahydrate, ~4 mol% of CeO_2 were obtained on near-surface regions. Dental post co-doped prototypes showed a slight coarser microstructure on the polished surface. Minimal presence of monoclinic phase after 30h of artificial degradation in autoclave at 134 ºC, 2 bar steam pressure were found on samples infiltrated at the 1100 ºC pre-sintered condition. This aging treatment was chosen to be roughly comparable with the maximum implant life expectancy. At the same time, the flexure strength of control 3Y-TZP (AS in the nomenclature) and Ce co-doped dental post prototypes in the shape of bars was similar. Therefore, it was proved that the microstructural changes introduced with the co-doping were not affecting the overall strength of as-fired materials.

10.1.2. Optimization of infiltration processing: CeO_2 profiles and microstructure

In **Article II**, the infiltration concept was developed and several infiltration conditions were studied by varying the pre-sintered temperature, the solution concentration and temperature. The most important results are summarized in Table 10.1. The open porosity decreased progressively from 47% to ~5% by increasing the pre-sintering temperature from 1100 ºC to 1300 ºC. The cross-sectional CeO_2 profiles of disk-shaped samples were obtained, showing that the surface concentration could be varied between 0 and ~7.8 mol% with the selected options and that a graded composition was obtained, with lower concentrations in the bulk of the material. The solution temperature during infiltration had no significant influence, demonstrating that these samples are fully infiltrated by the solution. By increasing the concentration from 50 wt% to 75 wt%, significantly higher amounts of CeO_2 were obtained after firing. It was therefore confirmed that the superficial CeO_2 content could be controlled by changing the sintering parameters and solution concentration.

Table 10.1. Summary of properties of all materials sintered at 1450 ºC: solution concentration, apparent porosity, CeO_2 content near the surface, biaxial strength, IF toughness in the surface region, grain size and monoclinic content after 30 h of artificial aging (mean values ± SD). Letters indicate the statistically significant differences (ANOVA with Tuckey test, $p = 0.05$). Adapted from the supporting information of Article III.

Sample Code	Conc. (wt%)	A. Poros. (%)	CeO_2 (%)	σ^*_{B3B} (MPa)	K_{IC} (MPa√m)	G. Size (μm)	V_m (%)
AS	-		-	1650±111 a	4.9±0.1 a	0.31±0.04 a	52±16
1100L	50%	47.3±0.3	4.6±0.4	1517±233 a, b	4.3±0.1 b	0.40±0.04 b, c	3±2
1100H	75%	47.3±0.3	7.8±0.3	1244±242 b	3.7±0.1 c	0.46±0.04 c	1±2
1150L	50%	42.7±0.9	3.0±0.1	1508±170 a, b	4.3±0.1 b, d	0.39±0.05 b, c, d	2±2
1150H	75%	42.7±0.9	5.9±0.2	1325±153 a, b	4.1±0.1 e	0.37±0.04 a, c, d	1±1
1200L	50%	34.8±0.9	1.9±0.4	1557±174 a, b	4.5±0.1 d	0.32±0.04 a	16±6
1200H	75%	34.8±0.9	3.8±0.5	1643±275 a	4.5±0.1 d	0.37±0.07 a, c, d	4±2
1300L	50%	4.7±1.0	0.0±00	1581±141 a	4.8±0.1 a	0.33±0.04 a, d	47±13
1300H	75%	4.7±1.0	0.1±0.0	1630±180 a	4.9±0.1 a	0.32±0.04 a	49±10

With the proposed method, differences in the concentration (< 1 mol%) were registered at the same depth from the surface for samples processed under the same conditions. The drying procedure was identified as critical for reducing the scatter in the

results. The microstructure is slightly affected by the co-doping: the grain size increases from 0.31 ± 0.04 μm (control 3Y-TZP) to 0.46 ± 0.04 μm for the samples with 7.8 ± 0.3 mol% of CeO_2 in the superficial region. This is imputable to the fact that, with the co-doping, the tetragonal phase is enriched in Cerium and depleted in Yttrium, which tends to segregate forming increasing quantities of highly-doped cubic phase. In this way, the solute-drag mechanism active in Y-TZP for limiting the grain growth is hindered in the tetragonal phase, while the cubic phase has generally higher growth kinetics.

10.1.3. Prevention of hydrothermal degradation in Ce co-doped surfaces

In **Article II** it is outlined that the threshold CeO_2 superficial concentration for preventing completely hydrothermal degradation after the exposure to 30 h of accelerated aging is of approximately 3 mol%. To ensure this content, zirconia has to be infiltrated either after pre-sintering at 1100 ºC or 1150 ºC with either 50 wt% and 75 wt% concentrations, or at the 1200 ºC condition with 75 wt% concentration. Higher pre-sintering temperatures do not allow introducing a sufficient quantity of CeO_2 for hydrothermal aging protection.

10.1.4. Mechanical properties of infiltrated materials

The overall mechanical properties are only slightly modified by the infiltration co-doping. Hardness of polished materials is not affected, while significant decrease in IF toughness, up to 1 MPa√m was observed for the specimens with high CeO_2 contents. The length of the cracks induced by indentation increased approximately linearly with the superficial CeO_2 molar content. This aspect is related to the over-stabilization of the tetragonal phase due to the co-doping and the possible increase in the amount of non-metastable cubic phase, which cannot contribute to the transformation toughening. In these less transformable conditions, a reduction of up to ~25% in the biaxial strength of polished samples was also appreciated. Therefore, in order to maintain approximately the mechanical properties of the control (AS) 3Y-TZP, the CeO_2 content should be limited to 1-3 mol%. The better combination guaranteeing hydrothermal stability is therefore the 1150 ºC pre-sintering condition and 50 wt% solutions, referred to as '1150*L*' in **Article III** and in Table 10.1.

10.1.5. Indentation cracks profiles

Article I illustrates the effect of hydrothermal exposure to indentation cracks in zirconia materials. The hydrothermal exposure is proposed as a method for revealing crack profiles in indented zirconia, since an intergranular crack region is developed during hydrothermal exposure ahead of the initial indentation crack. This microcracked intergranular region has a distinctive contrast after flexure testing of the sample, allowing recognizing clearly the indentation crack depth and shape with both optical and electronic microscopes. While in the 3Y-TZP the development of the intergranular region is associated to the damage induced by low-temperature degradation, in materials co-doped with CeO_2 this is the result of environmental crack growth in humid environment. This is proved by two evidences: a) that the surface of the same material does not suffer from LTD and b) the biaxial strength of indented samples is not modified by hydrothermal exposure, while this is the case in 3Y-TZP materials, where crack-tip shielding and blunting occurs after aging, increasing the strength.

10.1.6. Effect of sintering temperature on infiltrated materials

In a set of samples (1150*L*) with optimized infiltration conditions, **Article III** investigates the effect of increasing the sintering temperature, since higher temperatures generally produce an increase in the grain size, which in turn results in higher transformability of the tetragonal phase and therefore fracture toughness. In effect, by sintering at 1550 ºC and 1600 ºC the grain size was increased to 0.64 μm and 0.78 μm, respectively, obtaining indentation fracture toughness values even higher than for the control AS samples. The change in transformability was confirmed by fractographic observations after using the method detailed in **Article I** and by micro-Raman observations performed across indentation cracks. On the other hand, a slight decrease in strength an hardness and poor LTD resistance were obtained in the samples sintered at higher temperatures, meaning that the standard 1450 ºC sintering temperature provides better overall properties for the Cerium-infiltrated zirconia with the composition studied.

10.1.7. Pressure infiltration of roughened surfaces

Article IV shows that the Ce infiltration treatment has further potential and can be applied directly to zirconia roughened surfaces, which are needed for osseointegration and adhesion purposes in dental implants and crowns/abutments, respectively. Roughness was induced on polished zirconia samples either by sandblasting or by a novel acid etching

protocol. These surfaces were first wetted with a saturated solution of Ce nitrate Hexahydrate in water at 50 MPa pressure. After drying, a diffusion treatment was performed at the sintering temperature, allowing the diffusion of CeO_2 in a thin superficial region of few micrometers in thickness. The surfaces were compared between the three conditions: as-roughened, roughened and thermally treated, roughened and co-doped, in terms of roughness parameters, microstructure, hydrothermal behavior and response to indentation. It was found that the effect of the simple infiltration treatment is extremely beneficial against hydrothermal degradation, guaranteeing the absence of transformation after 30h of autoclave exposure. The surface appearance is modified by the diffusion of CeO_2 decomposed from the salt precursor, reducing surface defects through a remodeling process and eliminating residual stresses induced during the roughening process. Roughness parameters are also affected by the CeO_2 addition, especially in acid-etched surfaces, where remodeling is more evident due to the presence of finer roughness. However, in both cases the final roughness parameters are suitable for adhesion purposes and promising for osseointegration, since they fall in the range of commercial dental implants of proved success. An increase in grain size is observed only in the very first superficial grains, leaving unaltered the bulk and guaranteeing the same mechanical properties. At the same time, the color of the sample is not changed by the co-doping. Therefore, the pressure infiltration method, which can easily be adapted to the CAD/CAM production of dental parts, allows obtaining degradation resistant zirconia roughened pieces without altering the mechanical and esthetical properties of traditional 3Y-TZP.

10.1.8. Small-scale compressive behavior of 3Y-TZP: size effects and plasticity

In **Article VI**, the compressive behavior of 3Y-TZP is studied at the small scale, by milling with FIB micropillars in the range 0.3 – 3.3 μm in diameter and testing them in compression with a nanoindenter and a flat-punch tip. It is found that the compressive strength is of ~7500 MPa and similar among the different diameters tested, which is considerably higher than in the case of macroscopic 2 x 2 x 4 mm prismatic samples, where ~3900 MPa were recorded, as shown in Table 10.2. This difference is imputable to the absence of natural defects in small-scale samples. An important evidence is that significant plastic effects are observed at the small scale, while macroscopic samples show linear behavior until rupture. Moreover, the “yield stress” for plasticity is reduced in sub-micrometric pillars, where the size of the pillar is comparable to the grain size, while it is

approximately constant at ~3 GPa for bigger micropillars. At the same time, the irreversible deformation proceeds through the occurrence of instantaneous strain bursts in the smaller micropillars, while it is a continuous process in bigger ones. This effect, which can be viewed as a size effect in terms of yield stress, follows the rule "smaller being weaker", although it is not a pure effect of the size but rather of the ratio grain size/sample diameter. These results suggest that the brittle-ductile transition is not limited to ceramic monocrystals only, but is also exhibited by polycrystals showing phase transformation where processing defects are not important. The plasticity can be enhanced in these materials by modifying the transformability of the metastable phase and by increasing the ratio grain size/sample diameter.

Table 10.2. Comparison of failure stress (σ*) and failure strain (ε*) for micropillars and 2 x 2 x 4 mm bulk specimens.

	Micropillars				Bulk Samples 2x2x4 mm
	3.3 μm	1 μm	0.65 μm	0.3 μm	
σ* (MPa)	7442±788	7061±563	7658±523	7489±912	3907±291
ε* (%)	6.85±1.23	6.22±1.13	6.88±0.85	7.08±0.74	~2

Additional plasticity is observed when the stress is held constant at high values in the course of a monotonic test. This additional plasticity, which is not instantaneous as the strain bursts associated to phase transformation, may be associated to dislocation glide at room temperature, which may be activated by the high stresses implicated in the micro-compression experiments. The occurrence of plasticity induced by mechanisms other than transformation plasticity is also suggested by STEM/TEM observations of electron-transparent lamellas extracted from retrieved micropillars and by the local shape change observed by SEM after testing.

Cyclic loading-unloading tests at increasing peak stress show that the irreversible component of the strain increases with the applied stress, meaning that phase transformation under compression occurs first in preferentially orientated grains where the strain can be easily accommodated by the tetragonal-monoclinic orientation relationship and the constraint imposed by the surrounding grains, and is then progressively extended to untransformed regions when the necessary stress is reached. The unloading stiffness of the pillar is increasing with increasing peak stresses, which can be the result of both the higher elastic modulus of the monoclinic phase with respect to the tetragonal and the increase in the load-transfer area due to plastic deformation, especially in the upper part of the pillar.

Failure occurs by shear faulting in micropillars, from defects that are nucleated by stress localization at the intersection of transformation variants and grain boundaries. These defects, which are in principle independent of pillar size and depend rather on the grain size, are only seldom observed on the cross-section of pillars retrieved before failure. Instead, the fracture surface has a mixed intergranular-transgranular appearance, with the presence of numerous microcracks, meaning that many defects are nucleated close to the failure stress, when the incompatible strain and high local stresses associated to multivariant transformation are responsible for the simultaneous nucleation of many flaws. Failure can occur when the density of transformation-induced microcracks is enough for merging, which may happen through their interaction or by the nucleation of wing cracks. The fracture aspect reflects this mechanism of crack nucleation, which is typically intergranular, and merging.

Cyclic loading/unloading tests at constant stress amplitude have demonstrated that there is no significant slope change with the number of cycles, meanwhile loading-unloading loops become thinner (cyclic hardening) and reach a saturation stage. By increasing the peak stress above a threshold level, the loops become thicker, meaning that additional damage is created with each loop, until reaching the compressive failure.

10.1.9. Micropillar compression inside the degraded layer

Micropillars of different sizes (0.3 μm, 0.7 μm and 3.3 μm) have been milled entirely inside the surface zirconia degraded layer in **Article V** and their compressive behavior has been compared to non-degraded micropillars. In this way, completely degraded samples could be tested, broadening the knowledge about the mechanical behavior of zirconia after degradation. The compressive failure strength and strain are reduced by the action of hydrothermal degradation to values between 2 and 4 GPa, due to the presence of degradation-induced microcracks. These cracks, which are generally orientated along planes parallel to the surface exposed to hydrothermal aging, follow actually the grain boundaries. Under compression, the faces of cracks that are not perpendicular to the compression axis tend to slide on each other, either nucleating wing cracks or merging through mode-II cracks.

While the failure values are similar among different tests and close to 2 GPa for degraded pillars of 3.3 μm and 0.7 μm diameter, important scatter is registered for 0.3 μm pillars, obtaining in the latter generally higher failure stresses and strains, as well as initial stiffness values, and showing discontinuous strain bursts. This evidence is related to the presence of few grain boundaries inside the sub-micrometric pillars, and so of few

degradation microcracks or weakened interfaces. The fracture mechanism also changes by reducing the pillar size, shifting from axial splitting to mode-II, as a consequence of the statistical occurrence of favorably orientated defects and their interaction with the surface.

Cyclic loading/unloading tests have proved that an irreversible strain component is present also for degraded micropillars. In this case the strain can be associated to crack closure and sliding under the presence of friction forces, and crack nucleation/growth under loading. Time-dependent strains have also been recorded, but with an important difference with respect to the non-degraded material in that the strain is not additive for the degraded case and occurs also at low stress levels. These strains in the degraded pillars are therefore associated to environmental crack growth, suggesting an equivalence between time and stress level: the irreversible strain contribution obtained when increasing the stress to a certain value due to subcritical crack growth can be obtained while holding a lower stress during a sufficient time.

10.1.10. Small-scale bending behavior of 3Y-TZP and comparison for orientated cantilevers inside the degraded layer

The small-scale behavior of 3Y-TZP is significantly different from the macroscopic behavior also in bending, as demonstrated in **Article II**, where micro-cantilevers of approximately 3 x 3 x 10 μm were milled by FIB from the material surface and tested in flexure using an in-situ nanoindenter inside a scanning electron microscope. Exceptional failure stresses of 4100-4600 MPa were recorded, accompanied by an evident deformation of the beam, and plastic strain at failure between 0.8% and 1.5%. Again, these properties are imputable to the lack of processing defects and are controlled by phase transformation, but this time the failure stress is 4 times higher than for macroscopic specimens, where 1000-1200 MPa are usually found in bending. Transformation-induced plasticity plays an important role in the deformation behavior of the micro-cantilever, with deviations from linearity observed above ~3 GPa, similarly to the compression case.

After testing micro-cantilevers milled from the surface degraded layer, it was proved that the mechanical response is clearly anisotropic after degradation due to the preferential orientation of degradation-induced micro-cracks. In the case of micro-cantilevers parallel to the degraded surface, the initial stiffness is similar as for the non-degraded samples, while the bending strength is reduced to ~1200 MPa. On the contrary, for cantilevers milled perpendicularly to the surface, the initial stiffness is reduced by ~70% and the bending

strength is of about 600 MPa. These differences are both consequences of the orientation distribution of degradation cracks, which open under mode-I stress intensity factor in the latter case, affecting the stiffness and lowering the bending strength.

10.2. General conclusions

- The problem of zirconia low-temperature degradation has been solved by infiltration processing with solutions containing CeO_2 precursors.
- Infiltration at the pre-sintered state allows the design of a material with graded composition and higher CeO_2 close to the surface, suitable for posterior hard machining and polishing. In this material, slight changes in the local mechanical properties are unavoidable, which are minimized in optimized conditions. Pressure infiltration after surface roughening treatments for increasing osseointegration and adhesion is suitable for dense materials producing a thin CeO_2 enriched surface region and no change mechanical properties.
- At the small scale, flaw-free polycrystalline zirconia can exhibit exceptional properties. Failure stress is strongly enhanced, allowing the activation of deformation mechanisms not observable in the bulk state. Transformation plasticity plays a major role in the deformation response, resulting in important deviations from the elastic behavior and large strains at failure. Moreover, the yield stress for phase transformation is lower for sub-micrometric samples, where the ratio between the external surface and the grain boundary area is increased. Additional deformation mechanisms are suggested in compression as a result of the high applied stress.
- The properties of zirconia are greatly impaired by hydrothermal degradation and this change has been quantified by small-scale bending and compression tests, showing that degradation-induced microcracks control the behavior, while the damage is clearly anisotropic.

10.3. Impact and perspectives

The proposed solutions to hydrothermal degradation can have the technological impact of allowing a wider exploitation of zirconia-based materials in biomedical applications and, more in general, in humid environments. The infiltration at the pre-sintered state may allow the reintroduction of zirconia as load-bearing material for joint replacement, or for other applications where load is transferred through the surface. The co-doping of roughened

surfaces through pressure infiltration can foster the development of long-lasting dental implants, crowns and abutments with stable long-lasting surfaces, avoiding the current concerns about the possibility of performance loss with time. The validation of the surfaces obtained with the proposed methods for osseointegration could open the path to the design of all-ceramic reliable dental systems.

Infiltration processing can be used with other precursors to obtain ceramic nanocomposites and, more in general, functionally-graded materials where the properties are optimized for the function of the surface and bulk regions, without the formation of interfaces.

The small-scale techniques employed in this dissertation have demonstrated to be valid tools for the study of the micromechanics and damage of phase-transforming materials in small volumes, and have provided novel insights on the behavior of ceramic polycrystals. The superior properties exhibited by zirconia at the small scale could be exploited for the design of high strength miniaturized devices, nanostructured surfaces or nano-powders. Moreover, the high stresses involved in these tests can allow the study of deformation mechanisms otherwise impossible to observe at room temperature, paving the way to further research on the role of grain size, orientation, and time-dependent behavior.

References

[1] O. Ruff, F. Ebert, and E. Stephen, "Contributions to the ceramics of highly refractory materials: II System system zirconia-lime," *Zeitschrift für Anorg. und Allg. Chemie*, vol. 180, pp. 215–24, 1929.

[2] R. C. Garvie, R. H. J. Hannink, and R. T. Pascoe, "Ceramic steel?," *Nature*, vol. 258, no. 5537, pp. 703–704, Dec. 1975.

[3] C. Piconi and G. Maccauro, "Zirconia as a ceramic biomaterial.," *Biomaterials*, vol. 20, no. 1, pp. 1–25, Jan. 1999.

[4] P. Christel, A. Meunier, J. M. Dorlot, J. M. Crolet, J. Witvoet, L. Sedel, and P. Boutin, "Biomechanical Compatibility and Design of Ceramic Implants for Orthopedic Surgery," *Ann. N. Y. Acad. Sci.*, vol. 523: Bioce, pp. 234–56, Jan. 1988.

[5] I. Denry and J. R. Kelly, "State of the art of zirconia for dental applications.," *Dent. Mater.*, vol. 24, pp. 299–307, Mar. 2008.

[6] S. Lawson, "Environmental Degradation of Zirconia Ceramics," *J. Eur. Ceram. Soc.*, vol. 15, pp. 485–502, 1995.

[7] J. Chevalier, L. Gremillard, A. V. Virkar, and D. R. Clarke, "The Tetragonal-Monoclinic Transformation in Zirconia: Lessons Learned and Future Trends," *J. Am. Ceram. Soc.*, vol. 92, no. 9, pp. 1901–1920, Sep. 2009.

[8] J. A. Muñoz Tabares, E. Jiménez-Piqué, and M. Anglada, "Subsurface evaluation of hydrothermal degradation of zirconia," *Acta Mater.*, vol. 59, no. 2, pp. 473–484, Jan. 2011.

[9] Y. Gaillard, E. Jiménez-Piqué, F. Soldera, F. Mücklich, and M. Anglada, "Quantification of hydrothermal degradation in zirconia by nanoindentation," *Acta Mater.*, vol. 56, no. 16, pp. 4206–4216, Sep. 2008.

[10] "Recall of Zirconia ceramic femoral heads for hip implants," *U.S. Food and Drug Administration*, 2001. [Online]. Available: http://www.fda.gov/cdrh/recalls/zirconiahip.html.

[11] I. C. Clarke, "Metastable Nature of Zirconia Femoral Heads From a 20-Year Perspective Of Clinical and Simulator Wear Studies," *Semin. Arthroplasty*, vol. 17, no. 3–4, pp. 165–178, Sep. 2006.

[12] G. Pezzotti, T. Saito, Y. Takahashi, K. Fukatsu, and N. Sugano, "Surface Topology of Advanced Alumina/Zirconia Composite Femoral Head as Compared with Commercial Femoral Heads Made of Monolithic Zirconia," *J. Am. Ceram. Soc.*, vol. 94, no. 3, pp. 945–950, Mar. 2011.

[13] F. Filser, P. Kocher, and L. J. Gauckler, "Net-shaping of ceramic components by direct ceramic machining," *Assem. Autom.*, vol. 23, no. 4, pp. 382–390, 2003.

[14] H. G. Scott, "Phase relationships in the zirconia-yttria system," *J. Mater. Sci.*, vol. 10, pp. 1527–1535, 1975.

[15] O. Fabrichnaya and F. Aldinger, "Assessment of thermodynamic parameters in the system ZrO2 – Y2O3 – Al2O3," *Zeitschrift für Met.*, vol. 95, no. 1, pp. 27–39, 2004.

[16] R. H. J. Hannink, P. M. Kelly, and B. C. Muddle, "Transformation Toughening in ZrO2-Containing Ceramics," *J. Am. Ceram. Soc.*, vol. 83, no. 3, pp. 461–487, Oct. 2000.

[17] M. V Swain and L. R. F. Rose, "Strength Limitations of Transformation-Toughened Zirconia Alloys," *J. Am. Ceram. Soc.*, vol. 69, no. 7, pp. 511–518, Jul. 1986.

[18] P. M. Kelly and L. R. Francis Rose, "The martensitic transformation in ceramics — its role in transformation toughening," *Prog. Mater. Sci.*, vol. 47, no. 5, pp. 463–557, Jan. 2002.

[19] X. Guo, "Property degradation of tetragonal zirconia induced by low-temperature defect reaction with water molecules," *Chem. Mater.*, vol. 16, no. 21, pp. 3988–3994, 2004.

[20] P. Li and I.-W. Chen, "Effect of Dopants on Zirconia Stabilization-An X-ray Absorption Study: I, Trivalent Dopants," *J. Am.*, vol. 77, no. 1, pp. 118 –128, 1994.

[21] S. Fabris, A. T. Paxton, and M. W. Finnis, "A Stabilization Mechanism of Zirconia Based on Oxygen Vacancies Only," *Acta Mater.*, vol. 50, pp. 5171–5178, 2002.

[22] P. Li, I.-W. Chen, and J. E. Penner-hahn, "Effect of Dopants on Zirconia Stabilization-An X-ray Absorption Study: II, Tetravalent Dopants," *J. Am. Ceram. Soc.*, vol. 77, no. 5, pp. 1281–1288, 1994.

[23] P. Li, I.-W. Chen, and J. E. Penner-hahn, "Effect of Dopants on Zirconia Stabilization-An X-ray Absorption Study: III, Charge-Compensating Dopants," *J. Am. Ceram. Soc.*, vol. 77, no. 5, pp. 1289–95, 1994.

[24] "DoITPoMS Micrograph Library, University of Cambridge." [Online]. Available: http://www.doitpoms.ac.uk/tlplib/fuel-cells/sofc_electrolyte.php.

[25] T. Miyazaki, Y. Hotta, J. Kunii, S. Kuriyama, and Y. Tamaki, "A review of dental CAD/CAM: current status and future perspectives from 20 years of experience.," *Dent. Mater. J.*, vol. 28, no. 1, pp. 44–56, Jan. 2009.

[26] J. Chevalier and L. Gremillard, "Ceramics for medical applications: A picture for the next 20 years," *J. Eur. Ceram. Soc.*, vol. 29, no. 7, pp. 1245–1255, Apr. 2009.

[27] M. Hisbergues, S. Vendeville, and P. Vendeville, "Zirconia: Established facts and perspectives for a biomaterial in dental implantology.," *J. Biomed. Mater. Res. B. Appl. Biomater.*, vol. 88, no. 2, pp. 519–29, Feb. 2009.

[28] X. Guo, "Low temperature degradation mechanism of tetragonal zirconia ceramics in water: role of oxygen vacancies," *Solid state ionics*, vol. 112, no. 1, pp. 113–116, 1998.

[29] X. Guo and T. Schober, "Water incorporation in tetragonal zirconia," *J. Am. Ceram. Soc.*, vol. 87, no. 4, pp. 746–748, 2004.

[30] H. Schubert and F. Frey, "Stability of Y-TZP during hydrothermal treatment: neutron experiments and stability considerations," *J. Eur. Ceram. Soc.*, vol. 25, no. 9, pp. 1597–1602, Jun. 2005.

[31] T. Duong, A. M. Limarga, and D. R. Clarke, "Diffusion of Water Species in Yttria-Stabilized Zirconia," *J. Am. Ceram. Soc.*, vol. 92, no. 11, pp. 2731–2737, Nov. 2009.

[32] J. Chevalier, L. Gremillard, and S. Deville, "Low-Temperature Degradation of Zirconia and Implications for Biomedical Implants," *Annu. Rev. Mater. Res.*, vol. 37, no. 1, pp. 1–32, Aug. 2007.

[33] C. Piconi, G. Maccauro, L. Pilloni, W. Burger, F. Muratori, and H. G. Richter, "On the fracture of a zirconia ball head.," *J. Mater. Sci. Mater. Med.*, vol. 17, no. 3, pp. 289–300, Mar. 2006.

[34] J. Chevalier, S. Deville, E. Münch, R. Jullian, and F. Lair, "Critical effect of cubic phase on aging in 3mol% yttria-stabilized zirconia ceramics for hip replacement prosthesis.," *Biomaterials*, vol. 25, no. 24, pp. 5539–45, Nov. 2004.

[35] S. Deville, J. Chevalier, and L. Gremillard, "Influence of surface finish and residual stresses on the ageing sensitivity of biomedical grade zirconia.," *Biomaterials*, vol. 27, no. 10, pp. 2186–92, Apr. 2006.

[36] S. Schmauder and H. Schubert, "Significance of Internal Stresses for the Martensitic Transformation in Yttria-Stabilized Tetragonal Zirconia Polycrystals During Degradation," *J. Am. Ceram. Soc.*, vol. 69, no. 7, pp. 534–540, 1986.

[37] M. Watanabe, S. Iio, and I. Fukura, "Aging behaviour of Y-TZP," in *Advances in Ceramics Vol. 12, Science and Technology of Zirconia II*, 1984, pp. 391–398.

[38] K. Tsukuma, Y. Kubota, and T. Tsukidate, “Thermal and mechanical properties of Y2O3-stabilized tetragonal zirconia polycrystals,” in *Advances in Ceramics Vol. 12, Science and Technology of Zirconia II*, 1984, pp. 382–390.

[39] I. M. Ross, W. M. Rainforth, D. W. McComb, A. . Scott, and R. Brydson, “The role of trace additions of alumina to yttria–tetragonal zirconia polycrystals (Y–TZP),” *Scr. Mater.*, vol. 45, no. 6, pp. 653–660, Sep. 2001.

[40] K. Kuroda, H. Saka, M. Watanabe, and T. Imura, “Tetragonal to monoclinic transformation in ZrO2-Y2O3 ceramics,” in *Proceedings of the International Conference on Martensitic transformations. ICOMAT-86*, 1986, pp. 1161–1166.

[41] J. Chevalier, B. Cales, and J. M. Drouin, “Low-Temperature Aging of Y-TZP Ceramics,” *J. Am. Ceram. Soc.*, vol. 82, no. 8, pp. 2150–2154, 1999.

[42] S. Deville and J. Chevalier, “Martensitic Relief Observation by Atomic Force Microscopy in Yttria-Stabilized Zirconia,” *J. Am. Ceram. Soc.*, vol. 86, no. 12, pp. 2225–2227, 2003.

[43] H.-Y. Lu and S.-Y. Chen, “Low-Temperature Aging of t-ZrO2 Polycrystals with 3 mol% Y2O3,” *J. Am. Ceram. Soc.*, vol. 70, no. 8, pp. 537–541, 1987.

[44] H. Tsubakino, K. Sonoda, and R. Nozato, “Martensite transformation behaviour during isothermal ageing in partially stabilized zirconia with and without alumina addition,” *J. Mater. Sci. Lett.*, vol. 12, pp. 196–198, 1993.

[45] V. Lughi and D. R. Clarke, “Low-temperature transformation kinetics of electron-beam deposited 5 wt.% yttria-stabilized zirconia,” *Acta Mater.*, vol. 55, no. 6, pp. 2049–2055, 2007.

[46] J.-D. Lin and J. G. Duh, “Correlation of mechanical properties and composition in tetragonal CeO2-Y2O3-ZrO2 ceramic system,” *Mater. Chem. Phys.*, vol. 78, pp. 246–252, 2003.

[47] J.-D. Lin and J. G. Duh, “Mechanical properties and resistance to hydrothermal aging of ceria-and yttria-doped tetragonal zirconia ceramics,” *Mater. Chem. Phys.*, vol. 77, pp. 808–818, 2003.

[48] M. T. Hernandez, J. R. Jurado, P. Duran, and J. L. G. Fierro, “Subeutectoid Degradation of Yttria-Stabilized Tetragonal Zirconia Polycrystal and Ceria-Doped Yttria-Stabilized Tetragonal Zirconia Polycrystal Ceramics,” *J. Am. Ceram. Soc.*, vol. 74, no. 6, pp. 1254–1258, 1991.

[49] “ISO 13356: Implants for surgery—ceramic materials based on yttria- stabilized tetragonal zirconia (Y-TZP),” 1997.

[50] M. E. Roy, L. A. Whiteside, B. J. Katerberg, and J. A. Steiger, “Phase transformation , roughness , and microhardness of artificially aged yttria- and magnesia-stabilized zirconia femoral heads,” *J. Biomed. Mater. Res. Part A*, no. 2, 2007.

[51] M. Yashima, H. Takashina, M. Kakihana, and M. Yoshimura, “Low Temperature Phase Equilibria by the Flux Method and the Metastable–Stable Phase Diagram in the ZrO2–CeO2 System,” *J. Am. Ceram. Soc.*, vol. 77, no. 7, pp. 1869–1874, 1994.

[52] V. Sergo, C. Schmid, S. Meriani, and A. G. Evans, “Mechanically Induced Zone Darkening of Alumina/Ceria-Stabilized Zirconia Composites,” *J. Am. Ceram. Soc.*, vol. 77, no. 11, pp. 2971–2976, 1994.

[53] G. S. A. M. Theunissen, A. J. A. Winnubst, and A. J. Burggraaf, “Surface and grain boundary analysis of doped zirconia ceramics studied by AES and XPS,” *J. Mater. Sci.*, vol. 27, pp. 5057–5066, 1992.

[54] M. M. R. Boutz, A. J. A. Winnubst, B. Langerak, R. Olde Scholtenhuis, K. Kreuwel, and A. Burggraaf, “The effect of ceria co-doping on chemical stability and fracture toughness of Y-TZP,” *J. Mater. Sci.*, vol. 30, no. 7, pp. 1854–1862, 1995.

[55] K. Tsukuma and M. Shimada, “Strength, fracture toughness and Vickers hardness of CeO2-stabilized tetragonal ZrO2 polycrystals (Ce-TZP),” *J. Mater. Sci.*, vol. 20, no. 4, pp. 1178–1184, Apr. 1985.

[56] C. Zhao, J. Vleugels, L. Vandeperre, B. Basu, and O. Van Der Biest, “Y-TZP/Ce-TZP functionally graded composite,” *J. Mater. Sci. Lett.*, vol. 17, pp. 1453–1455, 1998.

[57] F. G. Marro, J. Valle, a. Mestra, and M. Anglada, “Surface modification of 3Y-TZP with cerium oxide,” *J. Eur. Ceram. Soc.*, vol. 31, no. 3, pp. 331–338, Mar. 2011.

[58] C. Pecharroman, J. F. Bartolomé, J. Requena, J. S. J. S. Moya, S. Deville, J. Chevalier, G. Fantozzi, R. Torrecillas, and B. C. Pecharromµn, “Percolative Mechanism of Aging in Zirconia-Containing Ceramics for Medical Applications,” *Adv. Mater.*, vol. 15, no. 6, pp. 507–511, 2003.

[59] K. Cherif, B. Gueroult, and M. Rigaud, “Wear behaviour of alumina toughened zirconia materials,” *Wear*, vol. 199, no. 1, pp. 113–121, Nov. 1996.

[60] T. SATO and M. SHIMADA, “Crystalline Phase Change in Yttria-Partially-Stabilized Zirconia by Low-Temperature Annealing,” *J. Am. Ceram. Soc.*, vol. 67, no. 10, pp. C–212–C–213, 1984.

[61] K. Tsukuma, K. Ueda, K. Matsushita, and M. Shimada, “High-Temperature Strength and Fracture Toughness of Y2O3-Partially-Stabilized ZrO2/Al2O3 Composites,” *J. Am. Ceram. Soc.*, vol. 68, no. 2, pp. C–56–C–58, Feb. 1985.

[62] J. Schneider, S. Begand, R. Kriegel, C. Kaps, W. Glien, and T. Oberbach, “Low-Temperature Aging Behavior of Alumina-Toughened Zirconia,” *J. Am. Ceram. Soc.*, vol. 91, no. 11, pp. 3613–3618, Nov. 2008.

[63] W. C. Oliver and G. M. Pharr, “An improved technique for determining hardness and elastic modulus using load and displacement sensing indentation experiments,” *J. Mater. Res.*, vol. 7, no. 6, pp. 1564–1583, 1992.

[64] X. Li and B. Bhushan, "A review of nanoindentation continuous stiffness measurement technique and its applications," *Mater. Charact.*, vol. 48, no. 1, pp. 11–36, Feb. 2002.

[65] J. R. Greer, W. C. Oliver, and W. D. Nix, "Size dependence of mechanical properties of gold at the micron scale in the absence of strain gradients," *Acta Mater.*, vol. 53, no. 6, pp. 1821–1830, Apr. 2005.

[66] N. A. Fleck, G. M. Muller, M. F. Ashby, and J. W. Hutchinson, "Strain gradient plasticity: theory and experiment," *Acta Metall. Mater.*, vol. 42, no. 2, pp. 475–487, Feb. 1994.

[67] A. G. Evans and J. S. Stolken, "A microbend test method for measuring the plasticity length scale," *Acta Mater.*, vol. 46, no. 14, pp. 5109–5115, 1998.

[68] W. D. Nix and H. Gao, "Indentation size effects in crystalline materials: A law for strain gradient plasticity," *J. Mech. Phys. Solids*, vol. 46, no. 3, pp. 411–425, 1998.

[69] M. F. Horstemeyer, M. I. Baskes, and S. J. Plimpton, "Length scale and time scale effects on the plastic flow of fcc metals," *Acta Mater.*, vol. 49, no. 20, pp. 4363–4374, Dec. 2001.

[70] M. D. Uchic, D. M. Dimiduk, J. N. Florando, and W. D. Nix, "Exploring specimen size effects in plastic deformation of Ni3(Al, Ta)," *MRS Proc.*, vol. 753, p. BB1.4, Jan. 2002.

[71] M. D. Uchic, D. M. Dimiduk, J. N. Florando, and W. D. Nix, "Sample dimensions influence strength and crystal plasticity.," *Science*, vol. 305, no. 5686, pp. 986–9, Aug. 2004.

[72] M. D. Uchic, P. a. Shade, and D. M. Dimiduk, "Plasticity of Micrometer-Scale Single Crystals in Compression," *Annu. Rev. Mater. Res.*, vol. 39, no. 1, pp. 361–386, Aug. 2009.

[73] M. D. Uchic and D. M. Dimiduk, "A methodology to investigate size scale effects in crystalline plasticity using uniaxial compression testing," *Mater. Sci. Eng. A*, vol. 400–401, pp. 268–278, Jul. 2005.

[74] O. Kraft, P. a. Gruber, R. Mönig, and D. Weygand, "Plasticity in Confined Dimensions," *Annu. Rev. Mater. Res.*, vol. 40, no. 1, pp. 293–317, Jun. 2010.

[75] J. R. Greer and J. T. M. De Hosson, "Plasticity in small-sized metallic systems: Intrinsic versus extrinsic size effect," *Prog. Mater. Sci.*, vol. 56, no. 6, pp. 654–724, Aug. 2011.

[76] S. Korte and W. J. Clegg, "Discussion of the dependence of the effect of size on the yield stress in hard materials studied by microcompression of MgO," *Philos. Mag.*, vol. 91, no. 7–9, pp. 1150–1162, Mar. 2011.

[77] P. S. S. Leung and a. H. W. Ngan, “Size effect on the strength of micron-sized polycrystals – A dislocation dynamics simulation study,” *Scr. Mater.*, vol. 69, no. 3, pp. 235–238, Aug. 2013.

[78] a. Rinaldi, P. Peralta, C. Friesen, and K. Sieradzki, “Sample-size effects in the yield behavior of nanocrystalline nickel,” *Acta Mater.*, vol. 56, no. 3, pp. 511–517, 2008.

[79] D. Jang and J. R. Greer, “Size-induced weakening and grain boundary-assisted deformation in 60 nm grained Ni nanopillars,” *Scr. Mater.*, vol. 64, no. 1, pp. 77–80, 2011.

[80] J. Michler, K. Wasmer, S. Meier, F. Östlund, and K. Leifer, “Plastic deformation of gallium arsenide micropillars under uniaxial compression at room temperature,” *Appl. Phys. Lett.*, vol. 90, 2007.

[81] F. Östlund, P. R. Howie, R. Ghisleni, K. Leifer, W. J. Clegg, and J. Michler, “Ductile – brittle transition in micropillar compression of GaAs at room temperature,” *Philos. Mag.*, vol. 91, no. 7–9, pp. 1190–1199, 2011.

[82] F. Östlund, K. Rzepiejewska-Malyska, K. Leifer, L. M. Hale, Y. Tang, R. Ballarini, W. W. Gerberich, and J. Michler, “Brittle-to-Ductile Transition in Uniaxial Compression of Silicon Pillars at Room Temperature,” *Adv. Funct. Mater.*, vol. 19, no. 15, pp. 2439–2444, Aug. 2009.

[83] S. Korte and W. J. Clegg, “Micropillar compression of ceramics at elevated temperatures,” *Scr. Mater.*, vol. 60, no. 9, pp. 807–810, May 2009.

[84] P. Veyssière, S. H. Kirby, and J. Rabier, “Plastic deformation of MgO : n Al2O3 spinels at temperatures below 1000 °C (0.5 Tm),” *J. Phys. Colloq.*, vol. 41, no. C6, pp. C6–175–C6–178, 1980.

[85] B. Moser, K. Wasmer, L. Barbieri, and J. Michler, “Strength and fracture of Si micropillars : A new scanning electron microscopy-based micro-compression test,” pp. 1–8, 2007.

[86] K. Kendall, “The impossibility of comminuting small particles by compression,” *Nature*, vol. 272, no. 20, pp. 710–711, 1978.

[87] B. L. Karihaloo, “The impossibility of comminuting small particles by compression,” *Nature*, vol. 279, no. 10, pp. 169–170, 1979.

[88] D. D. Stauffer, “Deformation Mechanisms in Nanoscale Brittle Materials,” Univerity of Minnesota, 2011.

[89] P. R. Howie, “Measuring plasticity in brittle materials,” University of Cambridge, 2012.

[90] P. R. Howie, S. Korte, and W. J. Clegg, “Fracture modes in micropillar compression of brittle crystals,” *J. Mater. Res.*, vol. 27, no. 01, pp. 141–151, Sep. 2011.

[91] K. Kendall, “Complexities of Compression Failure,” *Proc. R. Soc. A Math. Phys. Eng. Sci.*, vol. 361, no. 1705, pp. 245–263, May 1978.

[92] W. W. Gerberich, J. Michler, W. M. Mook, R. Ghisleni, D. D. Stauffer, and R. Ballarini, “Scale effects for strength, ductility, and toughness in ‘brittle’ materials,” *J. Mater. Res.*, vol. 24, no. 3, pp. 898–906, 2009.

[93] W. W. Gerberich, W. M. Mook, C. B. Carter, and R. Ballarini, “A crack extension force correlation for hard materials,” *Int. J. Fract.*, vol. 148, no. 2, pp. 109–114, Mar. 2008.

[94] M. Tanaka and K. Higashida, “HVEM characterization of crack tip dislocations in silicon crystals.,” *J. Electron Microsc. (Tokyo).*, vol. 53, no. 4, pp. 353–360, 2004.

[95] A. Montagne, S. Pathak, X. Maeder, and J. Michler, “Plasticity and fracture of sapphire at room temperature: Load-controlled microcompression of four different orientations,” *Ceram. Int.*, vol. 40, no. 1, pp. 2083–2090, 2014.

[96] S. Kiani, K. W. K. Leung, V. Radmilovic, a. M. Minor, J.-M. Yang, D. H. Warner, and S. Kodambaka, “Dislocation glide-controlled room-temperature plasticity in 6H-SiC single crystals,” *Acta Mater.*, vol. 80, pp. 400–406, Nov. 2014.

[97] T. Csanádi, N. Q. Chinh, P. Szommer, J. Dusza, Z. Lenčés, and P. Šajgalík, “Deformation and Fracture of β-Silicon Nitride Micropillars,” *J. Am. Ceram. Soc.*, vol. Rapid Comm, pp. 1–4, Dec. 2014.

[98] S. M. Ueland, Y. Chen, and C. a. Schuh, “Oligocrystalline Shape Memory Alloys,” *Adv. Funct. Mater.*, vol. 22, no. 10, pp. 2094–2099, May 2012.

[99] A. Lai, Z. Du, C. L. Gan, and C. a. Schuh, “Shape memory and superelastic ceramics at small scales.,” *Science*, vol. 341, no. 6153, pp. 1505–8, Sep. 2013.

[100] S. Johansson, J.-A. Schweitz, L. Tenerz, and J. Tirén, “Fracture testing of silicon microelements in situ in a scanning electron microscope,” *J. Appl. Phys.*, vol. 63, no. 10, p. 4799, 1988.

[101] J. McCarthy, Z. Pei, M. Becker, and D. Atteridge, “FIB micromachined submicron thickness cantilevers for the study of thin film properties,” *Thin Solid Films*, vol. 358, pp. 146–151, 2000.

[102] J. N. Ding, Y. G. Meng, and S. Z. Wen, “Specimen size effect on mechanical properties of polysilicon microcantilever beams measured by deflection using a nanoindenter,” *Mater. Sci. Eng. B*, vol. B83, no. 1–3, pp. 42–47, Jun. 2001.

[103] C. Motz, T. Schöberl, and R. Pippan, “Mechanical properties of micro-sized copper bending beams machined by the focused ion beam technique,” *Acta Mater.*, vol. 53, no. 15, pp. 4269–4279, Sep. 2005.

[104] D. E. J. Armstrong, A. J. Wilkinson, and S. G. Roberts, “Measuring anisotropy in Young’s modulus of copper using microcantilever testing,” *J. Mater. Res.*, vol. 24, no. 11, pp. 3268–3276, 2009.

[105] S. Wurster, C. Motz, M. Jenko, and R. Pippan, “Micrometer-sized specimen preparation based on ion slicing technique,” *Adv. Eng. Mater.*, vol. 12, no. 1–2, pp. 61–64, 2010.

[106] T. Sato, S. Ohtaki, T. Fukushima, T. Endo, and M. Shimada, “Mechanical propierties and thermal stability of yttria doped tetragonal zirconia polycrystals with diffused ceria in the surface,” *Mater. Res. Soc. Symp. Proc.*, vol. 78, pp. 147 – 154, 1987.

[107] B. R. Marple and D. J. Green, “Graded compositions and microstructures by infiltration processing,” *J. Mater. Sci.*, vol. 28, no. 17, pp. 4637–4643, 1993.

[108] P. Honeyman-Colvin and F. F. Lange, “Inflitration of Porous Alumina Bodies with Solution Precursors: Strengthening via Compositional Grading, Grain Size Control, and Transformation Toughening,” *J. Am. Ceram. Soc.*, vol. 79, no. 7, pp. 1810–14, 1996.

[109] J. G. Duh, “Liquid infiltration in ZrO2 ceramics,” *J. Mater. Sci. Lett.*, vol. 12, pp. 473 – 475, 1993.

[110] S. J. Glass and D. J. Green, “Mechanical Properties of Infiltrated Alumina-Y-TZP Composites,” *J. Am. Ceram. Soc.*, vol. 79, no. 9, pp. 2227–2236, 1996.

[111] Y. J. Lin and Y. C. Chen, “Cyclic infiltration of porous zirconia preforms with a liquid solution of mullite precursor,” *J. Am. Ceram. Soc.*, vol. 84, no. 1, pp. 71–78, 2001.

[112] W. Wendlandt, “The thermolysis of the rare earth and other metal nitrates,” *Anal. Chim. Acta*, vol. 15, pp. 435–439, 1956.

[113] D. S. Gianola, A. Sedlmayr, R. Mönig, C. a. Volkert, R. C. Major, E. Cyrankowski, S. a S. Asif, O. L. Warren, and O. Kraft, “In situ nanomechanical testing in focused ion beam and scanning electron microscopes.,” *Rev. Sci. Instrum.*, vol. 82, no. 6, p. 063901, Jun. 2011.

[114] C. Shin, H.-H. Jin, W.-J. Kim, and J.-Y. Park, “Mechanical Properties and Deformation of Cubic Silicon Carbide Micropillars in Compression at Room Temperature,” *J. Am. Ceram. Soc.*, vol. 95, no. 9, pp. 2944–2950, Sep. 2012.

Annex A

Article VI: Role of size and plasticity in zirconia micropillars compression

Role of size and plasticity in zirconia micropillars compression

Erik Camposilvan[1,2,*], *Marc Anglada*[1,2]

[1]Department of Materials Science and Metallurgical Engineering, Universitat Politècnica de Catalunya, Av. Diagonal 647, 08028 Barcelona – Spain

[2]Center for Research in NanoEngineering CRnE, Universitat Politècnica de Catalunya, Av. Diagonal 647, Barcelona, 08028, Spain

Abstract

The micropillar compression technique has exhibited the potential of activating the brittle-to-ductile transition in ceramic monocrystals when the micropillar diameter is small enough. Here this technique is applied to polycrystalline tetragonal zirconia, comparing the response of microscopic and macroscopic samples. In micropillars, the absence of the natural defect population typical of bulk zirconia increases considerably the strength, allowing the activation of plastic deformation mechanisms and their study. It is demonstrated that the brittle-to-ductile transition is not limited to ceramic monocrystals only. The main mechanism of plastic deformation is transformation-induced plasticity and the yield stress is shown to be size dependent. The deformation behavior is studied in detail by loading-unloading tests at constant and increasing peak loads, while the microstructure evolution is revealed by FIB cross-sections, TEM and STEM observations performed on lamellas extracted from pillars retrieved before failure. Finally, a failure mechanism is proposed, based on the damage induced by phase transformation rather than the growth of existing defects under compression.

Keywords: Zirconia, micro-pillar, phase transformation, transformation-induced plasticity.

1. Introduction

The Intrinsic mechanical properties of materials, such as yield stress and strength, may exhibit an extrinsic behavior when their volume is greatly reduced. This tendency has been shown to be true in monocrystals, where increasing yield stress is obtained by reducing the sample size. The existence of size effects has been highlighted by testing in different modes, such as micro- and nanoindentation [1,2], torsion tests [3], bending [4,5], tension [6] and compression [7].

The micropillar compression approach has received special attention due to several advantages. Firstly, the absence of strain gradients that are usually responsible for substantial extrinsic contributions and mask the effect of the sole volume and free surfaces [3,8]. Secondly, the relative simplicity of sample preparation and testing is another merit of micro-compression, which can be performed either ex-situ or in-situ under SEM or TEM observation [9], as well as coupled with other electrical and acoustical [10], spectroscopic [11] and diffraction [12] techniques.

The limitations of this approach are mainly related to the micropillar taper angle and the confinement at the base of the specimens imposed by the surrounding material. Other limitations are related to the possible misalignment and the presence of friction forces between the micropillar top surface and the flat-punch indenter. All these effects contribute to the non-uniformity of the micropillar stress state, making difficult to compare samples of different size and taper angle [13–15]. Misaligning of the system leads to underestimation of the elastic modulus, stress concentration at the pillar top edge, and the possibility of failure by buckling instead of compression [15]. Thermal and mechanical drift during testing may also be a source of errors in strain measurement [16].

By compression testing single-crystal micropillars of soft metals one can study the activation of individual slip systems and the yield stress as a function of pillar size. An inverse power-law has been found between the critical resolved shear stress along the slip plane normalized by the shear modulus and the pillar diameter [14,17]. This relationship holds for FCC single crystals, for which the exponent is close to 0.6, meanwhile the behavior in the BCC case is somehow erratic and very sensitive to the initial dislocation density, with the yield stress also scaling with micro-pillar size, but with lower exponents [14]. At the same time, both the extent of the size effect and the length scale where the transition between bulk and small-scale behavior takes place appear to be related to the bulk shear yield stress [18].

Thus, soft materials show more pronounced size effects and the transition occurs in bigger samples.

At present, full understanding of the behavior of polycrystalline micropillars is still lacking. In these materials, a combination of extrinsic and intrinsic length scales seems to affect the overall behavior. Different and conflicting deviations from the Hall-Petch relation have been found by independent studies in polycrystalline wires, sheets and micro-pillars of FCC metals [19]. In particular, in nanocrystalline Nickel it has been shown that the "smaller being stronger" trend can be inverted in polycrystals depending on the ratio thickness/grain size [20]. As a result of dislocation dynamics simulations, two types of behavior have been observed in metals, depending on sample size, grain size, and dislocation density [21]. One is dominated by strain-hardening and follows the Hall-Petch relation; in the other type, plasticity is source-limited and the "smaller being stronger" behavior is expected, reflecting in part the tendency previously observed by Janssen et al. for Aluminum [22].

With reference to structural ceramics, testing of single-crystal micropillars has not received as much attention as for metals. Nevertheless, this technique may be of particular interest in ceramics to investigate the transition from brittle to ductile behavior when the volume becomes small enough [23,24]. In this sense, Korte and Clegg [18] have shown that hard brittle materials like MgO can be deformed plastically at room temperature by micropillar compression. The size effect was similar to BCC metals when activating MgO soft slip systems, while hard slip systems showed a behavior rather similar to the one observed for GaAs [25] and Si [26]. Deformation by dislocation glide during micropillar compression can also be activated at room temperature in high strength ceramic monocrystals like sapphire [27], silicon carbide [28] and silicon nitride [29]. With respect to zirconia, Lai and co-workers [30] have recently shown that single-crystal or oligocrystalline micropillars of zirconia highly doped with Ce and Y can display shape memory and superelastic effects in association with phase transformation under compression, while the presence of other plastic phenomena has not been discussed.

In the present work, the compression behavior of yttria-stabilized zirconia (3Y-TZP) micropillars is studied and compared with the macroscopic behavior. This material is composed of tetragonal-metastable polycrystals with approx. 10 vol.% of stable cubic phase. It is well known that the tetragonal phase can transform into the stable monoclinic phase, transformation that can be activated locally either mechanically by the presence of high stresses [31] or chemically by the diffusion of water species from the environment [31,32].

Here, 3Y-TZP micro- and nano-pillars of different sizes are milled by focused ion beam (FIB) and tested by monotonic and cyclic compression tests in order to study the role of size, plastic deformation and damage. The absence of natural defects typical of macroscopic specimens may increase considerably the micropillars strength, providing some light on the mechanisms of plastic deformation of these materials.

2. Materials and Methods

Commercial spray-dried zirconia powder (TZ-3YSB-E, Tosoh Corp.) was isostatically pressed at 200 MPa in a rod shape and sintered at 1450 ºC in air inside a tubular furnace for 2 hours, obtaining a ceramic with density of 6.06 ± 0.02 g/cm^3 (99.5 ± 0.3% of the theoretical value) as measured by the Archimedes' method. The rod was cut into disks of approx. 1.5 mm thickness, which were ground and polished with diamond pastes down to less than 20 nm Ra. The disks were cut along the diameter and the resulting cross-section was polished using diamond films on a tripod fixture (Struers A/S) to reduce blunting of the cross-sectional edge. The disk halves were mounted on inclinable SEM holders with hard conductive adhesive and coated with a thin carbon layer of ~10 nm. The holder was tilted conveniently to facilitate both the parallel and normal visualization of the sample surface by the electron and ion beams employed during micropillars milling in a Zeiss Neon 40 dual beam station. The surface was visualized tangentially by the ion beam to set the reference angle for milling and then the stage was tilted and oriented accordingly for starting the milling procedures. The micropillars were milled directly into the sample polished surfaces, close to the edge of the cross-section, in order to allow better visualization after testing. Milling was performed with a two-steps procedure that had been optimized for each pillar size in order to minimize the taper angle and maintain similar aspect ratios and reasonable milling times. In the first step a large well, ~34 μm in diameter, was obtained with a relatively high ion current. The size of the well had been adapted to facilitate the compression experiments avoiding contact between the indenter tip and the surface and allowing to locate the pillar by the built-in optical microscopes mounted on the two nanoindenters employed. In the second step, lower currents were used and the milling profile, i.e. the dwell time associated to each pixel as a function of the distance from the pillar axis, was tuned for each pillar size. Four nominal sizes were selected: 3.3 μm, 1 μm, 0.65 μm and 0.30 μm in diameter. The aspect ratio was between 1:2 and 1:4 in all the pillars. A thin cyanoacrylate strip was manually deposited on the half disk from where the samples were milled, approximately 500 μm away from the micropillars

edge, serving as a soft surface for detecting the shape and location of the mark left by the flat-punch tip before testing. The nanoindentation systems employed in testing were an MTS XP Nanoindenter (now Agilent, Oak Ridge, TN) and a CSM Ultra Nano Hardness Tester (CSM Instruments, Peseux, Switzerland). In both systems, the site of the indentation is first selected by imaging the surface with the optical microscope and then the indenter (or the sample, depending on the system) moves to perform the indentation at the selected location. Therefore, the distance between the microscope and the indenter tip has to be properly calibrated. Prior to testing, the SEM holder was tilted to orientate the surface normally to the loading axis and mounted on supports designed for the indenter. Once inside the nanoindentation system, additional adjustments on the tilting angle were performed, if needed, by indenting the cyanoacrylate strip and visualizing the mark with the microscope until a regular shape was observed also at small indentation depths. The loading rates were adjusted to obtain similar strain rates ($1\text{-}3x10^{-3}$ s^{-1}) for all the conditions and tests duration of approximately 40 s (monotonic tests to failure). Accurate microscope-to-indenter calibrations were performed by indenting on the cyanoacrylate strip before each single test to guarantee the correct positioning of the flat-punch tip over the pillar head. This procedure was also useful for cleaning the indenter tip from residual debris from broken samples. Compression testing at constant loading rate was used in all the tests. Repeated loading/unloading tests until rupture were also performed by loading at constant or increasing peak loads and unloading down to a constant low load.

The pillars were visualized before and after testing. The actual diameter, height and taper angle of each pillar were measured from SEM micrographs. Since the maximum stress occurs at the pillar top, the initial diameter measured at this location was used in the calculation of stress. Load-displacement data were converted into stress-strain curves to compare different sample sizes. Some pillars were unloaded before breakage to observe their appearance by SEM and, in selected cases, to observe a FIB cross-section or to lift out a thin lamella from the pillar cross-section. The latter was observed first by Scanning Transmission Electron Microscopy (STEM) inside a Zeiss Neon 40 dual-beam station equipped with a STEM module at 30 KV, obtaining bright field and annular dark field images. Conventional Transmission Electron Microscopy (TEM) observations were later performed with a JEOL 1200 EX-II at 120 KV.

Macroscopic compression tests were carried out on 3Y-TZP prisms of 2 x 2 x 4 mm obtained by cutting and polishing the same sintered rods employed for milling micropillars.

The prisms were tested in an Instron 8562 universal testing machine, transferring the load through two WC-Co plates and recording the displacement with an Instron LVDT 5809R deflectometer with +/- 1mm axial travel.

3. Results

Examples of stress/strain curves obtained during monotonic testing of micropillars are shown in Figure 1. The initial part of these curves shows increasing stiffness in association with the progressive contact between the indenter and the sample and the potential presence of debris/humidity on their surfaces. This is followed by a linear behavior, and finally a significant deviation from linearity until failure. The compressive strength lies between 6.5 to 9.3 GPa, which is much higher than for macroscopic specimens (3.5-4.3 GPa). The latter show a linear elastic behavior until rupture, if we exclude initial deviations from linearity that are the result of the settlement between the sample and the loading plates. Mean values of failure stress (σ^*) and failure strain (ε^*) obtained in monotonic tests are reported in Table 1, where ε^* is the maximum strain measured at failure to which the initial strain associated to contact has been subtracted.

Table 1. Comparison of failure stress (σ^*) and failure strain (ε^*) for micropillars and 2 x 2 x 4 mm bulk specimens.

	Micropillars				Bulk Samples 2x2x4 mm
	3.3 μm	1 μm	0.65 μm	0.3 μm	
σ^* (MPa)	7442±788	7061±563	7658±523	7489±912	3907±291
ε^* (%)	6.85±1.23	6.22±1.13	6.88±0.85	7.08±0.74	~2

Among the micropillars, no evident size effect in terms of strength is appreciated in Fig. 1. In terms of strain, localized strain bursts are observed in the stress-strain curves only for samples with diameter smaller than 1 μm, appearing sometimes at relatively low stress (e.g. ~1700 MPa, see Fig. 1-D). Bigger micropillars show smooth curves until rupture, with increasing curvature at high stresses starting at ~3 GPa. At lower stresses and once the stress-strain curve becomes linear, the slope is from 3% to 37% smaller than the theoretical elastic modulus (210 GPa for 3Y-TZP). This variability is not dependent on the pillar size. In the 0.30 μm micropillars, the slopes of the curve before and after the first discontinuous strain bursts are similar.

The occurrence of transformation-induced plasticity was confirmed by SEM observation of micropillars tested to 85-90% of σ^* and unloaded. The “stripes” observed on

the pillar surface (Figures 2 and 3) are actually transformation bands, which indicate extensive transformation in nearly all grains, suggesting a first explanation for the evident plasticity effects observed in the stress-strain curves.

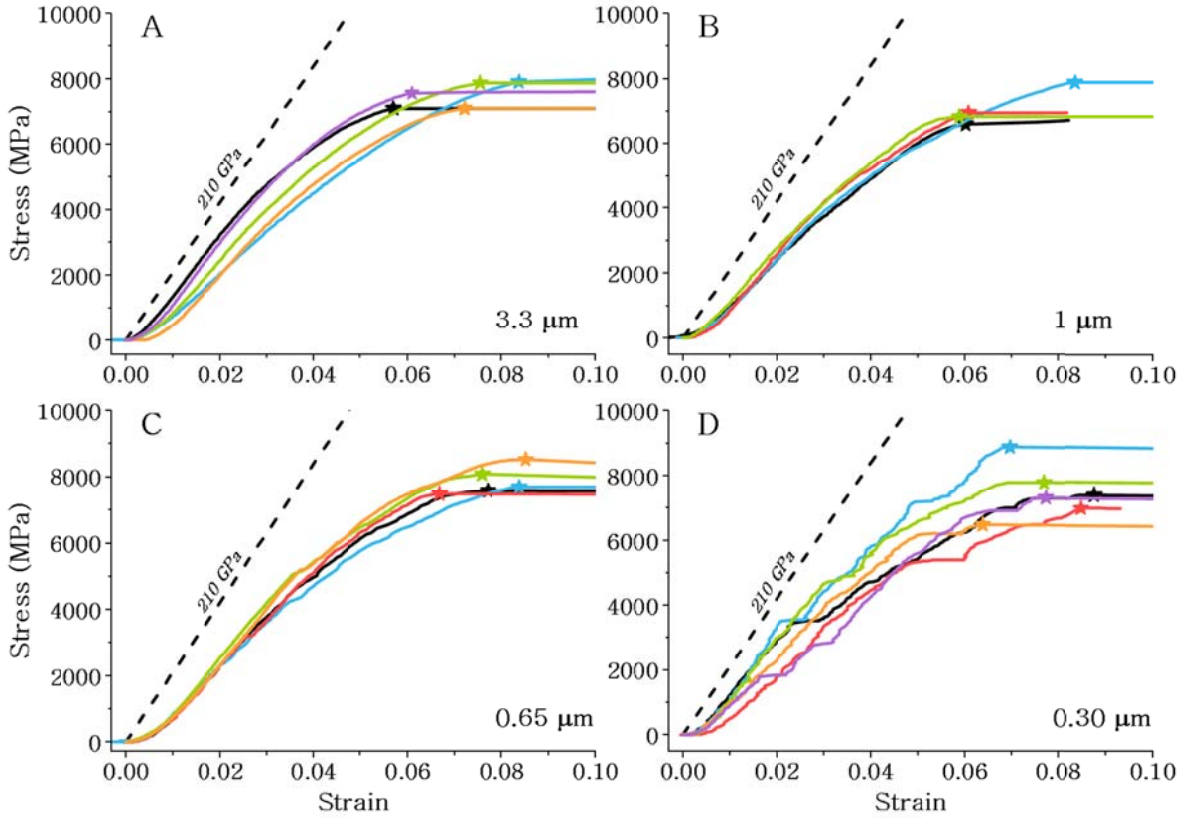

Fig. 1. Stress-strain response of micropillars of different sizes (0.3 µm - 3.3 µm). Failure is marked with a star.

Irreversible deformation can be also appreciated in SEM pictures of the same micropillar (see Fig. 2, C-D and E-F and Fig. 3, A-B) by the permanent change in dimensions after unloading. The pillars appear slightly shorter and thicker once compressed. Remarkable accumulation of martensitic plates was detected around the isolated alumina grains present in the microstructure as a result of the small amount of alumina in the composition of the starting powder (see Fig. 2-B).

The distribution of martensitic plates could be observed in greater detail from FIB cross-sections of tested micropillars (Fig. 3-D) and from the extracted lamellas observed by STEM (Fig. 4) and TEM (Fig. 5). It can be appreciated that the transformation is not limited to the surface but interests the whole volume, with higher concentration in the upper part of the pillar. In the STEM images, the martensitic plates associated with the formation of monoclinic phase are orientated mostly in the range 30º-60º with respect to the loading axis and spread in most of the grains. On the contrary, grains close (but external) to the base of the pillar are not transformed, indicating that sample preparation did not introduce artifacts or

relevant stresses in the foil. The presence of few small intergranular microcracks was sometimes detected on the surface or cross-sections of compressed samples retrieved before failure. In the TEM micrograph of Fig. 5, five small grain-boundary microcracks, which were not observable in the STEM images, can be appreciated at the intersection of transformation bands and grain boundaries. However, these observations from specimens loaded up to 85-90 % of the average strength allow the detection of a rather low crack density. Developed wing cracks are observed in the broken sample of Fig. 6-E, while incipient wing cracks appear in the detail of Fig. 2-G. Moreover, TEM micrographs reveal the presence of some untransformed regions inside the micropillar. These regions have generally a distorted appearance as it was observed for scratching of zirconia in Ref. [33], with the presence of strain-induced contrast and deformed Moiré fringes (see G2 in Fig. 5-A and detail of Fig. 5-B), which are not observed outside the pillar. Some of the martensitic laths show a bended contour (e.g. Fig. 4-G and G1 in Fig. 5-A), in contrast to the usually straight and defined profiles observed in transformed zirconia (see as an example Fig. 5 in Ref. [34]).

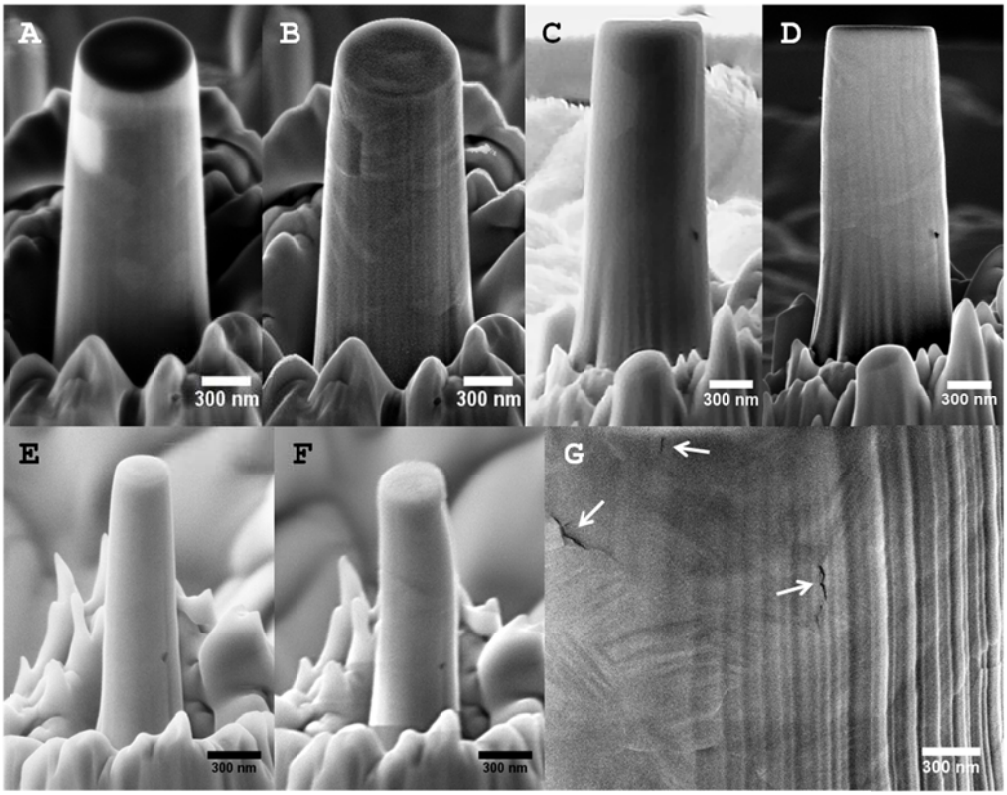

Fig. 2. A-B: Evidence of transformation on the surface of a 0.65 μm diameter pillar after testing to 6 GPa (unloaded before failure). Martensitic laths seem to concentrate around the visible alumina grain. C-D: Shape change in a 0.65 μm pillar after loading to 6.1 GPa. E-F: shape change in a 0.30 μm pillar with evidence of plastic deformation at the top and buckling (loading curve not included in the results). G: surface of a 3.3 μm pillar unloaded before failure. Arrows indicate the presence of microcracks.

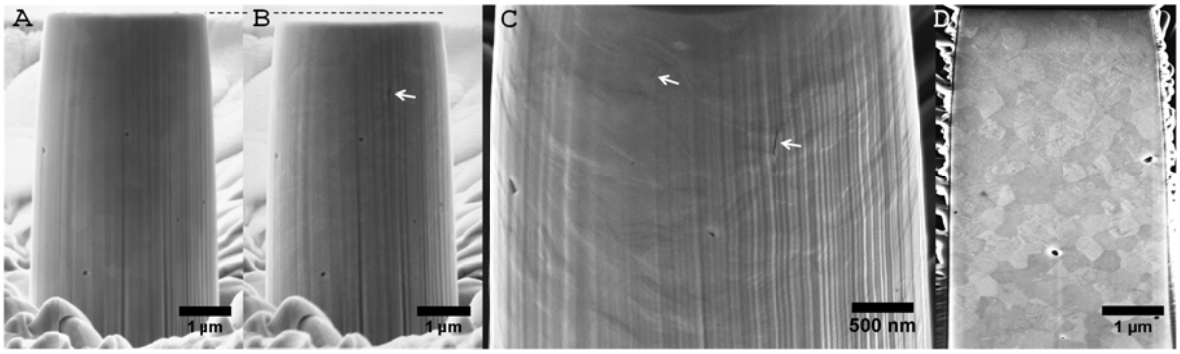

Fig. 3. A-B: 3.3 µm diameter micropillar before and after testing (loaded up to 6.3 GPa), highlighting the change in size, side view. Vertical lines are due to curtain effect during the milling procedure. C: detail showing transformation on the surface and the presence of surface flaws, indicated by arrows. D: FIB cross-section of the same pillar, showing extensive phase transformation. A video displaying a 1µm in-situ test, performed at INM-Saarbrücken, is available in the supporting information.

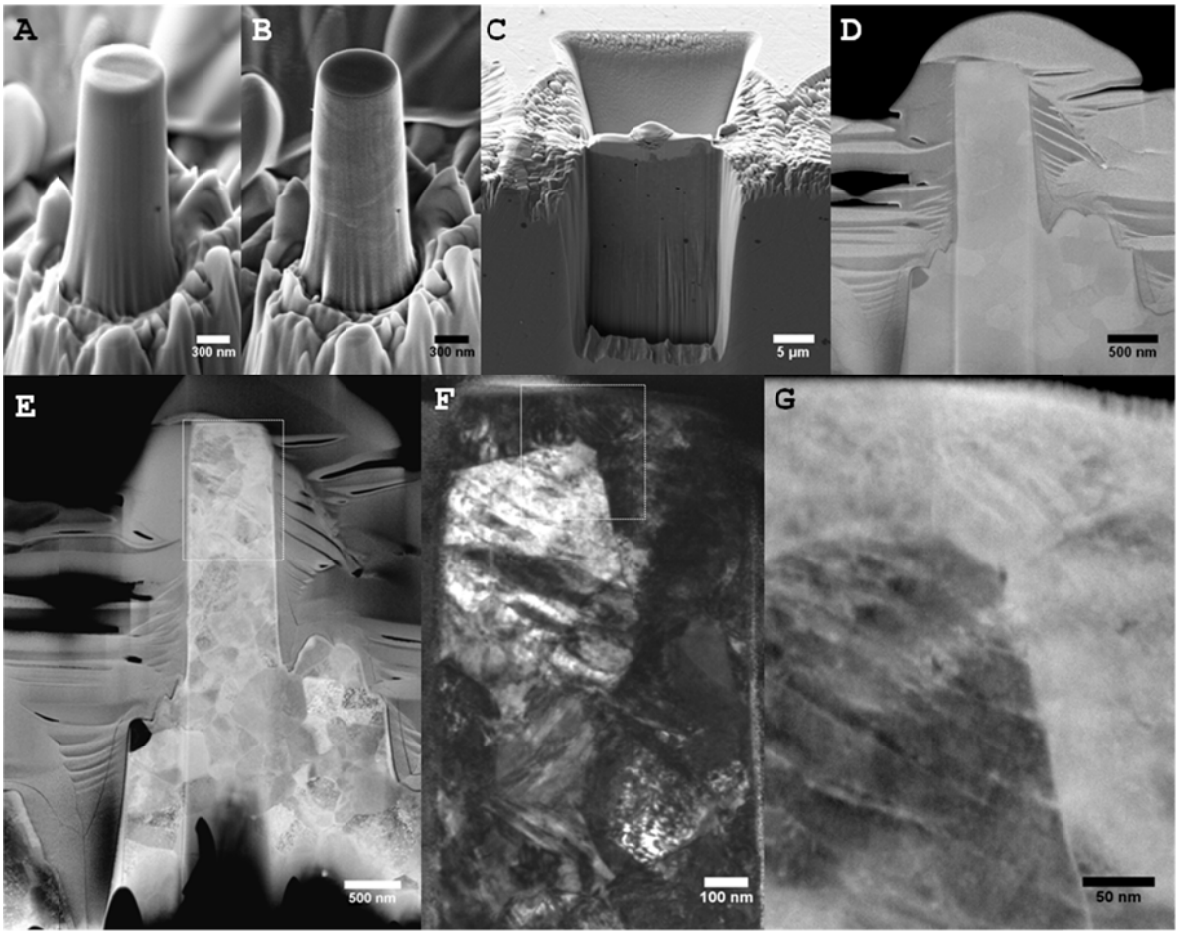

Fig. 4. A-B: 0.65 µm diameter pillar before and after loading up to 6.1 GPa. C-D: Lamella preparation after Pt deposition and SEM observation of the prepared lamella. E: dark field STEM image of the lamella. F: bright field of the upper part of the pillar, showing the preferential inclination of transformation bands. G: Detail of the triple points close to the pillar top. The top-right edge of the pillar has been milled away during the depostition of the Pt protective layer.

SEM imaging of micropillars after failure shows mixed inter-trans-granular fracture, with the presence of many micro-cracks on the fracture surface as reported in Fig. 6-A, D, F.

In some areas, the saw-toothed appearance reflects the contour of individual martensitic plates (Fig. 6-C). Extensive microcracking with evidence of crack merging appears on the external surface of broken micropillars (Fig. 6-B and E). The fracture plane is generally tilted with respect to the loading axis.

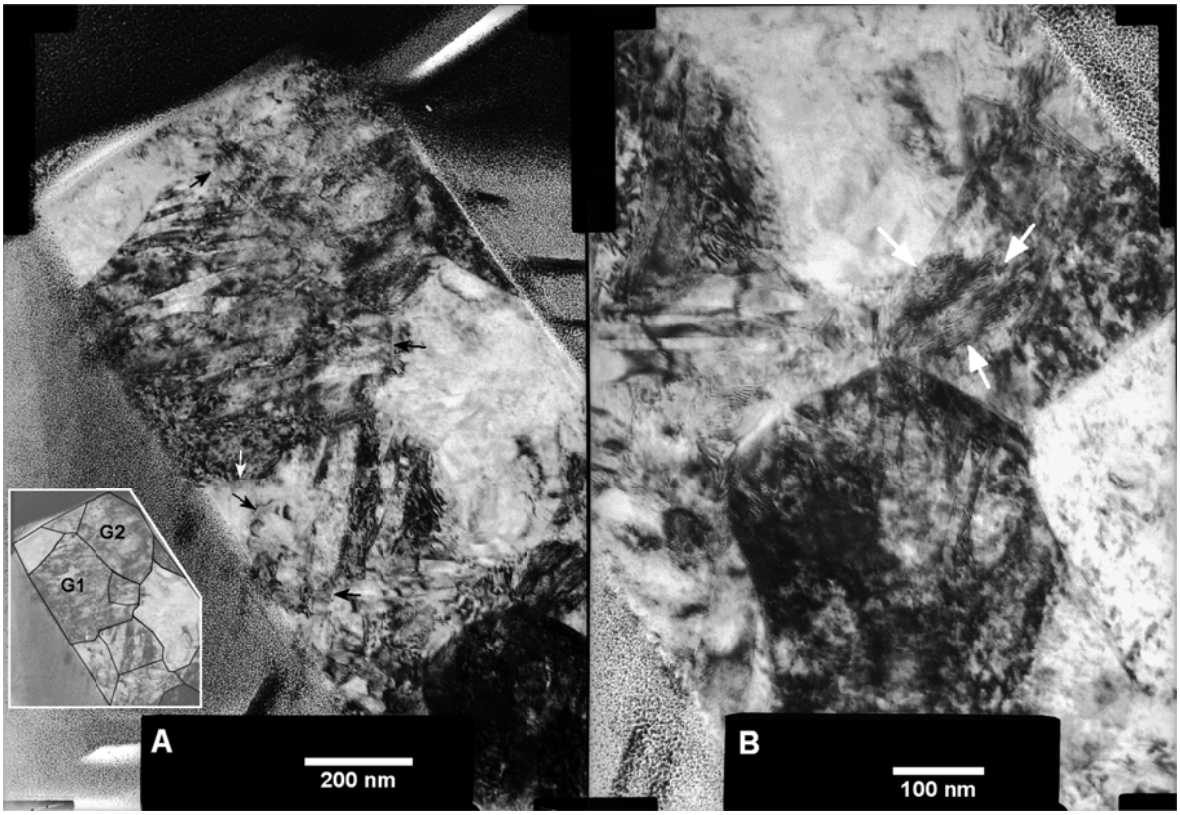

Fig. 5. Bright field TEM images of the micropillar previously imaged by STEM in Fig. 4. The pillar is embedded in a nanocrystalline Pt layer needed for the lift-out procedure. Loading took place from the top-left corner in the axial direction. In A, arrows indicate visible microcracks associated to phase tranformation. In B, which is the bottom region of A at higher magnification, arrows indicate a region with distorted Moiré patterns.

Examples of loading-unloading tests at increasing peak loads are presented in Fig. 7, where the irreversible component of the strain is clearly exhibited. For stresses higher than 3.5 GPa, immediate load reversal induced an unloading curvature at the peak load, which did not appear for load reversals at lower peak loads. By holding the peak load (hold time = 10 s) instead of the immediate reversion, the deformation at constant peak load increased with time, as indicated in the insert of Fig. 7-B. This time–dependent strain at constant load, which increases with the peak load and only appears at stresses higher than 3.5 GPa, should not be confused with the instantaneous strain bursts that were observed in sub-micron pillars loaded monotonically. In the same figure, it can be seen that during the unloading and reloading segments, a narrow hysteresis loop appears, whose width increases slightly with the peak stress. The unloading modulus is close to the theoretical value of 210 GPa for ~3 GPa peak

stress and increases progressively with the peak stress up to a maximum variation of about 20% for ~7 GPa.

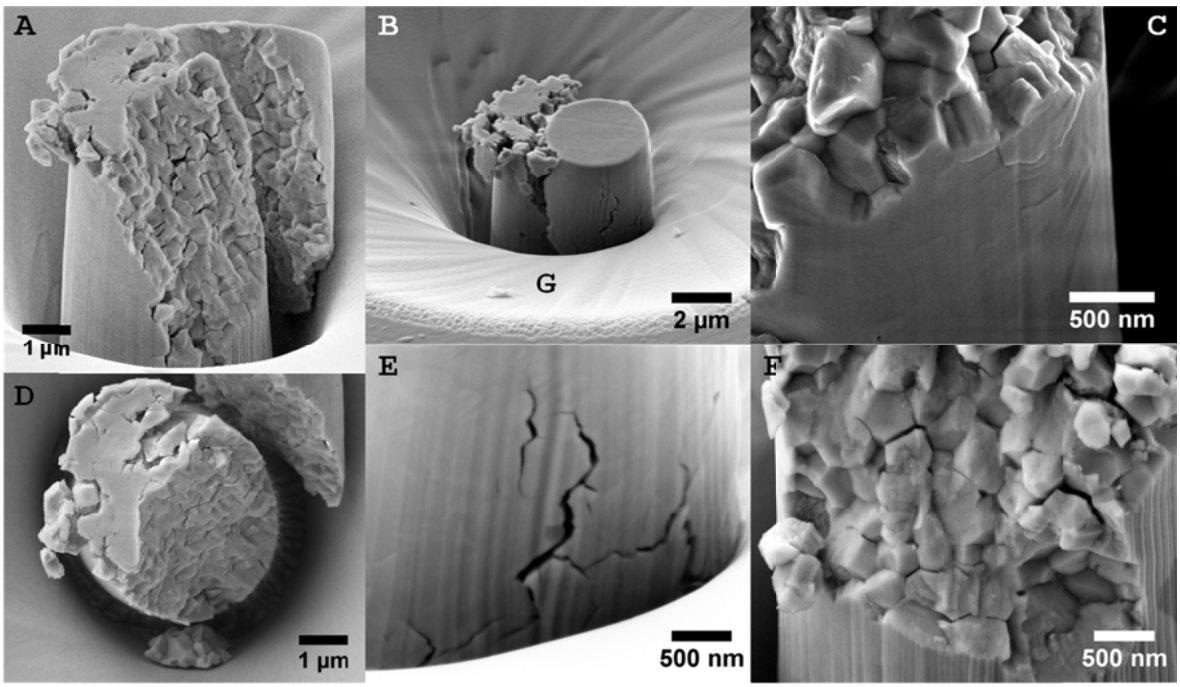

Fig. 6. Appearance of four 3.3 µm diameter pillars after failure. A and D: fracture surface with mixed intergranular-transgranular aspect plus the presence of growing intergranular microcracks. B and E: external surface of a second pillar, with evidence of crack merging and wing crack formation. C and F: details of the fracture surface from other two pillars, where the saw-toothed contour induced by transformation bands is observed in some areas.

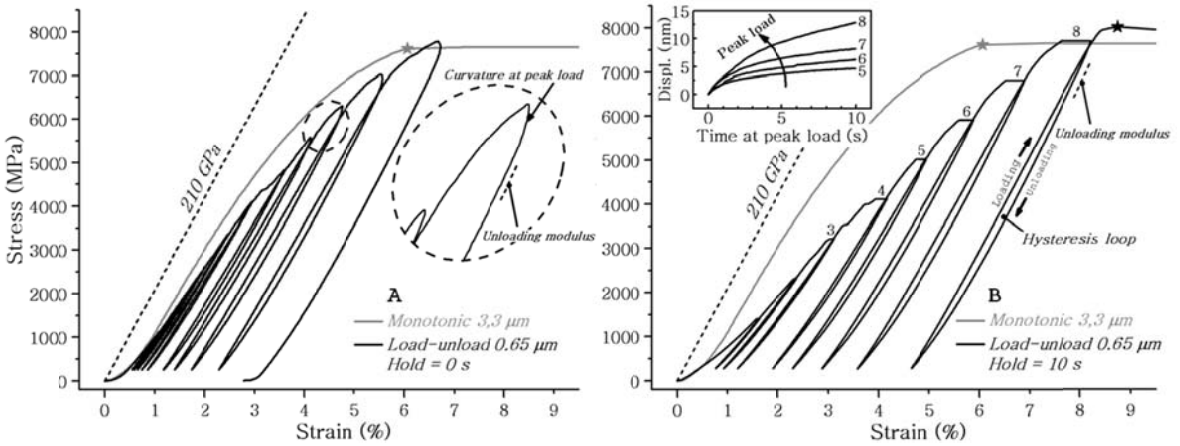

Fig. 7. A: progressive loading of a 0.65 µm diameter sample until 7.6 GPa, no hold. The detail shows the presence of a curvature in the upper part of the unloading curve. B: Progressive loading until rupture, 10 s hold segment at maximum load. The hysteresis loop in the unloading-reloading cycle is indicated. The insert shows the displacement at constant peak load.

The response of 0.65 µm micropillars to two cyclic loading-unloading tests at constant load amplitude is reported in Figure 7. The pillar was first cyclically loaded between 7.05 GPa and 0.3 GPa for 40 cycles and then the test was repeated by increasing the maximum stress to

8.40 GPa until failure. At the lower stress amplitude, most of the plastic strain occurs in the first cycles, with little additional plastic strain in the subsequent cycles (see the insert of Figure 8). The unloading curvature at peak load is observed only during the first cycle. When the peak stress is increased to 8.4 GPa, the deformation behavior during the first two cycles evolves similarly as for the previous amplitude, but in the 3rd cycle the loading-unloading loop starts to become wider, i.e. the cyclic plastic strain increases during the next cycles until failure sets in the 6th cycle.

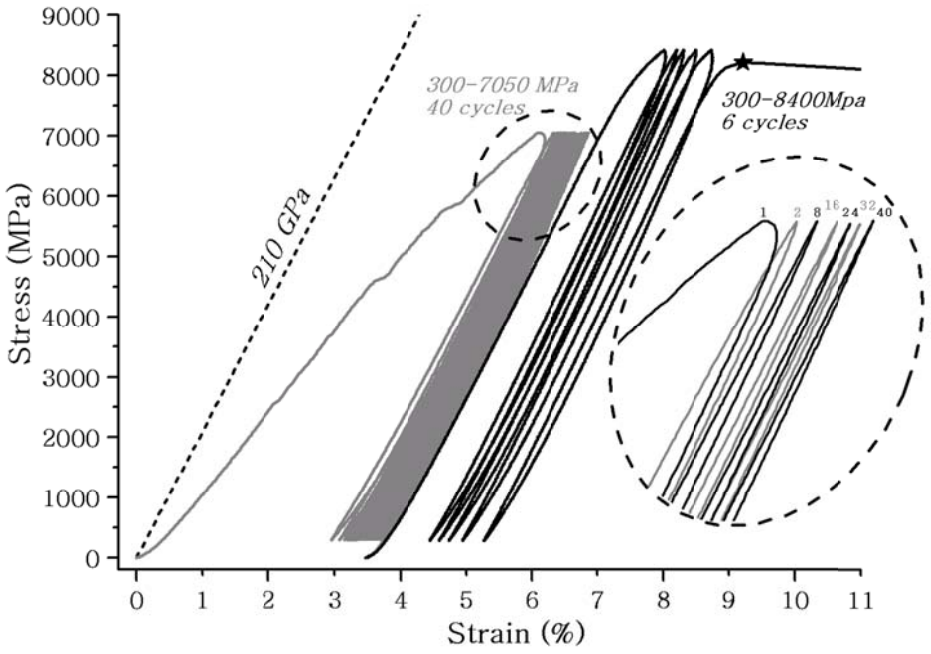

Fig. 8. Cyclic loading tests of a 0.65 μm diameter pillar. First test: 40 cycles, max load 7050 MPa. Second test: max load 8400 MPa, failure of the pillar at the 6th cycle.

4. Discussion

The micropillars tested in this work range from pure polycrystalline condition for 3.3 μm pillars, where there are approximately 10 grains along the diameter, to the bamboo-like grains arrangement in the ~0.3 μm pillars, where there are only 0 to 2 grain boundaries along the diameter (oligo-crystalline pillars).

In the previous section, it has been shown that the compressive strength increases considerably for the micropillars (6.5-9.3 GPa) with respect to the macroscopic tests (3.5-4.3 GPa). This result can be partly related to the different nature of defects in macro- and micro-samples. Processing defects of a few tens of micrometers in size are present inside the macro-samples, as it can be calculated for the critical crack size from the strength of macroscopic flexure tests, which is typically of ~1200 MPa. In fact, considering the value of 4.1 MPa√m as

KIC [35] and a semicircular defect with an appropriate geometric factor [36], the calculated radius is of ~8 μm. On the other hand, small-scale samples are milled from hypothetically defect-free regions, and indeed no defect was observed by SEM on the surface and FIB cross-sections prior to testing, with the exception of nanopores (20-50 nm). The absence of preexisting flaws was also demonstrated for zirconia micro-beams tested in bending in Ref. [37].

Another important difference is suggested by the shape of stress-strain curves. Nearly linear elastic behavior until failure was observed in tests of macroscopic specimens, while significant deviation from the linear elastic regime was recorded for the micropillars starting from 3-4 GPa (for 3.3 μm diameter micropillars), meaning that there is a transition from the brittle to quasi-plastic behavior between these length scales.

4.1. Failure modes

The generally accepted micromechanical model describing brittle failure in compression in absence of confinement is based on the existence of initial flaws or discontinuities. Under increasing stresses, suitably orientated flaws with respect to the compression axis nucleate tension cracks (wing cracks), which grow and curve toward the compression direction until failure by axial splitting [38]. The failure mode tends to shift to faulting, or macroscopic shear failure, when lateral confinement is applied to the body in compression [39].

In our case, failure occurred along inclined planes, resembling the shear faulting mode. The fact that only few microcracks were detected on the surface, cross-sections or lamellas of retrieved micropillars after stressing up to 90 % of the strength suggests that presumably most of the cracks are created at higher stresses close to the failure stress. In effect, a large number of microcracks were observed on the fracture and external surfaces of micropillars after failure (Fig. 6), showing evidence of interaction and merging of transformation-induced microcracks. The mixed fracture surface appearance is precisely the result of the combination of grain boundary crack formation (intergranular) and crack merging.

Nonetheless, transformation starts at much lower stresses without the simultaneous nucleation of a significant number of microcracks, as elucidated from both the microstructural observations and the deviation from linear behavior on the stress-strain curves. The hardening observed is likely to originate from the increasing stress necessary to induce transformation or

dislocation activity in residual tetragonal regions embedded in transformed monoclinic phase, in which the associated shape change may be hard to accommodate due to the constraints imposed by the surrounding transformed material and grain boundaries. While in monocrystals of tetragonal zirconia, like the ones tested by Lai and co-workers [30], martensitic transformation is simple, single variant and complete, in polycrystals the constraints associated with surrounding grains and triple points make it a more complex phenomenon. In this sense, Ueland et al. studied the cubic-monoclinic transformation of the shape-memory alloy Cu-Zn-Al by tensile testing of microwires with different grain size, reporting that regions of the parent phase were left untransformed near grain boundaries, while near triple points the transformation was partial and multivariant. Finite-elements simulations showed that the stresses associated with transformation relax very rapidly away from these singular regions, which also act as preferential sites for the nucleation of flaws and limit the amount of strain that can be sustained [40,41]. The t-m transformation of zirconia under tensile stress was also modeled using the phase-field method by Mamivand et al [42], confirming the localization of high stresses along triple points and grain boundaries. Here, we found the presence of multivariant transformation that was not complete close to grain boundaries, with the development of cracks at their intersection with monoclinic laths (see arrows in Fig. 5), suggesting a similar mechanism.

The presence of high concentration of transformation bands around alumina grains observed in the micropillar of Fig. C are likely to be the result of the stiffness mismatch between the two phases, which induces stresses at the interface during compression. In this case, the situation is similar but more severe than for grain boundaries and triple points, so the incompatible strain has to be accommodated by the formation of numerous multivariant martensitic laths, and flaws are likely to form at the interface by increasing the stress.

Following these concepts, it becomes clear that phase transformation occurs first in sites where the transformation strain is compatible with the microstructure constraints, while close to the failure stress it extends to regions where the incompatible strain and high local stresses associated to multivariant transformation are responsible for the simultaneous nucleation of many flaws that interact and merge leading to failure. The defect size created with this damage process is in principle independent from the sample size, and it can be estimated to be smaller than one grain facet. Failure can occur when the density of transformation-induced microcracks is enough for merging, which may occur through their interaction or by the nucleation of wing cracks. The stress necessary for wing crack formation

in brittle materials with the presence of small defects under compression could be calculated according to the model presented in Refs. [38,43]. However, since intergranular microcracks may have dimensions comparable to the diameter in sub-micrometric micropillars and plastic deformation takes place, the basic assumptions of elastic fracture mechanics are not fulfilled so the model cannot be applied.

4.2. Transformation-induced plasticity

The reduction of sample size and the absence of preexisting defects imply the transition to a quasi-plastic behavior in polycrystalline zirconia, showing strain hardening effects and irreversible deformation. The micropillars failure strains of 5.4% to 8.6% are considerably higher than for macroscopic samples, in which fracture occurs practically in the elastic regime at strains of ~2%.

In nanometric micropillars, the bamboo-like structure allows transformation to begin earlier than in micrometric ones, since grains are less constrained by the presence of none or few grain boundaries and the shape change can be better accommodated by the free surfaces. Strain bursts are in fact detected at stresses as low as, e.g. ~1700 MPa in these small micropillars (see Fig. 1-D). The slope between individual strain bursts is generally higher than for bigger micropillars after the onset of transformation-induced plasticity. While this is a continuous phenomenon in micrometric samples, it becomes a discrete phenomenon in sub-micrometric samples, where each event is more complete and produces a relatively higher contribution to the total strain. If we consider the transformation stress as the “yield stress” of zirconia micropillars, the rule “smaller being weaker” seems to apply here, meaning that the yield stress is smaller for smaller sizes. However, the important parameter that determines the plastic behavior is the nearly single crystal nature of the specimens with small diameter and not the diameter itself. Due to the scatter of the yield stress in 0.3 μm pillars, which must be orientation-related, a relation between yield stress and size cannot be established.

4.3. Loading-unloading tests at increasing peak load

Loading-unloading tests at increasing peak load show that the plastic component of the strain is higher for higher peak loads, indicating that a higher fraction of grains transforms as the load is increased and that the transformation under compression at these scales requires mechanical work to proceed.

The slight increase of the unloading modulus with the peak load could be related to the difference in the elastic modulus, which is moderately higher for monoclinic than for tetragonal zirconia [44,45]. Another explanation could be related to the change in the diameter due to the plasticity resulting from phase transformation and other possible inelastic phenomena, plus the volume increase associated to the transformation, which has to be accommodated in the radial direction. This effect is emphasized by the taper angle, as calculated by Zhang et al. [15]. On the other hand, the cracks that develop during loading do not reduce the stiffness of the pillars. Similar results were found in Ref. [46] during high strain rate loading of Y-TZP, where the amount of micro-cracking observed after complete transformation was not altering the stiffness of zirconia. In a parallel work, they excluded ferroelastic domain switching as a possible source of inelastic strain [47]. This behavior differs completely from micropillars extracted from the monoclinic surface layer that forms on 3Y-TZP after hydrothermal degradation, which present extensive microcracking [48]. The slope of the linear part of loading curves in monoclinic degraded micropillars is less than half the one of non-cracked tetragonal micropillars, due to the large population of microcracks at the grain boundaries. Even though the unloading slope at the peak load in loading-unloading tests also increases slightly with the peak load for degraded pillars, in this case the slope change is presumably the result of the closure of increasing fractions of cracks under the applied stress [48].

The unloading curvature at the peak load, as well the time-dependent deformation during the hold segment at the peak load, represent anelastic effects that were not expected if phase transformation would be the sole plastic deformation mechanism. In fact, since the t-m transformation does not need diffusion, it is essentially instantaneous. The total amount of strain at constant load increases with the value of the peak load, while the strain rate decreases with time. It may therefore be possible that dislocation movement is also activated at high stress, producing the observed time-dependent strains. In this case, dislocation glide may be the operating mechanism, since it generally occurs when $\sigma/G > 10\text{-}2$ and does not need diffusion. Although in nanoindentation experiments the presence of thermal drift may give a spurious strain contribution at constant load if not properly corrected, this possibility was carefully analyzed and discarded since in our case the time-dependent strains do not occur at loads below ~0.5 σ^* independently on pillar size. Moreover, this phenomenon was similar when testing on different nanoindenters and takes place mostly during the first seconds after the stress is kept constant.

The activation of dislocation movement at room temperature does not normally occur in bulk ceramic specimens without confinement. This is no longer valid at the small scale, where, for example, monocrystals of alumina, chromia, SiC and silicon nitride [27–29,49] have been deformed plastically under compression by slip. The participation of dislocation glide is likely to happen here since the stress level reached without fracture is comparable to confined deformation by indentation or grinding [33,50]. If we assume that in hardness testing the confinement allows plastic deformation to occur with a yield stress of about 1/3 of the macroscopic hardness value [51], it means that the threshold for plastic deformation in the present micropillars would be ~4.2 GPa, value which is well below the observed compressive strength. Even though the 1/3 ratio may be slightly higher for hard materials [52,53], we can imagine that numerous dislocations are formed giving a contribution to the total strain during loading. The sudden change to zero stress rate after reaching the peak stress may translate into the plastic deformation provided by transient dislocation movement during the hold segment.

The local shape change of the top region of some pillar (see Fig. 2-F) evidences the necessary existence of a plastic mechanism other than phase transformation, which could not produce such localized strain. In TEM images, both the presence of heavily distorted Moiré patterns and the blurred contrast exhibited by some distorted regions could indicate the dislocation-rich areas, while individual dislocations are not resolved. These regions coincide mostly with the grains –or grain fractions– that did not undergo phase transformation and could not sustain the deformation by means of transformation-induced plasticity, although the presence of bended martensitic plates indicates that also the transformed regions have been successively plastically deformed, similarly to what happens under a Vickers indentation [50]. High resolution TEM studies are needed to clarify the presence and role of dislocations, which will be the subject of future studies.

The thin hysteresis cycles observed between one unloading and the next reloading segments represents a pseudoelastic behavior, capable for dissipating mechanical work, which could be potentially associated to several factors. First, to the occurrence of a small fraction of reversible m-t transformation during unloading, which has been observed in both polycrystalline and monocrystalline zirconia, but always at temperatures above the final reversion temperature Ab (~1000 ºC for our composition) [30,54]. Second, the reorientation of ferroelastic domains inside t’ grains could take place, as observed first in Ce-TZP [55] and then in Y-TZP [56]. Two transitions stresses were observed at 400 ± 50 MPa and 1.6 ± 0.2 GPa for Y-TZP, contrarily to our observations that indicate a rather progressive phenomenon.

Third, the possible formation and annihilation of dislocations during loading/unloading could also be an explanation. Further research is required to clarify this point.

4.4. Cyclic loading-unloading tests at constant stress amplitude

During cyclic loading at constant stress amplitude with ~7 GPa peak stress there is no significant slope change with the number of cycles, meanwhile loading-unloading loops become thinner (cyclic hardening) and reach a saturation stage. The latter aspect may be related to either the saturation of the reversible phase transformation as observed in pseudoelastic zirconia [30] or/and dislocation glide. A minor fraction of inelastic strain seems to occur in each loading–unloading cycle, inducing a cumulative net strain after many cycles. By increasing the peak stress to 8.4 GPa on the same pillar, cyclic hardening is observed during the first two cycles, while the subsequent gradual widening of the loop can be the result of microcrack nucleation/growth right before fracture. Therefore, there seems to be a threshold stress below which damage is not increased by cyclic loading, which lies between 7 GPa and 8.4 GPa in this case. This stress level should correspond to the necessary stress for extensive flaw formation and fracture.

4.5. Possible sources of artifacts

4.5.1. Effect of fib ion implantation

The mechanical properties could be affected by Ga bombardment during pillar milling, as shown by Kiener et al. [57]. Several defects may appear, like point defects, dislocations and precipitates. The presence of these defects and the thickness of the affected layer depend on the energy of the ions and the impact angle. An amorphous layer forms at the surface, which may range from few nm in thickness to ~50 nm. The currents employed in our study suggest that our amorphous layer might be of not more than 10-20 nm thick, which was confirmed by TEM observations. The influence of this layer on dislocation movement in monocrystals might be important through the formation of dislocation pile-ups and the action of a back stress. In our case, where dislocation movement is not the main deformation mechanism, the amorphous layer is considered of minor importance. The nucleation of transformation occurs from internal stresses close to grain boundaries and triple points, so the surface modification induced by FIB may not alter this process.

4.5.2. Taper effect and correction for surface deflection

1º to 3.5º of taper angle were measured on the micropillars of this study. The impossibility of reproducing exactly the same taper angle and aspect ratio for all the samples is a further explanation for the slight differences in the observed elastic modulus, failure stress and strain. The asymmetry in loading induced by taper angle introduces an additional driving force for axial crack propagation, as outlined in Ref. [58,59], which was estimated to be in the range 6-22 % for similar angles in Si micropillars. Since failure occurred by shear faulting rather than pure axial splitting, this contribution is considered of secondary importance. The elastic modulus measured from the stress-strain curves is affected by three main sources of error. First, since the pillar top was chosen for calculation, this leads to an overestimation of the elastic modulus. Other authors have chosen to use mean or equivalent diameters, which makes sense when energetic analysis are of interest but not in our case, where the failure stress is of more importance [30]. Second, the deflection of the surface at the base of the pillar has not been taken into account. This spurious strain component can be corrected according to the Sneddon model [60], as it was done in the work of Frick et al. [61]. For the maximum loads employed at the small scale in this study, the calculated correction is less than 10%. Due to the limited effect of this correction and the presence of other sources of error, data are presented without it. Third, the occurrence of buckling would result in lower elastic modulus and failure stresses. In the few cases where bucking was suspected, like in the pillar of Fig. 2-F, results were not included.

Another point worthwhile mentioning is that the degree of phase transformation in the pillars is not homogeneous since the upper part in contact with the flat nanoindenter is more transformed than the bottom close to the base. This may be attributed to the smaller cross-section of the upper part as well as to the effect of non-uniform stresses near the contact and the presence of confinement in the lower part, which is likely to hinder the transformation.

Conclusions

- In polycrystalline zirconia micropillars the absence of natural defects, typical of macroscopic specimens, increases considerably the strength, allowing the activation of plastic deformation mechanisms and their study. Micropillars may reach strengths and failure strains which are roughly twice and four times larger than in macroscopic tests, respectively, showing evident shape change. The small-scale brittle-to-ductile transition is therefore not limited to ceramic monocrystals only.

- Transformation-induced plasticity is the main observed mechanism of plastic deformation, which occurs without significant damage up to stresses of about 90% of the strength. The threshold stress for its activation is smaller (down to ~1.7 GPa) for micropillars with diameter similar to the grain size.

- If a sufficiently high stress is held constant in the course of a monotonic test, an additional strain sets in during the first hold seconds, indicating a strain relaxation effect that may be associated to dislocation glide. The latter is assumed to play a role in the plastic deformation of micropillars, opening the path to further research.

- Cyclic loading-unloading tests show the existence of cyclic hardening during the first cycles and softening close to fracture, depending on the applied stress level.

Acknowledgements

The authors would like to acknowledge Prof. K. Leifer for the interesting discussions about electron microscopy images and for his support during the stay at Uppsala University. Prof. U. Wiklund and Dr. J. Heinrichs are kindly acknowledged for their assistance with the nanoindenter set-up, while O. Torrents is acknowledge for the in-situ testing. This work was supported by Ministry of Economy and Competitiveness (MINECO) under the project ref. MAT2011-23913 and by Government of Catalonia under the project ref. 2014SGR0137. Erik Camposilvan acknowledges Universitat Politècnica de Catalunya for the grant FPU-UPC.

References

[1] W.D. Nix, H. Gao, Indentation size effects in crystalline materials: A law for strain gradient plasticity, J. Mech. Phys. Solids. 46 (1998) 411–425.

[2] W.D. Nix, J.R. Greer, G. Feng, E.T. Lilleodden, Deformation at the nanometer and micrometer length scales: Effects of strain gradients and dislocation starvation, Thin Solid Films. 515 (2007) 3152–3157.

[3] N.A. Fleck, G.M. Muller, M.F. Ashby, J.W. Hutchinson, Strain gradient plasticity: theory and experiment, Acta Metall. Mater. 42 (1994) 475–487.

[4] T. Namazu, Y. Isono, T. Tanaka, Evaluation of size effect on mechanical properties of single crystal silicon by nanoscale bending test using AFM, J. Microelectromechanical Syst. 9 (2000) 450–459.

[5] C. Motz, T. Schöberl, R. Pippan, Mechanical properties of micro-sized copper bending beams machined by the focused ion beam technique, Acta Mater. 53 (2005) 4269–4279.

[6] D. Kiener, W. Grosinger, G. Dehm, R. Pippan, A further step towards an understanding of size-dependent crystal plasticity: In situ tension experiments of miniaturized single-crystal copper samples, Acta Mater. 56 (2008) 580–592.

[7] M.D. Uchic, D.M. Dimiduk, J.N. Florando, W.D. Nix, Exploring specimen size effects in plastic deformation of Ni3(Al, Ta), MRS Proc. 753 (2002) BB1.4.

[8] J.R. Greer, W.C. Oliver, W.D. Nix, Size dependence of mechanical properties of gold at the micron scale in the absence of strain gradients, Acta Mater. 53 (2005) 1821–1830.

[9] M. Legros, D.S. Gianola, C. Motz, Quantitative In Situ Mechanical Testing in Electron Microscopes, Mater. Res. Soc. Bull. 35 (2010) 354–360.

[10] a. B. Mann, D. van Heerden, J.B. Pethica, T.P. Weihs, Size-dependent Phase Transformations During Point Loading of Silicon, J. Mater. Res. 15 (2000) 1754–1758.

[11] K. Wasmer, T. Wermelinger, a. Bidiville, R. Spolenak, J. Michler, In situ compression tests on micron-sized silicon pillars by Raman microscopy—Stress measurements and deformation analysis, J. Mater. Res. 23 (2008) 3040–3047.

[12] H. Van Swygenhoven, S. Van Petegem, The use of Laue microdiffraction to study small-scale plasticity, Jom J. Miner. Met. Mater. Soc. 62 (2010) 36–43.

[13] D. Kiener, C. Motz, G. Dehm, Micro-compression testing: A critical discussion of experimental constraints, Mater. Sci. Eng. A. 505 (2009) 79–87.

[14] M.D. Uchic, P. a. Shade, D.M. Dimiduk, Plasticity of Micrometer-Scale Single Crystals in Compression, Annu. Rev. Mater. Res. 39 (2009) 361–386.

[15] H. Zhang, B.E. Schuster, Q. Wei, K.T. Ramesh, The design of accurate micro-compression experiments, Scr. Mater. 54 (2006) 181–186.

[16] W.C. Oliver, G.M. Pharr, An improved technique for determining hardness and elastic modulus using load and displacement sensing indentation experiments, J. Mater. Res. 7 (1992) 1564–1583.

[17] R. Dou, B. Derby, A universal scaling law for the strength of metal micropillars and nanowires, Scr. Mater. 61 (2009) 524–527.

[18] S. Korte, W.J. Clegg, Discussion of the dependence of the effect of size on the yield stress in hard materials studied by microcompression of MgO, Philos. Mag. 91 (2011) 1150–1162.

[19] M.G.D. Geers, W. a. M. Brekelmans, P.J.M. Janssen, Size effects in miniaturized polycrystalline FCC samples: Strengthening versus weakening, Int. J. Solids Struct. 43 (2006) 7304–7321.

[20] J.R. Greer, J.T.M. De Hosson, Plasticity in small-sized metallic systems: Intrinsic versus extrinsic size effect, Prog. Mater. Sci. 56 (2011) 654–724.

[21] P.S.S. Leung, a. H.W. Ngan, Size effect on the strength of micron-sized polycrystals – A dislocation dynamics simulation study, Scr. Mater. 69 (2013) 235–238.

[22] P.J.M. Janssen, T.H. de Keijser, M.G.D. Geers, An experimental assessment of grain size effects in the uniaxial straining of thin Al sheet with a few grains across the thickness, Mater. Sci. Eng. A. 419 (2006) 238–248.

[23] K. Kendall, The impossibility of comminuting small particles by compression, Nature. 272 (1978) 710–711.

[24] B.L. Karihaloo, The impossibility of comminuting small particles by compression, Nature. 279 (1979) 169–170.

[25] F. Östlund, P.R. Howie, R. Ghisleni, K. Leifer, W.J. Clegg, J. Michler, Ductile – brittle transition in micropillar compression of GaAs at room temperature, Philos. Mag. 91 (2011) 1190–1199.

[26] B. Moser, K. Wasmer, L. Barbieri, J. Michler, Strength and fracture of Si micropillars: A new scanning electron microscopy-based micro-compression test, (2007) 1–8.

[27] A. Montagne, S. Pathak, X. Maeder, J. Michler, Plasticity and fracture of sapphire at room temperature: Load-controlled microcompression of four different orientations, Ceram. Int. 40 (2014) 2083–2090.

[28] S. Kiani, K.W.K. Leung, V. Radmilovic, a. M. Minor, J.-M. Yang, D.H. Warner, et al., Dislocation glide-controlled room-temperature plasticity in 6H-SiC single crystals, Acta Mater. 80 (2014) 400–406.

[29] T. Csanádi, N.Q. Chinh, P. Szommer, J. Dusza, Z. Lenčés, P. Šajgalík, Deformation and Fracture of β-Silicon Nitride Micropillars, J. Am. Ceram. Soc. Rapid Comm (2014) 1–4.

[30] A. Lai, Z. Du, C.L. Gan, C. a. Schuh, Shape memory and superelastic ceramics at small scales., Science. 341 (2013) 1505–8.

[31] R.C. Garvie, R.H.J. Hannink, R.T. Pascoe, Ceramic steel?, Nature. 258 (1975) 703–704.

[32] K. Kobayashi, H. Kuwajima, T. Masaki, Phase change and mechanical properties of ZrO2-Y2O3 solid electrolyte after ageing, Solid State Ionics. 3-4 (1981) 489 – 493.

[33] J.A. Muñoz Tabares, E. Jiménez-Piqué, J. Reyes-Gasga, M. Anglada, Microstructural changes in 3Y-TZP induced by scratching and indentation, J. Eur. Ceram. Soc. 32 (2012) 3919–3927.

[34] R.H.J. Hannink, P.M. Kelly, B.C. Muddle, Transformation Toughening in ZrO2-Containing Ceramics, J. Am. Ceram. Soc. 83 (2000) 461–487.

[35] M. Turon-Vinas, M. Anglada, Fracture toughness of zirconia from a shallow notch produced by ultra-short pulsed laser ablation, J. Eur. Ceram. Soc. 34 (2014) 3865–3870.

[36] S. Strobl, P. Supancic, T. Lube, R. Danzer, Surface crack in tension or in bending – A reassessment of the Newman and Raju formula in respect to fracture toughness measurements in brittle materials, J. Eur. Ceram. Soc. 32 (2012) 1491–1501.

[37] E. Camposilvan, O. Torrents, M. Anglada, Small-scale mechanical behavior of zirconia, Acta Mater. 80 (2014) 239–249.

[38] S. Nemat-Nasser, H. Horii, Compression-induced nonplanar crack extension with application to splitting, exfoliation, and rockburst, J. Geophys. Res. 87 (1982) 6805.

[39] H. Horii, S. Nemat-Nasser, Brittle failure in compression: splitting, faulting and brittle-ductile transition, Philos. Trans. R. Soc. …. 319 (1986) 337–374.

[40] S.M. Ueland, Y. Chen, C. a. Schuh, Oligocrystalline Shape Memory Alloys, Adv. Funct. Mater. 22 (2012) 2094–2099.

[41] S.M. Ueland, C. a. Schuh, Grain boundary and triple junction constraints during martensitic transformation in shape memory alloys, J. Appl. Phys. 114 (2013) 053503.

[42] M. Mamivand, M. Asle Zaeem, H. El Kadiri, M.A. Zaeem, H. El Kadiri, Shape Memory Effect and Pseudoelasticity Behavior in Tetragonal Zirconia Polycrystals: A Phase Field Study, Int. J. Plast. 60 (2014) 71–86.

[43] M.F. Ashby, S.D. Hallam, The failure of brittle solids containing small cracks under compressive stress states, Acta Metall. 34 (1986) 497–510.

[44] E.Y. Fogaing, Y. Lorgouilloux, M. Huger, C.P. Gault, Young's modulus of zirconia at high temperature, J. Mater. Sci. 41 (2006) 7663–7666.

[45] X.S. Zhao, S.L. Shang, Z.K. Liu, J.Y. Shen, Elastic properties of cubic, tetragonal and monoclinic ZrO2 from first-principles calculations, J. Nucl. Mater. 415 (2011) 13–17.

[46] G. Subhash, S. Nemat-Nasser, Uniaxial stress behaviour of Y-TZP, J. Mater. Sci. 28 (1993) 5949–5952.

[47] G. Subhash, S. Nemat-Nasser, Dynamic Stress-Induced Transformation and Texture Formation in Uniaxial Compression of Zirconia Ceramics, J. Am. Ceram. Soc. 76 (1993) 153–165.

[48] E. Camposilvan, M. Anglada, Micropillar compression inside zirconia degraded layer, J. Eur. Ceram. Soc. (2015).

[49] D.D. Stauffer, Deformation Mechanisms in Nanoscale Brittle Materials, Univerity of Minnesota, 2011.

[50] A. Pajares, F. Guiberteau, K.H. Westmacott, A. Dominguez-Rodriguez, TEM characterization of indented polycrystalline Y-PSZ, J. Mater. Sci. 28 (1993) 6709–6714.

[51] D. Tabor, The hardness of metals, Clarendon Press, Oxford, UK, 1951.

[52] J.J. Gilman, Relationship Between Impact Yield Stress and Indentation Hardness., J. Appl. Phys. 46 (1975) 1435–1436.

[53] L.J. Vandeperre, W.J. Clegg, The correlation between hardness and yield strength of hard materials, in: Mater. Sci. Forum Vols. 492-493, Trans Tech Publ, 2005: pp. 555–560.

[54] P.E. Reyes-Morel, Transformation Plasticity of Ce02-Stabilized Tetragonal Zirconia Polycrystals: II, Pseudoelasticity and Shape Memory Effect, J. Am. Ceram. Soc. 71 (1988) 648–657.

[55] A. V. Virkar, R.L.K. Matsumoto, Ferroelastic Domain Switching as a Toughening Mechanism in Tetragonal Zirconia, J. Am. Ceram. Soc. 69 (1986) C–224 – C–226.

[56] M.G. Cain, M.H. Lewis, Evidence of Ferroelasticity in Y-Tetragonal Zirconia Polycrystals, Mater. Lett. 9 (1990) 309–312.

[57] D. Kiener, C. Motz, M. Rester, M. Jenko, G. Dehm, FIB damage of Cu and possible consequences for miniaturized mechanical tests, Mater. Sci. Eng. A. 459 (2007) 262–272.

[58] P.R. Howie, S. Korte, W.J. Clegg, Fracture modes in micropillar compression of brittle crystals, J. Mater. Res. 27 (2011) 141–151.

[59] K. Kendall, Complexities of Compression Failure, Proc. R. Soc. A Math. Phys. Eng. Sci. 361 (1978) 245–263.

[60] I.N. Sneddon, The relation between load and penetration in the axisimmetric boussinesq problem for a punch of arbitrary profile, Int. J. Eng. Sci. 3 (1965) 47–57.

[61] C.P. Frick, B.G. Clark, S. Orso, a. S. Schneider, E. Arzt, Size effect on strength and strain hardening of small-scale [1 1 1] nickel compression pillars, Mater. Sci. Eng. A. 489 (2008) 319–329.

Annex B

Article VII: Development of a novel zirconia dental post resistant to hydrothermal degradation

The article is available for download at the following web address:

http://dx.doi.org/10.1088/1757-899X/31/1/012016

Annex C

Other Contributions

Conference Proceedings

• **Camposilvan, E**; Anglada, M, *"Micro-compression of zirconia degraded layer"*, Proceedings of the 14th European Inter-Regional Conference on Ceramics, pp. 24-30. 2014. ISBN 978-3-8440-2975-8.

• **Camposilvan, E**; Jimenez-Pique, E; Anglada, M, *"Micro-mechanical testing of advanced ceramics: tools, procedures and first results"*, Anales de mecánica de la fractura. 2, pp. 451-456. 2013. ISSN 0213-3725.

• Marro FG, **Camposilvan E**, Mestra A, Anglada M, *"Decoration of indentation cracks in 3Y-TZP by hydrothermal ageing"*, Anales de mecánica de la fractura. 29 - 1, pp. 83-88. 2012. ISSN 0213-3725

• **Camposilvan E**, Marro FG, Maspero F, Cuspidi G, Anglada M, *"Mechanical properties of alumina infil-trated zirconia nanocomposites"*. In: Actas del XIII Congreso Nacional de Propiedades Mecánicas de Sólidos (XIII PMS), pp. 203-208. 0027. ISBN 978-84-8363-897-2.

• Marro F, **Camposilvan E**, Anglada M, *"Increasing low temperatura degradation resistance by a thin diffusion layer of cerium in 3Y-TZP"*, Proceedings of the 13th European Inter-Regional Conference on Ceramics, pp. 193-196. (2012). ISBN 978-84-615-9681-2.

• **Camposilvan E**, Marro FG, Mestra A, Anglada M, *"Aging resistance and fracture toughness of ceria–infiltrated zirconia"*. In: XII Congreso nacional de materiales, Universidad de Alicante, pp. 1-4. ISBN 978-84-695-3316-1.

Patents

Patent name: Procedimiento para el aumento de la durabilidad de la Circona en aplicaciones dentales
Inventors: Fernando Garcia Marro; Alvaro Miguel Mestra Rodríguez; Erik Camposilvan; Marcos Juan Anglada Gomila
Patent holding body: Universitat Politècnica de Catalunya
Application number: P201131289 Date: 28/07/2011

Posters and oral presentations

• **Camposilvan E**, Flamant Q, Anglada M, *"Surface roughened zirconia: control of hydrothermal degradation"*. In: 13th International Conference of the European Ceramic Society, Toledo 21-25 June 2015. Oral presentation.

• **Camposilvan E** and Anglada M, *"Degradation of surface mechanical properties of 3Y-TZP in humid environments"*. In: LIV Congress of the Spanish Society of Glass and Ceramic (SECV), Badajoz 19-22 November 2014. Oral presentation.

• **Camposilvan E** and Anglada M, *"Micro-compression of zirconia degraded layer"*. In: CIEC14, European Inter-regional Conference on Ceramics, Stuttgart 8-10 September 2014. Oral presentation.

• Flamant Q, **Camposilvan E**, Anglada M, *"Assessment of the ageing sensitivity of surface modified acid-etched zirconia for increased osseointegration"*. In: E-MRS 2014 Fall Meeting, Warsaw University of Technology, Poland, 15-18 September 2014. Oral presentation.

• **Camposilvan E** and Anglada M, *"Micro-mechanical testing of Zirconia"*. In: 13th International Conference of the European Ceramic Society, Ester Technopole – Limoges, France, 23-27 June 2013. Oral presentation.

• **Camposilvan E**, Marro FG, Mestra A, Anglada M, *"ATZ via infiltration method: mechanical properties, aging resistance and wear behavior"*. In: 7th EEIGM International conference on advanced materials research, Luleå, March 2013. Oral presentation.

• **Camposilvan E**, Marro FG, Anglada M, *"In situ Study of sintering of alumina-zirconia nanocomposites obtained by the infiltration method"*. In: 7th EEIGM International conference on advanced materials research, Luleå, March 2013. Poster.

• **Camposilvan E**, Jiménez-Piqué E, Anglada M, *"Micro-Mechanical testing of advanced ceramics: tools, procedures and first results"*. In: XXX Encuentro Grupo Español de Fractura, Toledo, March 2013. Oral presentation.

• Muñoz-Tabares JA, **Camposilvan E**, Chintapalli R, Mestra A, Marro FG, Jiménez-Piqué E, Anglada M, *"Resistance to surface degradation of Yttria doped Zirconia"*. In: XXVIII Trobades Científiques de la Mediterrània a Maó (Menorca), 24-26 October 2012. Oral presentation.

• **Camposilvan E**, Marro FG, Maspero F, Cuspidi G, Anglada M, *"Mechanical properties of alumina infiltrated zirconia nanocomposites"*. In: Congreso Nacional de Propiedades Mecánicas de Sólidos (XIII PMS). Alcoy, 26-28 September 2012. Oral presentation.

• Marro FG, **Camposilvan E**, Jiménez-Piqué E, Mestra A, Anglada M, *"Increasing low temperature degradation resistance by a thin diffusion layer of Cerium in 3Y-TZP"*. In: CIEC13, European Inter-regional Conference on Ceramics, Barcelona, 12-14 September 2012. Poster.

• **Camposilvan E**, Marro FG, Mestra A, Anglada M, *"Aging resistance and fracture toughness of ceria–infiltrated zirconia"*. In: XII Congreso nacional de materiales, Universidad de Alicante, 30 y 31 of May and 1 June 2012. pp. 1-4. Oral presentation.

• Marro FG, **Camposilvan E**, Mestra A, Anglada M, *"Decoration of indentation cracks in 3Y-TZP by hydrothermal ageing"*. In: XXIX Encuentro Grupo Español de Fractura, Bilbao, 21-23 March 2012. Oral presentation.

• **Camposilvan E**, Marro FG, Mestra A, Anglada M, *"Development of a novel zirconia dental post resistant to hydrothermal degradation"*. In: 6th EEIGM International conference on advanced materials research, Nancy, France, 7-8 November 2011. Oral presentation.

Erratum

In Chapter 5. Article I, section 2: Materials and methods (p. 1542).

- Line 8: 1100 ºC instead of 1200 ºC
- Line 9: ~47% instead of ~35 %
- Line 11: 75% instead of 50%.
- Next column, line 4 from the top: ~9 wt% instead of 2.5% wt.
- Table 1 (p. 1543), “AS3 line”: grain size is 0.46 μm instead of 0.30 μm.